THE CMS FORWARD CALORIMETER PROTOTYPE DESIGN STUDIES AND Ω_C^0 SEARCH AT E781 EXPERIMENT AT FERMILAB

by

Ahmet Sedat Ayan

An Abstract

Of a thesis submitted in partial fulfillment of the
requirements for the Doctor of Philosophy
degree in Physics in the
Graduate College of The
University of Iowa

May 2004

Thesis Supervisor: Professor Yasar Onel

ABSTRACT

In the first part, the Compact Muon Solenoid (CMS) forward calorimeter design studies are presented. The forward calorimeter consists of quartz fibers embedded in a steel absorber. Radiation damage studies of the quartz fiber and the absorber as well as the results of the first pre-production prototype PPP-I are presented. In the second part, the Ω_c^0 search studies at the SELEX (E781) experiment at FermiLab are presented. 107 ± 22 Ω_c^0 events are observed in three decay modes. The relative branching ratio $(\Omega_c^0 \to \Omega^-\pi^-\pi^+\pi^+)/\mathcal{B}(\Omega_c^0 \to \Omega^-\pi^+)$ is measured as $2.00 \pm 0.45(stat) \pm 0.32(sys)$.

Abstract Approved: _____
Thesis Supervisor

_____
Title and Department

_____
Date

THE CMS FORWARD CALORIMETER PROTOTYPE DESIGN STUDIES AND Ω_C^0 SEARCH AT E781 EXPERIMENT AT FERMILAB

by

Ahmet Sedat Ayan

A thesis submitted in partial fulfillment of the
requirements for the Doctor of Philosophy
degree in Physics in the
Graduate College of The
University of Iowa

May 2004

Thesis Supervisor: Professor Yasar Onel

Graduate College
The University of Iowa
Iowa City, Iowa

CERTIFICATE OF APPROVAL

PH.D. THESIS

This is to certify that the Ph.D. thesis of

Ahmet Sedat Ayan

has been approved by the Examining Committee for the thesis requirement for the Doctor of Philosophy degree in Physics at the May 2004 graduation.

Thesis Committee: _____
Yasar Onel, Thesis Supervisor

_____
Edward R. McCliment

_____
Edwin Norbeck

_____
Mary Hall Reno

_____
Tuong Ton-That

ACKNOWLEDGMENTS

I wish to thank my supervisor Prof. Yasar Onel, first for giving me the opportunity to study at the University of Iowa and second, for supporting me in my research efforts. I would also like to thank Maurizio Iori at the University of Rome for his valuable contributions and suggestions. I am grateful to Peter Cooper of FermiLab for always making time to talk to me and answering my questions. Soon Yung Jun of FermiLab was especially helpful in making suggestions and answering my numerous questions in the early days of Ω_c^0 analysis. I am also indebted to Edward McCliment of the University of Iowa, Erhan Gulmez of Bogazici University , and Jim Russ of Carnegie Melon University.

I would not be here were it not for the love and support of my family. Their encouragement gives me confidence to work towards my goals.

I have met many wonderful colleagues and friends through this experience. I am especially grateful to Ugur Akgun, Ahmet Akyol, Bugrahan Oktay for their friendship.

Finally I wish to thank Laura McDonald for believing in me. Without her constant love and support I would not be able to complete this endeavor.

ABSTRACT

In the first part, the Compact Muon Solenoid (CMS) forward calorimeter design studies are presented. The forward calorimeter consists of quartz fibers embedded in a steel absorber. Radiation damage studies of the quartz fiber and the absorber as well as the results of the first pre-production prototype PPP-I are presented. In the second part, the Ω_c^0 search studies at the SELEX (E781) experiment at FermiLab are presented. 107 ± 22 Ω_c^0 events are observed in three decay modes. The relative branching ratio $(\Omega_c^0 \to \Omega^-\pi^-\pi^+\pi^+)/\mathcal{B}(\Omega_c^0 \to \Omega^-\pi^+)$ is measured as $2.00 \pm 0.45(stat) \pm 0.32(sys)$.

TABLE OF CONTENTS

LIST OF TABLES

Table

LIST OF FIGURES

Figure

CHAPTER 1
INTRODUCTION

This thesis consists of two independent studies. In the first part, Compact Muon Solenoid (CMS), Hadron Forward Calorimeter (HF) design and Pre-Production-Prototype test beam studies are discussed.

The CMS detector [1] has been designed to detect new physics at the Large Hadron Collider (LHC). This task will be accomplished by measuring energies of muons, electrons, photons and jets of charged and neutral particles. The name of the detector, Compact Muon Solenoid, is inherited from a 4 T Solenoidal Superconducting Magnet. In chapter 2, we will present a brief introduction of the CMS detector and the LHC project. The quartz fiber calorimeter technique of HF will also be introduced.

There has been a pressing need for radiation damage and activation analysis studies for the detectors planned at the Large Hadron Collider, particularly because some of them will experience several hundreds of MRads during their useful lifetime. The forward calorimeters especially will face unprecedented particle fluxes. In the Compact Muon Solenoid experiment, for example, at η[1] $= 5$ in $\sim$ 10 years of LHC operation, the forward calorimeters are expected to experience ~ 1 GRad of dose [1]. In chapter 3, the quartz fiber radiation damage studies done under neutron radiation will be discussed. In chapter 4, the radiation damage and the activation studies will be presented. And finally to end the first part of this thesis, first Pre-Production-Prototype (PPP-I) of the HF design and the test beam results are discussed in chapter 5.

In the second part, we present the results of our analysis on the Ω_c^0 search at the E781 experiment at FermiLab. The Ω_c^0 is a doubly-strange single-charmed baryon. Most singly charmed baryons have been well studied; Λ_c^+, Ξ_c^+, Ξ_c^0 for example. However Ω_c^0's experimental observation is relatively new and the statistics of the observed number of

[1] pseudo-rapidity η is defined as $\eta = -ln[tan(\theta/2)]$ where angle θ is with respect to the beam axis.

events are not very high. A summary of these observations will given in chapter 6. For the complete understanding of the properties of charmed baryons and their hadronic decay mechanisms it is crucial that Ω_c^0's mass, lifetime and relative decay fractions are understood well. After an introduction to charm physics in chapter 6, the E781 (SELEX) experiment are introduced in chapter 7. Finally in chapter 8, we present our measurements on the Ω_c^0 and the $\mathcal{B}(\Omega_c^0 \to \Omega^-\pi^-\pi^+\pi^+)/\mathcal{B}(\Omega_c^0 \to \Omega^-\pi^+)$ relative decay fraction.

CHAPTER 2
CMS FORWARD CALORIMETER PREPRODUCTION PROTOTYPE PPP I DESIGN-TEST STUDIES

2.1 Large Hadron Collider

The Large Hadron Collider (LHC) is a proton-proton collider being built in the LEP tunnel at CERN, Switzerland. Its center of mass energy will be 14 TeV. Heavy ion beams such as Pb will also be available instead of proton beams at energies reaching to 1250 TeV. For the proton beam operation mode, the LHC will reach a luminosity of $\mathcal{L}$=10^{34} cm^{-2}s^{-1} by filling each of the beams with 2835 bunches of 10^{11} protons resulting in a beam current of I_b=0.53 A. Two detectors, ATLAS and CMS, will record interactions created by the proton-proton collisions and heavy ions and will try to observe the Higgs and super-symmetric particles. There are two other detectors, ALICE and LHCb. ALICE is designed primarily for the heavy ion beam collisions. It will study the very hot soup of quarks and gluons created in the heavy ion collisions. LHCb is designed to look for B-mesons produced in proton collisions. A schematic of the LHC accelerator and the detectors mentioned above is shown in figure 2.1.

2.2 CMS Detector

The CMS detector is shown in Figure 2.2. It has a solenoidal 4 T superconducting 13.0 m long magnet with an inner diameter of 5.9 m. It is surrounded by 5 wheels (cylindrical objects) and 2 end-caps (disks) of muon absorber and muon tracking chambers. The total length of the detector is 21.6 m and the outer diameter is 14.6 m. Charged particle trackers and calorimeters (hadron and electromagnetic) are located inside the solenoid magnet. Two end-cap calorimeters and muon end-caps cover two ends of the detector. The CMS tracker is composed of a silicon pixel barrel and forward disks and

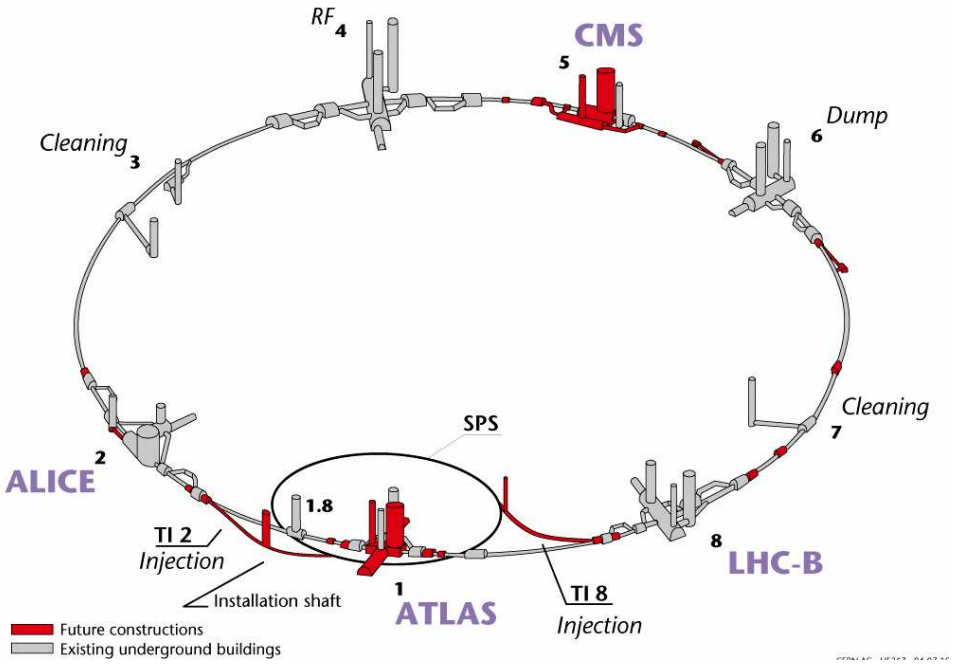

Figure 2.1: Schematic representation of LHC accelerator and the locations of ALICE, ATLAS, CMS, and LHCb detectors.

silicon micro-strip devices. The electromagnetic calorimeter is made up of $PbWO_4$ crystals, each 23 cm (25.8 X_o[1], 1.1 λ[2]) long and 2 cm x 2 cm in lateral dimensions. The response of the electromagnetic and hadronic calorimeters constitutes the data for the reconstruction of particle jets and the missing transverse energy.

2.3 The CMS Hadron Calorimeter

The hadronic calorimeter is a crucial part of the CMS detector. This calorimeter will help measure quark, gluon and neutrino directions and energies by measuring the energy and directions of particle jets and of missing transverse energy flow. It will also help with the identification of electrons, photons and muons together with the

[1]Radiation length X_o: Scaling variable for the probability of occurrence of bremsstrahlung pair production, and for the variance of the angle of multiple scattering

[2]Interaction length λ: The mean free path of a hadron before undergoing an interaction that is neither elastic nor quasi-elastic (diffractive), in a given medium

electromagnetic calorimeter and the muon system. The pseudo-rapidity range of ($\eta <$ 3.0) is covered by the Hadron Barrel (HB), and Hadron End-cap (HE), calorimeters. To extend the pseudo-rapidity region to $3.0 < \eta < 5.0$, a separate forward calorimeter, HF, is introduced. It is composed of quartz fibers embedded in an iron matrix. Its location, $3.0 < \eta < 5.0$, will be in a region where a very high radiation environment will be present.

2.4 The Physics Potentials

The Standard Model (SM), describes the electroweak interaction. Mathematically speaking, it is, in fact, the $SU(2)$ x $U(1)$ symmetry group which is broken spontaneously through the existence of the Higgs field with a non-zero vacuum expectation value. As a result, the massive $W^{\mp}$ and Z bosons and the massless photon emerge. However, the Higgs boson is yet to be observed.

The basic goal of the CMS detector is to explore the physics beyond the electroweak symmetry breaking scale. The discovery of Standard Model Higgs or super-symmetric Higgs bosons is one of the challenges that the CMS detector will face. This detector should also have the capability of detecting new unexpected physics. These goals set a high burden on the hadronic forward calorimeter since it is essential to measure the missing energy, E_T^{miss}, jets coming from Higgs.

2.4.1 The Role of Forward Calorimeter

The measurement of the E_T^{miss} is essential for the search for SM Higgs by $H \rightarrow WW \rightarrow l\nu jj$ channels. It is also crucial in SUSY Higgs searches for $H \rightarrow \tau\tau \rightarrow e\mu + E_T^{miss}$ and $H \rightarrow \tau\tau \rightarrow lh + E_T^{miss}$ channels to make H mass reconstruction possible.

For the $H \rightarrow WW \rightarrow l\nu jj$ and $H \rightarrow ZZ \rightarrow l\nu jj$ channels, two forward jet tagging is important. These jets are energetic, with a longitudinal momentum of $< p_L >= 1$ TeV and with a transverse momentum of the order of m_W and are produced in the

pseudo-rapidity region of $5.0 > \eta > 2.0$ which falls into the Forward Calorimetry region.

2.5 Quartz Fiber Calorimeter

The quartz fiber calorimeter is based on the detection of Čerenkov radiation [2] which is emitted by a charged particle traversing a quartz fiber with a velocity greater than speed of light in quartz. The opening angle of the Čerenkov radiation is a function of the velocity of the particle, $\beta = v/c$:

$$cos(\theta_c) = 1/n\beta \tag{2.1}$$

where n is the refractive index of quartz. The total light yield due to the Čerenkov effect is calculated as

$$\frac{d^2N}{dxd\lambda} = 2\pi\alpha z^2(sin^2\theta_c/\lambda^2) = 2\pi\alpha z^2/\lambda^2[1 - 1/\beta^2 n^2(\lambda)] \tag{2.2}$$

where is α the fine structure constant, θ_c is the Čerenkov angle, λ is the wavelength of the emitted light, x is the path of the particle in the medium and z is the charge of the incident particle. The quantity $\alpha = 1/137$ is the fine structure constant.

The particles which enter the absorber create particle showers, and those which are charged particles with a β greater than the threshold value emit Čerenkov radiation. The created showers are narrow. For electron showers, for example, the transverse size of the shower is smaller than the Moliere radius, $R_M = X_0E_s/E_c$, where X_0 is radiation length, E_s is 21 MeV and E_c is the critical energy. E_c is defined as the energy at which an electron's energy loss by bremsstrahlung and by ionization are equal and it is characterized approximately as $E_c = (800\text{ MeV})/(Z+1.2)$.

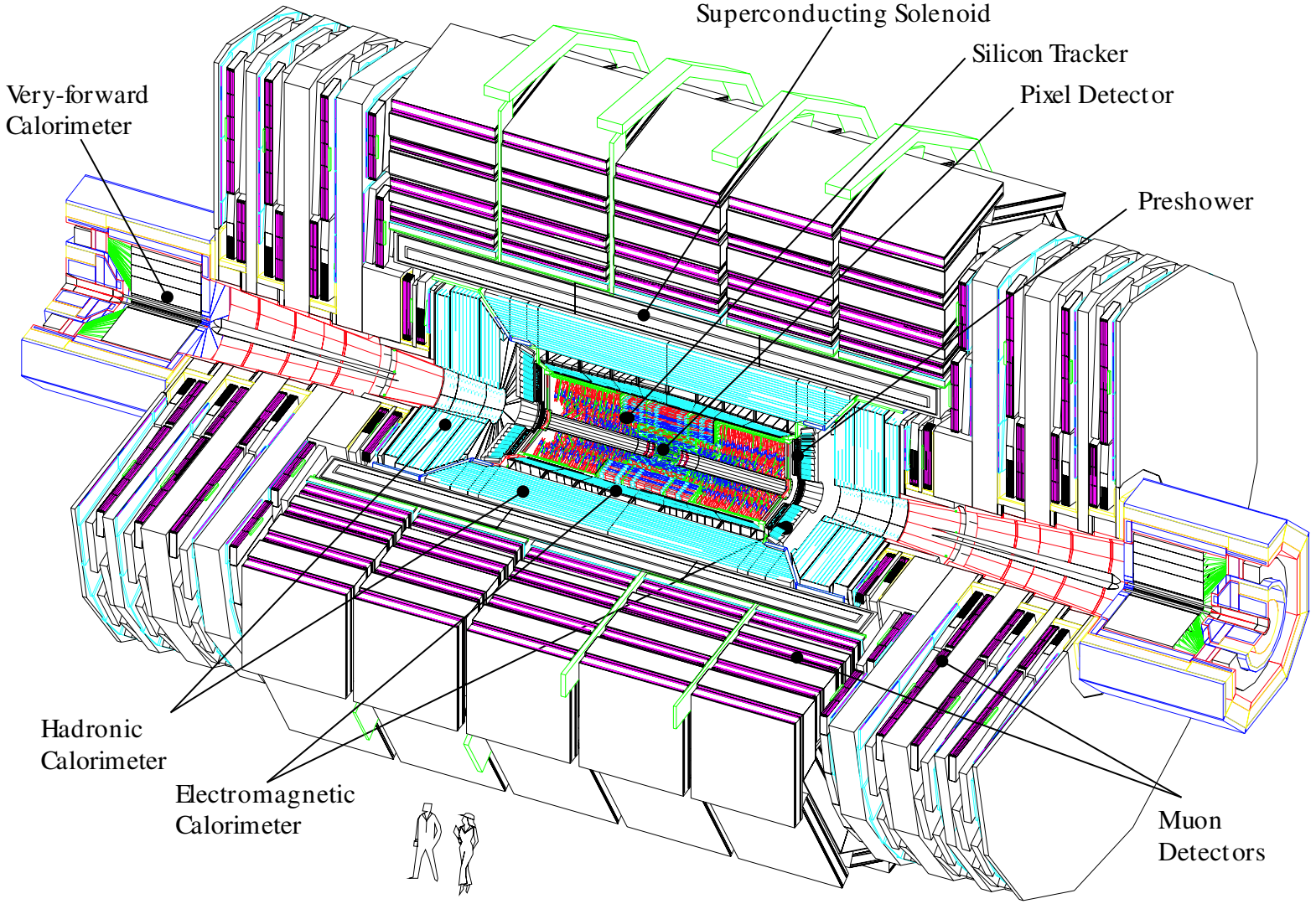

Figure 2.2: Compact Muon Solenoid (CMS) Detector

CHAPTER 3
RADIATION DAMAGE STUDIES OF QUARTZ FIBERS

The forward calorimeter (HF) in CMS will experience unprecedented particle fluxes. On average, 760 GeV per event is incident on the two forward calorimeters, compared to only 100 GeV for the rest of the main detector. Moreover, this energy is not uniformly distributed, but has a pronounced maximum at the highest rapidities. At $\eta = 5$ and integrated luminosity of 5×10^5 pb^{-1} ($\sim$ 10 year of LHC operation), the HF will experience $\sim$ 1 GRad [1]. The neutron rates ($E_n \leq 14$ MeV) at the front of the detector will be of order of 10^8 Hz/cm^2. The charged hadron rates will also be extremely high, especially at the shower maximum of the HF where the rate will reach 10^{13} to 10^{16} Hz/cm^2. This hostile environment presents a unique challenge in particle detection techniques.

Since their advent, optical fibers have found diverse applications and have experienced dramatic improvements. One such emerging application is the use of silica-core and Fluorine-doped silica-clad fibers as the active component in the HF. This choice was based predominantly on their exceptional radiation resistance. In such a calorimeter, the signal is detected when charged shower particles above the Čerenkov threshold ($E > 200$ keV) generate Čerenkov light, thereby rendering the calorimeter mostly sensitive to the electromagnetic component of showers. The performance characteristics of this detector are given in detail elsewhere [3].

Although scientific literature reports the optical characteristics of these types of fibers in detail, they generally refer to the infrared band [4]: mainly three discrete wavelengths, 820, 1300 and 1550 nm. In addition, most studies are conducted with γ or electron irradiation. We concentrated on the effects of neutrons on a shorter wavelength region, $325 \leq \lambda \leq 800$ nm, with special attention to the photo multiplier tube, (PMT),

sensitivity range, 400 to 500 nm.

3.1 Experimental Setup

We performed measurements at two differnet facilities; at a 10-kW experimental reactor, UTR-10, at Iowa State University (ISU) in Ames, Iowa and at the MGC-20E cyclotron at ATOMKI in Debrecen, Hungary. Special attention was paid to the fact that the apparatus and the methods used to analyze data were as identical as possible.

An Ocean Optics Model SD2000 spectrometer with a pulsed Xe lamp (10 Hz pulse rate) was used for all measurements. The spectral resolution was better than 1 nm and the data were collected within an integration time of 300 msec. A xenon lamp injects about 5–10 μwatts of power per pulse into fibers, (numerical aperture = $\sqrt{n_{core}^2 - n_{clad}^2}$ = 0.22).

The types of fibers used in these initial studies are listed in Table 3.1. Our objective at this time was to establish a coherent methodology for testing and specifying fibers for the forward calorimeter and not to perform an exhaustive test of all available fibers.

Table 3.1: Types of fibers used in this study are listed below. The FSHA- and FIA-type fibers are manufactured by Polymicro Inc. (USA) and IN-type is by INFOS (Russia).

ID	Core (μm)	Clad (μm)	Buffer(μm)	OH^- (ppm)
FSHA	Silica (300)	Polymer (320)	Acrylate (345)	$\sim$700
FIA	Silica (200)	F-Silica (240)	Acrylate (500)	$<$1
IN	Silica (300)	F-Silica (316)	Polyimide (345)	$\sim$1200

3.1.1 ISU UTR-10 Reactor

In the core of the reactor, the optical fibers were subjected to a combination of gamma rays, fission spectrum neutrons and thermal neutrons [36]. The gamma ray dose

was assumed to be fairly uniform throughout the core, while the ratio of fast to slow neutrons depended on the location within the reactor. The schematic of the experimental layout is shown in figure 3.1. At the end of the experiment, the total gamma dose was estimated to be ∼22 kRad. The gamma ray dose was determined by placing commercial dosimeters in the rabbit tube (a pneumatic tube that enables placement of samples in the reactor core). Access to the fuel region, however, was limited so that no direct dosimetry is avaliable for this region.

The total neutron flux was determined by measuring gamma-ray activity in activated gold foils. Before the experiment, foils were activated in the fuel region and in the rabbit tube in a low-power run. The neutron-activation gamma-ray activity as a function of time was measured using Ge detectors, fitted to the known half-life and the activity at the time of irradiation was determined. The neutron flux was 1.3×10^{10} n/cm^2/s/kW and the thermal neutron flux was estimated to equal 8.5×10^9 n/cm^2/s/kW. The integrated neutron fluence at the end of the measurements was 1×10^{15} n/cm^2.

The design of the sample holders for the fibers was dictated by the geometry of the fuel elements of the reactor. The fibers were loaded into the sample holders with approximately 1/2 of the length of each fiber in 2-cm diameter loops and the remaining length straight. The entire sample holder was immersed in deionized water during reactor operations. Only the ends of the fibers were situated above the coolant water level. The temperature was not monitored near the fuel region and there may have been large temperature gradients, particularly because the sample holders were in contact with fuel elements. The reactor coolant, however, was maintained at 26.7^0C at all times via a set of automatic valves. The fibers were connected to 8 meter long transport fibers which were fed through the reactor shielding and connected to the xenon light source and spectrometer.

During the experiment, the power of the reactor was periodically altered to allow for irradiation of electronic components. This had an additional benefit of allowing us

to observe often an cited but not well-understood recovery phenomena, as we discuss later.

3.1.2 ATOMKI Cyclotron Neutron Source

18 MeV protons incident on a 3 mm thick cooled beryllium target generate neutrons with an average energy of 3.7 MeV in the forward region (see figure 3.2). The energy spectrum of neutrons ranges up to 20 MeV. The target current and the collected charge were measured during irradiation and were used to derive the flux rate and the neutron flux, using data from [37]. The diameter of the proton beam was 14 mm and the target current ranged from 20 to 24 μAmps. A pair of ionization chambers with different neutron and gamma response functions was used to monitor the mixed neutron-gamma field of the source and to estimate the gamma content. The total dose due to gammas was estimated to be 6.3 krad.

In the cyclotron measurements, the fibers were coiled around a 12 cm diameter cylinder and located 5 cm away from the neutron production target. The beam was perpendicular to the symmetry axis of the cylinder. The maximum neutron flux was at 0^o and at the end of a 25.3-hour period, the total fluence was 1.02×10^{15} n/cm^2 $\pm$18%. The average neutron fluence at the cylinder was estimated to be 0.6×10^{15} n/cm^2. During the irradiation, the dose rate was constant at 1.1×10^{10} n/cm^{2}sec $\pm$18%, except for a 13.26-hour down-time in order to change the ion source.

3.2 Analysis and Results

The usual expression for the attenuation in a fiber can be written as

$$A(\lambda) = A_0(\lambda) - \frac{10}{L} \log \frac{I_{irr}(\lambda)}{I_0(\lambda)} \tag{3.1}$$

where $A_0(\lambda)$ is the attenuation of the fiber (dB/m) prior to irradiation, L is the length

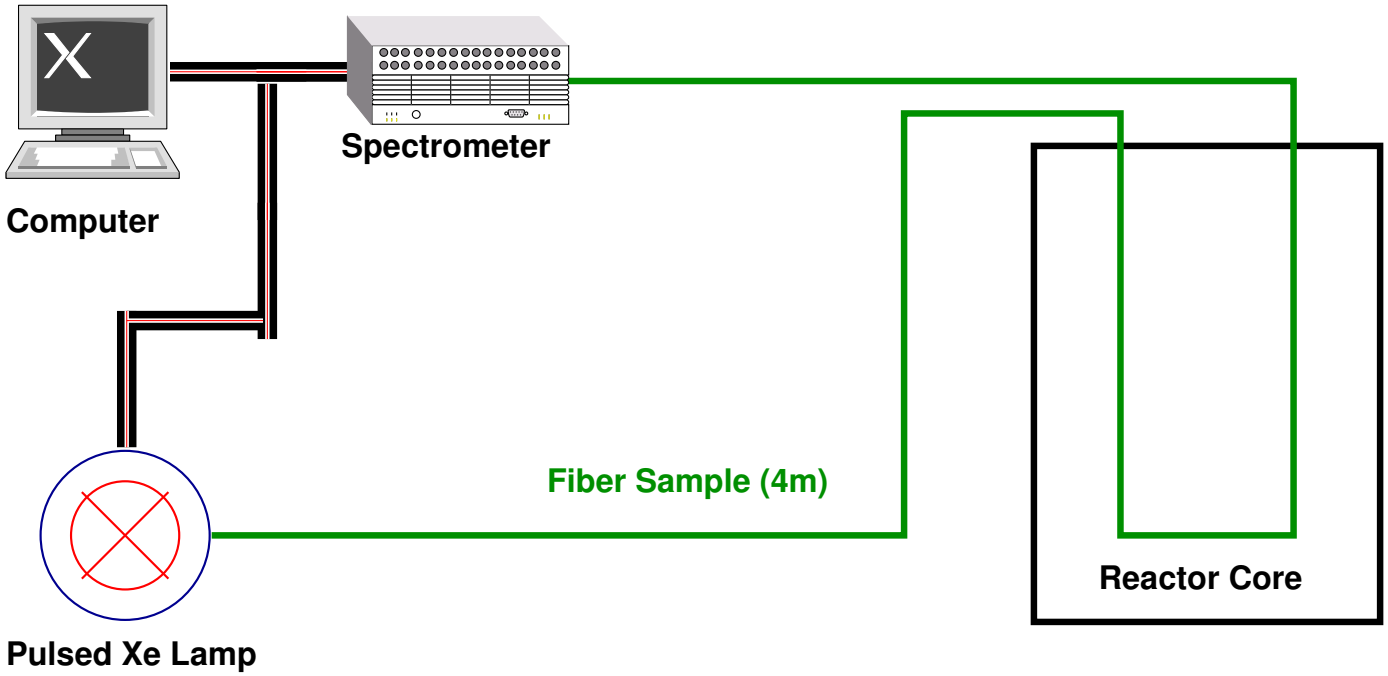

Figure 3.1: The sample fibers are placed close to the reactor core during the entire experiment. The light is injected from the Xe light source and transmitted through several meters of large diameter silica fibers before hitting the sample fibers; finally the transmitted light is transported once again with large diameter silica fibers and is analyzed by the spectrometer. The spectrum is stored in a personal computer for further off-line analysis.

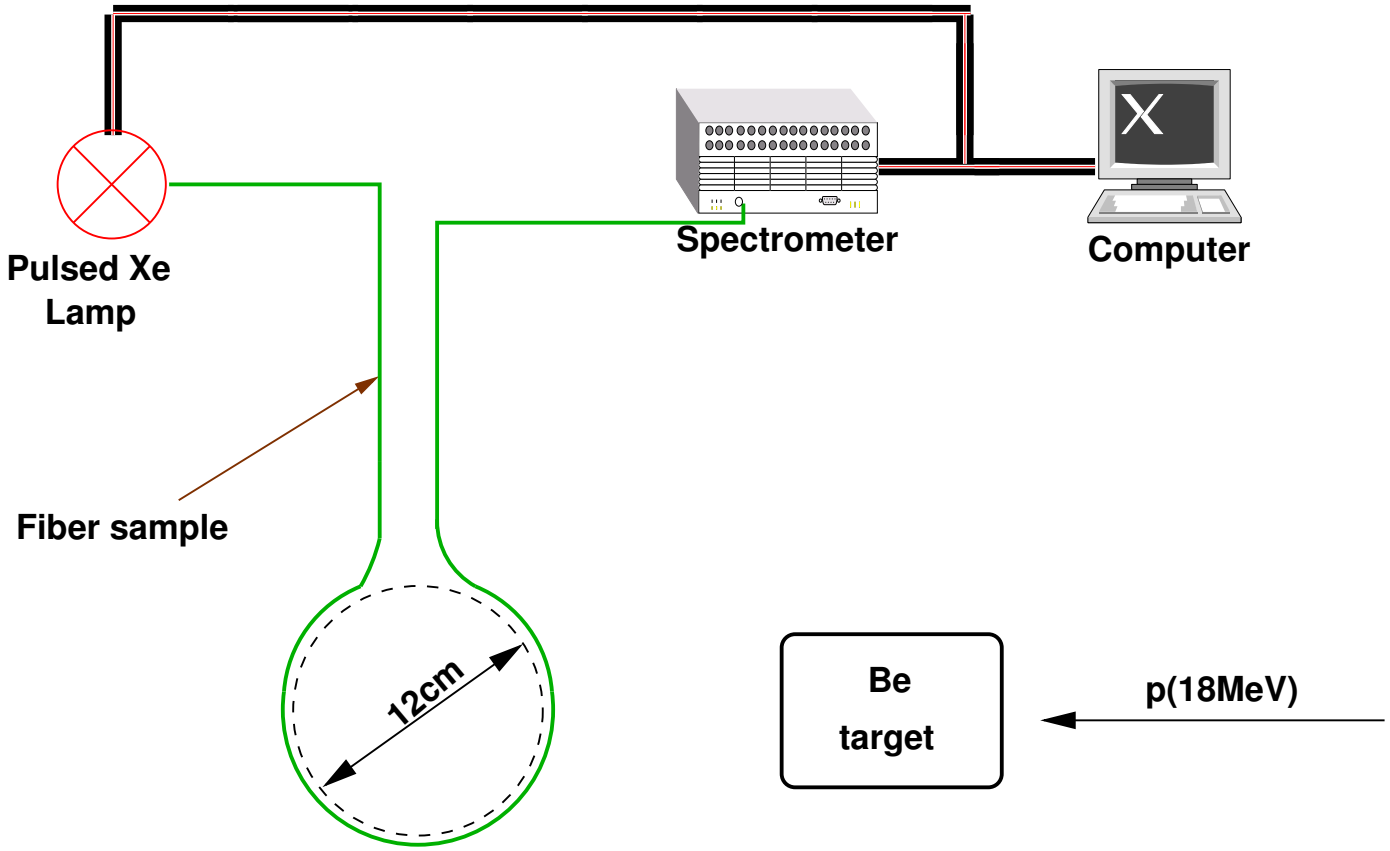

Figure 3.2: The sample fibers are coiled around a 12-cm diameter cylinder 5 cm away from the beryllium target. A similar set-up was used in ISU reactor tests.

of the irradiated fiber (in our case, typically 3-4 meters) and I_{irr} and I_0 are the spectral intensities measured for irradiated and unirradiated cases, respectively. The second term represents the irradiation induced loss in the optical transmission and hereafter we refer to it as induced loss.

In all cases, the spectral range studied was 325 nm to 800 nm. The intensity data were binned in 25 nm intervals and the average values are used in calculations and figures.

In the near-UV and visible spectral regions, the radiation induced absorption bands in silica-core fibers can be grouped in the following manner:

1. The prominent absorption band in the range $\sim 600 - 630$ nm is interpreted to originate from non-bridging-oxygen hole centers (NBOHCs). The NBOHC is a molecular structure where a silicon atom is bonded to four oxygens and one of them carries an unpaired electron, $\equiv \mathrm{Si} - \mathrm{O}\cdot$. It was shown that a large γ-induced absorption band arises with F-doped silica-clad fibers compared to polymer clad fibers [5]. By progressive etch-back of F-doped silica-clad fiber and electron spin resonance (ESR), it was demonstrated that NBOHCs are located largely in the core-clad interface. The origin of these excessive NBOHCs then may be the conversion of paired hydroxyl groups near the surface of the core rod into peroxy linkages during the plasma deposition of the F-doped cladding. The peroxy linkages would serve as NBOHC precursors by breaking the $\mathrm{O} - \mathrm{O}$ bond. If this argument holds true, the production of radiation-hard fibers would mean exclusion of OH groups and peroxy linkages from the core rod. NBOHCs have a luminescence band at around 670 nm.

2. The attenuation tail that extends from near-UV to visible, the so-called UV tail, has several origins, however the strongest color center that contributes to this absorption band comes from chlorine impurities as verified by ESR studies [6].

3. E′ center, one of the most studied defects in SiO_2, ($\equiv$ Si·), has an absorption peak at 212 nm and a luminescence at 450 nm. These color centers are produced in glasses by energetic irradiation and during the fiber drawing process [7].

4. It is worthwhile to note that different color centers may interact with each other and that they display different characteristics than what is listed above when irradiated [8].

3.2.1 Reactor Data

The spectral dependence of irradiation induced loss for the FSHA fiber shown in figure 3.3 displays a characteristic behavior common to most irradiated optical silica fibers. The near-UV region shows a rapid transmission loss with irradiation. In the 400-500 nm band, there is a soft dip, and around 600 nm there is an absorption band ascribed to NBOHCs. In the range of 700-800 nm, the attenuation increase due to irradiation seems affected the least. This feature has been observed by others for high OH content fibers [9].

The FIA-type fiber, Figure 3.4, exhibits a different damage profile. The induced losses are higher, 8 dB/m at 450 nm, for similar neutron fluences compared to the FSHA-type fiber. The hydroxyls may not be readily terminating and deactivating the color centers due to reduced OH concentration (less than 1 ppm) in the core material. There is a shift in the absorption band peak from $\sim$ 390 nm at a fluence of 1.04×10^{13} n/cm^2 to 460 nm at an increased fluence of 7.78×10^{14} n/cm^2. The attenuation behavior in the region between 300 nm to 400 nm is rather uncharacteristic. It is possible that the luminescence band at 450 nm from E′ oxygen-vacancy centers contributes to light emission and effectively reduces the attenuation here, but this region will have to be studied further.

The reactor could only be operated during the day for an 8-hour period. Figure

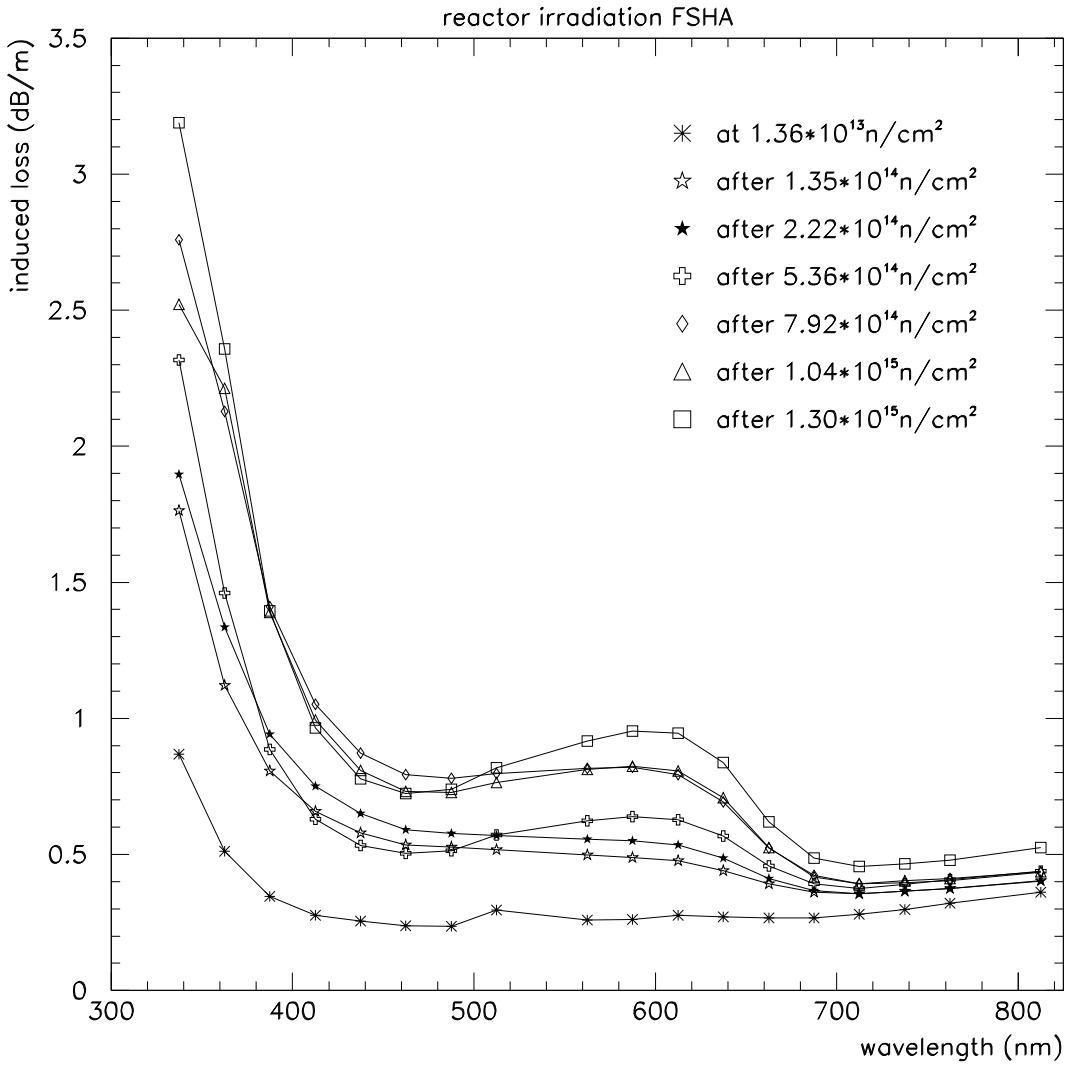

Figure 3.3: Neutron irradiation induced loss for the FSHA-type fiber reaches 1 dB/m after 1.3×10^{15} n/cm^2 at 600 nm at the reactor. In $400 \leq \lambda \leq 500$ nm range, the loss is on average less than 1 dB/m.

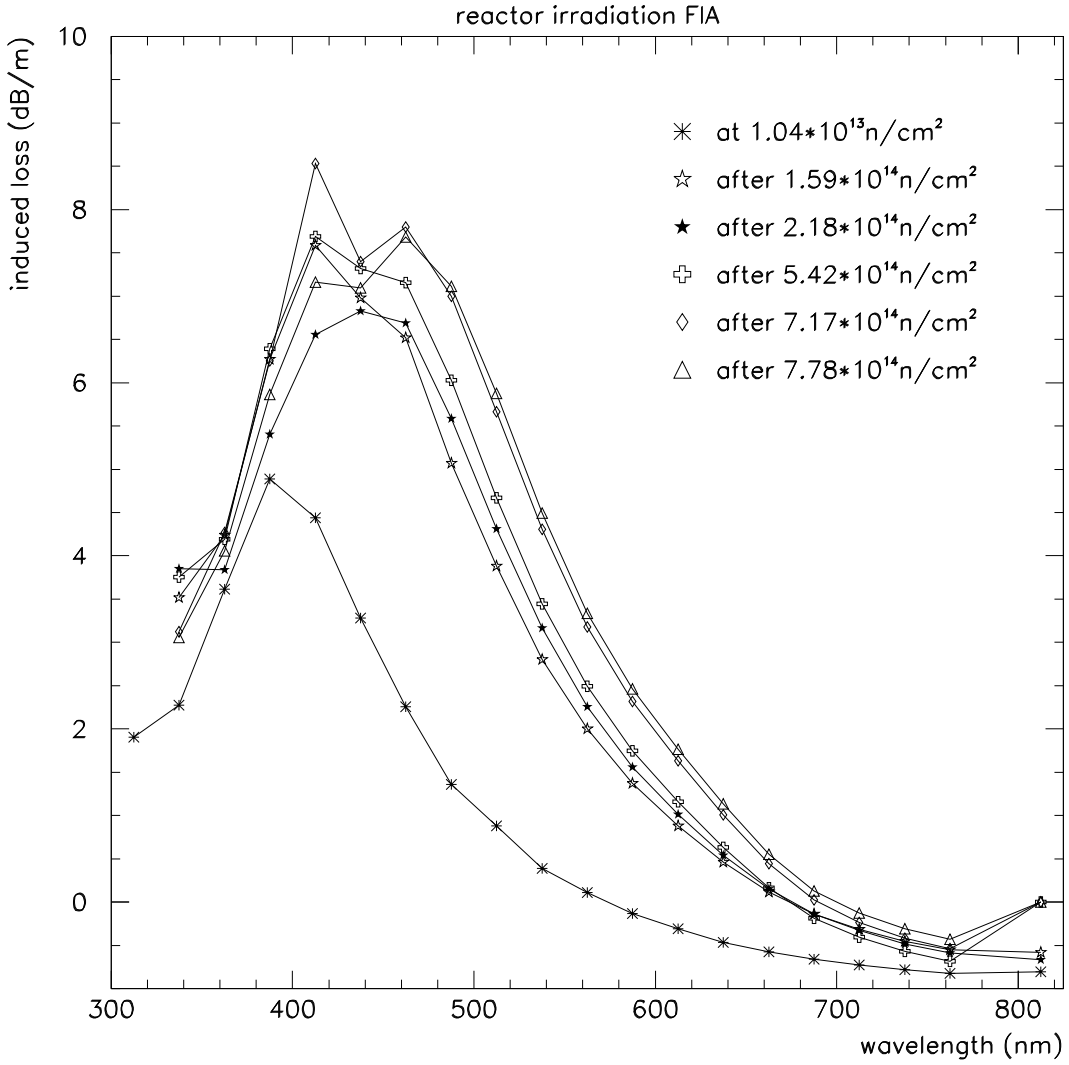

Figure 3.4: Neutron irradiation induced loss reaches 8 dB/m at 450 nm for the FIA-type fiber after 7.8×10^{14} n/cm^2 at the ISU reactor.

3.5 shows the history of the reactor operation in terms of the induced loss in the FSHA-type fiber. Although there are many parameters that contribute to the behavior in this figure, it is interesting to note that the attenuation reflects the neutron fluence (or more precisely the reactor power) at a given time and that the recovery occurs rather quickly when the power in the reactor is reduced or shut down (as on the second half of the first day). The increased attenuation is quickly restored, however, when the fibers are irradiated again (see the beginning of the third day, for example).

From figure 3.3, one can see the dynamic characteristic of the optical fiber. The first three spectra are taken in day one (see the arrows in Figure 3.5). The induced loss increases as the integrated neutron fluence increases for all wavelengths. The first measurement in the beginning of the second day after an over night shut-down, (indicated by open crosses) shows recovery in shorter wavelengths. The same effect is observed in the beginning of day three (going from open diamonds to open triangles in figure 3.3).

In order to extract the kinetic behavior of attenuation with accumulated dose or neutron fluence, we fitted the data to a function of form aD^b, Figure 3.6. Table 3.2 summarizes the results. As is clearly seen from Figure 3.6, there are no saturation or quasi-saturation effects that would signal exhaustion of the precursors that turn into color centers. Power-law behavior suggests the activation of precursor species (and sub-species) as the dose accumulates. It is suggested in [10], however, that the silica fibers would reach their fully radiation densified state for fast neutron fluences of $\sim 10^{20}$ n/cm^2.

Within the experimental accuracy, the parameter b is the same for 400, 425 and 500 nm for both type FSHA- (high OH) and FIA-type (low OH) fibers. At 600 nm, however, presumably due to NBOHCs and the low OH content of the FIA-type fiber core, the FIA-type degrades more readily ($b \approx 0.43$) when compared to the FSHA-type fiber ($b \approx 0.26$). Similar values are reported $b = 0.295$ in [11] and $b = 0.263$ [12] for pure silica-core optical fibers.

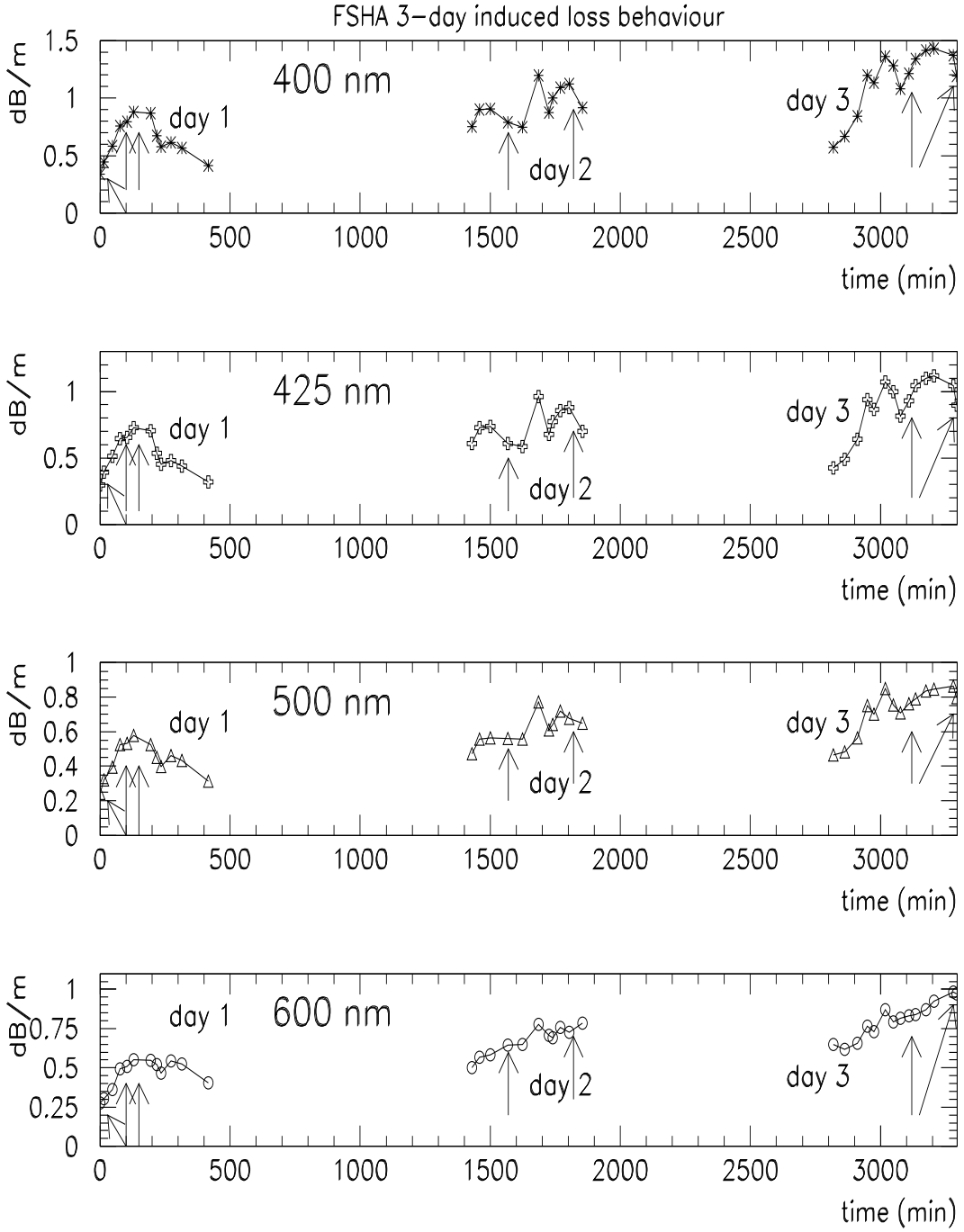

Figure 3.5: FSHA-type fiber induced loss curves at five different wavelengths show the power history of the reactor.

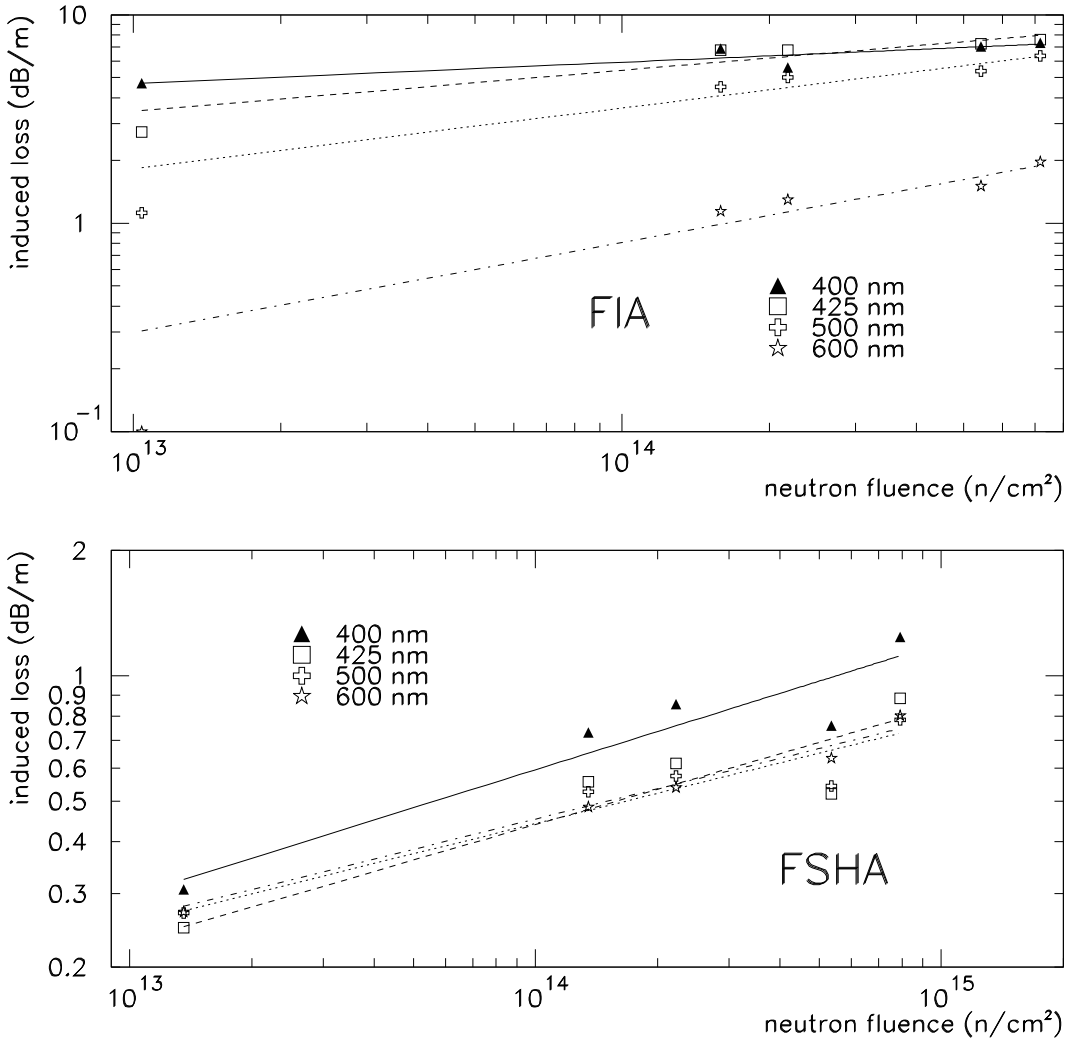

Figure 3.6: The power-law dependence of induced loss on neutron fluence is shown above for the FIA- and FSHA-type fibers. Within the experimental accuracy, the induced loss scales as D^b, where D is the neutron fluence. The solid (400 nm), dashed (425 nm), dotted (500 nm) and dash-dotted (600 nm) lines are fits to data.

Table 3.2: Power-law behavior of irradiation induced loss with accumulated neutron fluence is shown by the fit parameters to a functional of type aD^b, where D is the neutron fluence. The parameter b is calculated at four wavelengths for FSHA, FIA and IN-type fibers.

ID	400 nm	425 nm	500 nm	600 nm
FSHA	0.21	0.21	0.21	0.26
FIA	0.20	0.20	0.29	0.43
IN	0.35	0.34	0.59	0.69

3.2.2 Cyclotron Data

Figure 3.7 shows the induced loss for the IN-type fiber for fast neutrons. The UV-tail and the absorption band at around 630 nm are clearly observable, much like in figure 3.3. At 10^{15}n/cm^2, the induced loss in the region of interest is about 1 dB/m. The cyclotron down-time occured towards the end of the irradiation, after an integrated neutron fluence of 7.48×10^{14} n/cm^2. It should be noted that the next measurement (shown as open triangles), in shorter wavelengths ($\leq$500nm), shows less induced attenuation even though the total fluence is higher, indicating recovery during 13.26 hour shut down. The same phenomena was already discussed in the reactor experiment in previous section.

Table 3.2 shows that for the IN-type fiber the parameter b tends to be >50% higher for the same wavelengths compared to FSHA and FIA fibers. There may be several reasons for this: The more energetic neutrons from the cyclotron may be more damaging compared to the mostly low-energy neutrons from a reactor, or the constant neutron dose rate may induce more optical loss, or it may simply be due to a characteristic of IN-type fiber.

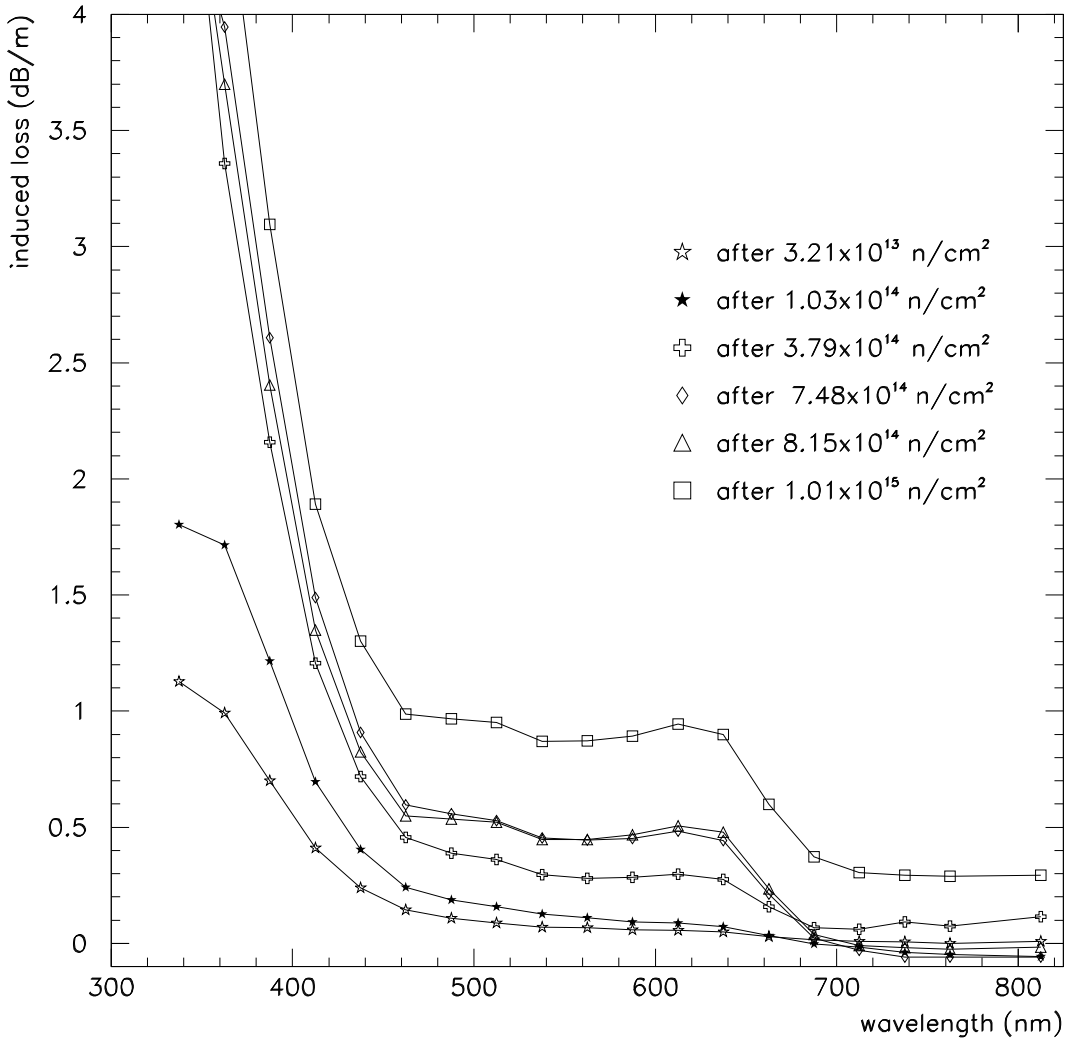

Figure 3.7: The neutron irradiation induced loss at 600 nm is about 1 dB/m for IN-type fiber at the ATOMKI cyclotron. The neutron rate was kept constant at 1.1×10^{10} n/cm^{2}sec $\pm$ 18%, except for a 13.26 hour down-time in order to change the ion source. After 7.48×10^{14} n/cm^2, note that the next measurement (open triangle), in shorter wavelengths ($\leq$ 500 nm), shows smaller induced loss, indicating recovery during the shutdown.

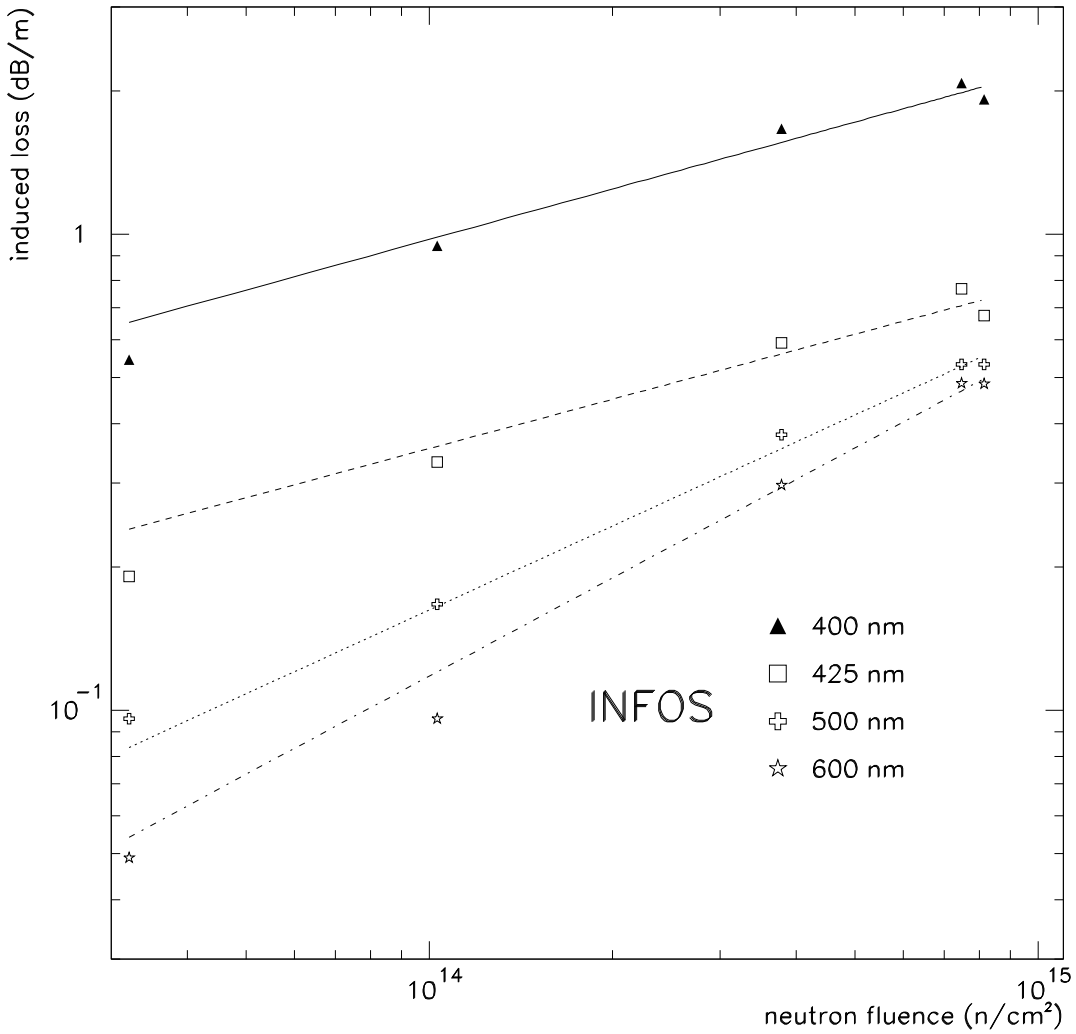

Figure 3.8: The power-law dependence of induced loss on neutron fluence is shown above for the IN-type fiber. The induced loss scales as D^b, where D is the neutron fluence and the exponent b is typically 0.35 to 0.69. The solid (400 nm), dashed (425 nm), dotted (500 nm) and dash-dotted (600 nm) lines are fits to data.

3.3 Recovery of Damage

Essentially, all silica-core fibers tend to recover to varying degrees. In Table 3.3, the time constants are evaluated assuming an exponential behavior in the form of $e^{-t/\tau}$. There are undoubtedly several processes that contribute to recovery phenomena. Our intent is to characterize a gross time scale for this behavior. Similar time constants are reported in [13]; from the data presented in [14], we calculate $\tau \sim 10^4$ seconds for silica-core fibers in the green wavelength region. It is also noteworthy that as Table 3.3 and data in [14] suggest, the recovery takes place faster in 400-500 nm band for polymer clad fibers (FSHA), compared to silica-clad fibers.

Table 3.3: Recovery time constants, τ (sec), are calculated at four wavelengths.

ID	400 nm	425 nm	500 nm	600 nm
FSHA	7560	6780	17100	17100
FIA	15360	9960	6540	7200
IN	9650	11760	10640	11410

Figures 3.9 and 3.10 show the recovery in the optical transmission for the FSHA- and FIA-type fibers.

3.4 Results and Discussion

Some recovery is observed in most silica fibers [15]. A typical time constant is of the order 10^3 to 10^4 seconds. Once the radiation is reapplied to the fibers, the color centers are quickly reactivated and the optical characteristics return to the same state as at the end of irradiation. No permanent recovery is observed [9].

The importance of *in situ* optical measurements is manifested by the recovery data

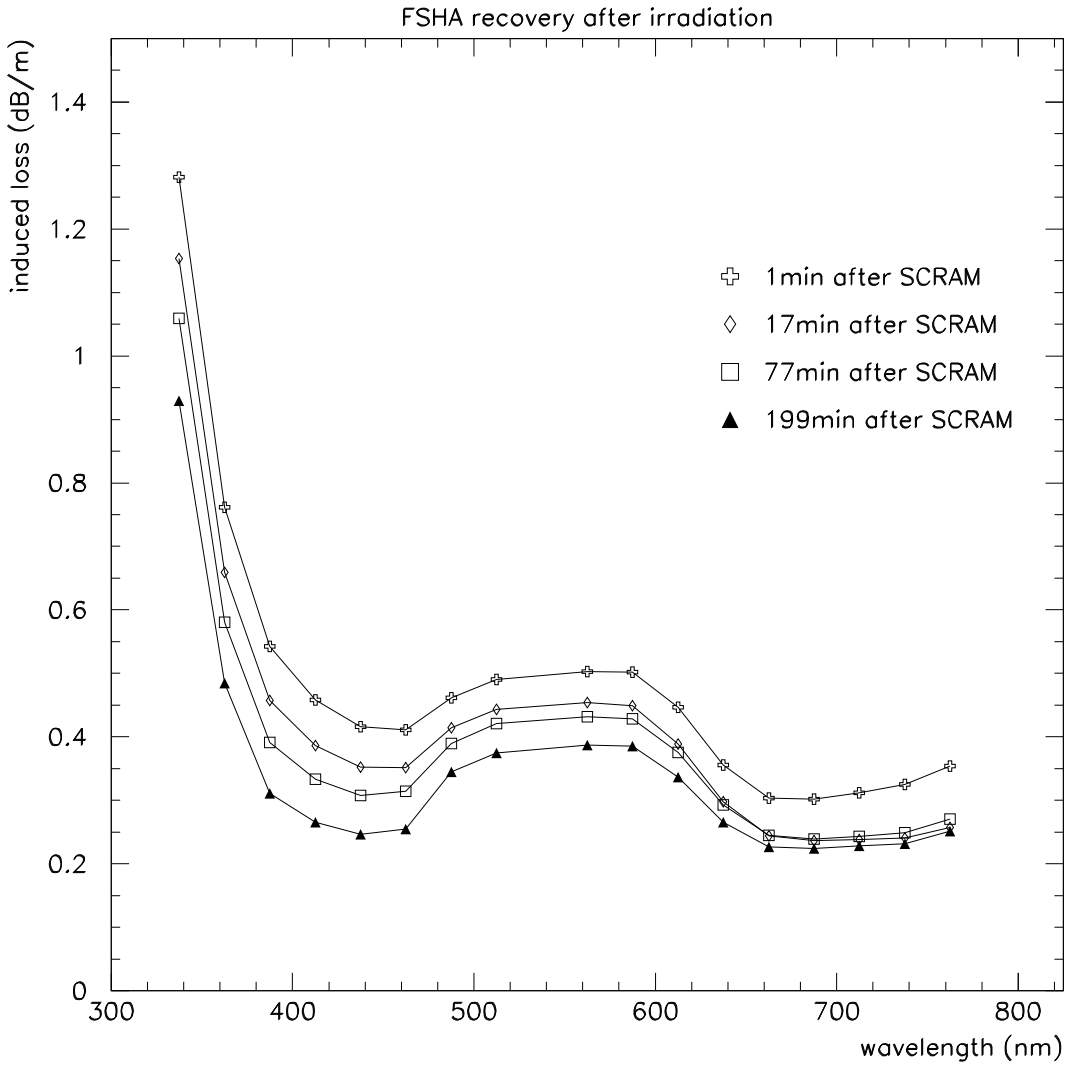

Figure 3.9: The post-irradiation optical transmission recovery of the FSHA-type fibers shown above at four different times at the end of the third day of reactor operation. Note that there is a speedy recovery after 1 minute (from 1 dB/m to 0.55 dB/m at 600 nm) and that the spectral damage profile is, to a large extent, maintained during the recovery process. SCRAM refers to reactor shutdown.

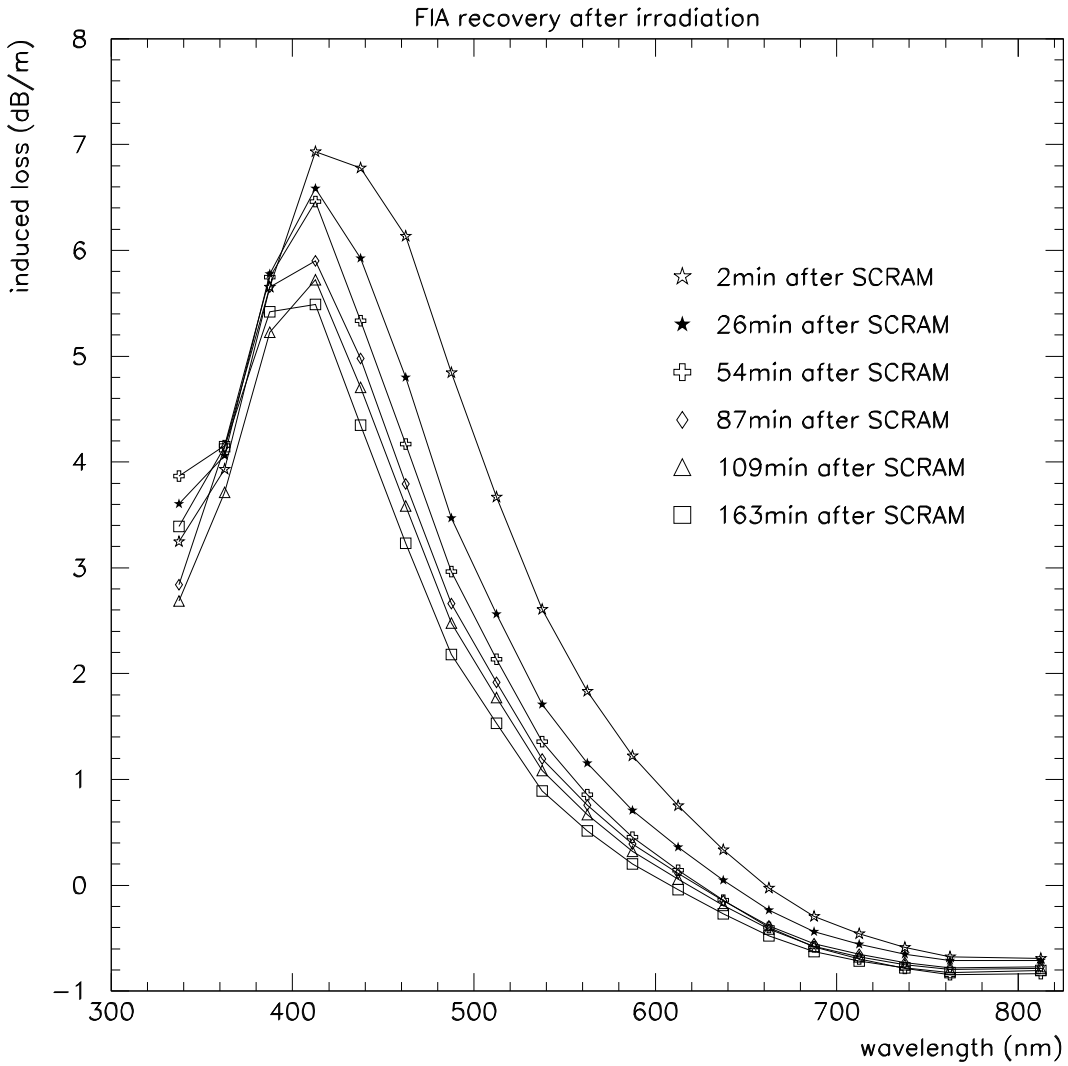

Figure 3.10: The post-irradiation optical transmission recovery of the FIA-type fiber is shown above at six different times at the end of the third day of reactor operation. Note that there is a speedy recovery after 2 minutes, and the recovery profile follows the damage profile back in time.

presented here. This is particularly important for calorimetry and the calibration of the forward calorimeter. The neutron rate at the cyclotron was constant at 10^{10} Hz/cm^2; and at the reactor, the rate varied but the average rate over the course of three days was 6×10^9 Hz/cm^2. These rates are more by one or two orders of magnitude compared to what is expected by the MARS [16] code in the front of the HF [17].

The luminescence properties of the fibers need to be studied in detail and their effect on the calorimeter performance should be addressed.

For the same IN-type fiber, $<$ 10 MRad γ-irradiation seems to have generated a similar type of optical damage as neutron irradiation at a fluence of 10^{15} n/cm^2 [38]. More detailed comparisons between these data sets can be misleading since the experimental systematics may be quite different.

The intent of these initial neutron irradiation studies was to establish a general method of testing individual fibers which was specifically aimed at the needs of the forward calorimeter.

CHAPTER 4
RADIATION DAMAGE AND ACTIVATION STUDIES AT THE LIL FACILITY OF CERN

The CMS forward calorimeter consists of multi-mode synthetic silica-core optical fibers embedded in an iron absorber. In the previous sections we presented the studies we carried out to understand the effects of the radiation on quartz fibers. In order to study the response of the forward calorimeter under the expected intense radiation conditions, we performed dose and activation measurements in iron absorbers after irradiating them with a 500 MeV electron beam at the LEP pre-injector (LPI) facility at CERN. We made Monte Carlo calculations to compare them with the data in an attempt to generalize and to use these results for the radiation damage studies of the prototypes irradiated at the same facility.

The details of the lateral and longitudinal dose profiles in the calorimeter absorber determine the magnitude and extent of the radiation damage in quartz fibers. The radiation dose degrades the optical transmission in quartz fibers and worsens the response of the detector. In the 400 nm to 500 nm range, for example, the irradiation induced transmission loss reaches $\sim$ 1dB/m for 100 MRads for most synthetic silica-core and fluorine-doped silica-clad fibers.

The CMS forward calorimeter absorber material(s) will become activated under the intense LHC radiation fields. After two months of running at an average luminosity (5×10^{33} cm^{-2}sec^{-1}) and a day of cool-down period, the activation level is estimated to be several thousand $\mu Sievert/hour$ at the higher rapidity region. In addition to safety and maintenance concerns, this background introduces noise into the calorimeter system. In the case of the iron absorber (Fe I), as this study shows, $\sim$110 MRad dose from electrons results in 6.5 MBq of total activity at the shower maximum after about

an hour of cool down.

4.1 The Iron Absorber Structures

4.1.1 First Iron Matrix (Fe I)

Figure 4.1 shows the structure of the first iron matrix. The total length of the absorber is 206 mm (11.36 X_0), deep enough to fully contain 500-MeV electron showers. The iron plates are positioned normal to the beam direction; the first four plates are 1 cm and the last eight are 2 cm thick with respect to the beam direction. They measure 40 mm $\times$ 40 mm on a side. Between each plate, a 0.5-mm thick (0.396 gr/cm^2) Fe plate and a radiation sensitive (RISO) [18] paper are placed. RISO paper consists of a thin plastic film containing a radio-chromic dye (leucocyanide) which induces intense permanent colors when exposed to ionizing radiation. Like most cyanides, luecocyanide is colorless but upon irradiation, the cyanide bond is broken and the positive carbonium ion becomes colored. The 0.5-mm thick Fe plates were used for the activation measurements and the RISO sheets registered the integrated dose. These thin Fe plates are of identical chemical composition as the thicker ones. There was no air gap between the plates and/or the RISO paper.

4.1.2 Second Iron Matrix (Fe II)

The second iron matrix was constructed in order to study the lateral shower development in a wider range in detail; thus the transverse absorber dimensions measured 16 cm $\times$ 16 cm. In addition to the RISO papers sandwiched between plates, we embedded glass RPL dosimeters in small holes in some of the iron plates (indicated as shaded plates in Figure 4.2). RPL (RadioPhotoLuminescent) technique is based on generation of color centers under irradiation in specially prepared glasses. These color centers can be activated by ultraviolet light and the subsequent luminescence can be recorded to

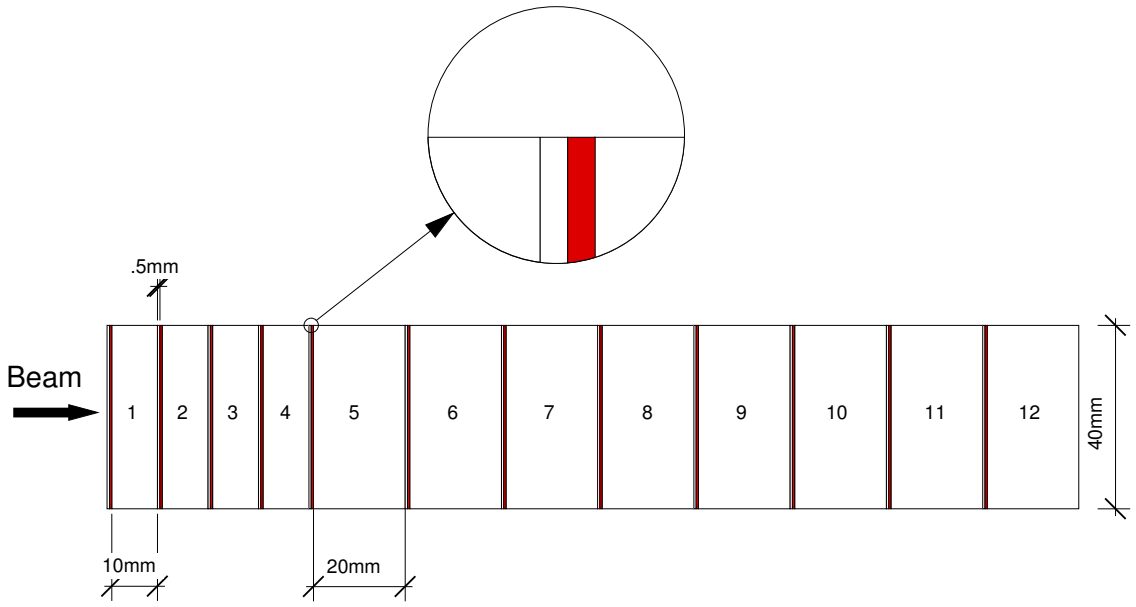

Figure 4.1: The iron matrix consists of a sandwich of thin (0.5 mm) iron plates, sheets of radiation sensitive RISO paper (indicated as dark lines) and thicker iron plates (10 or 20 mm) as shown. Twelve such units make up the entire Fe I absorber matrix. The total depth of the stack is 206 mm, sufficient to contain all of the energy from 500 MeV electrons. The transverse dimensions are 40 mm by 40 mm.

indicate the absorbed dose. The glass samples we used were typically 0.5 mm in diameter and 5 mm in length. In addition, in order to investigate the characteristics of lateral activation profile, 0.5 mm thick and 1.5 cm diameter disks were placed inside the absorber as shown in Figure 4.2. By this construction, we were able to measure the details of the lateral activation as well as longitudinal profiles, whereas with the first iron matrix (Fe I) we could only measure the total activation as a function of depth.

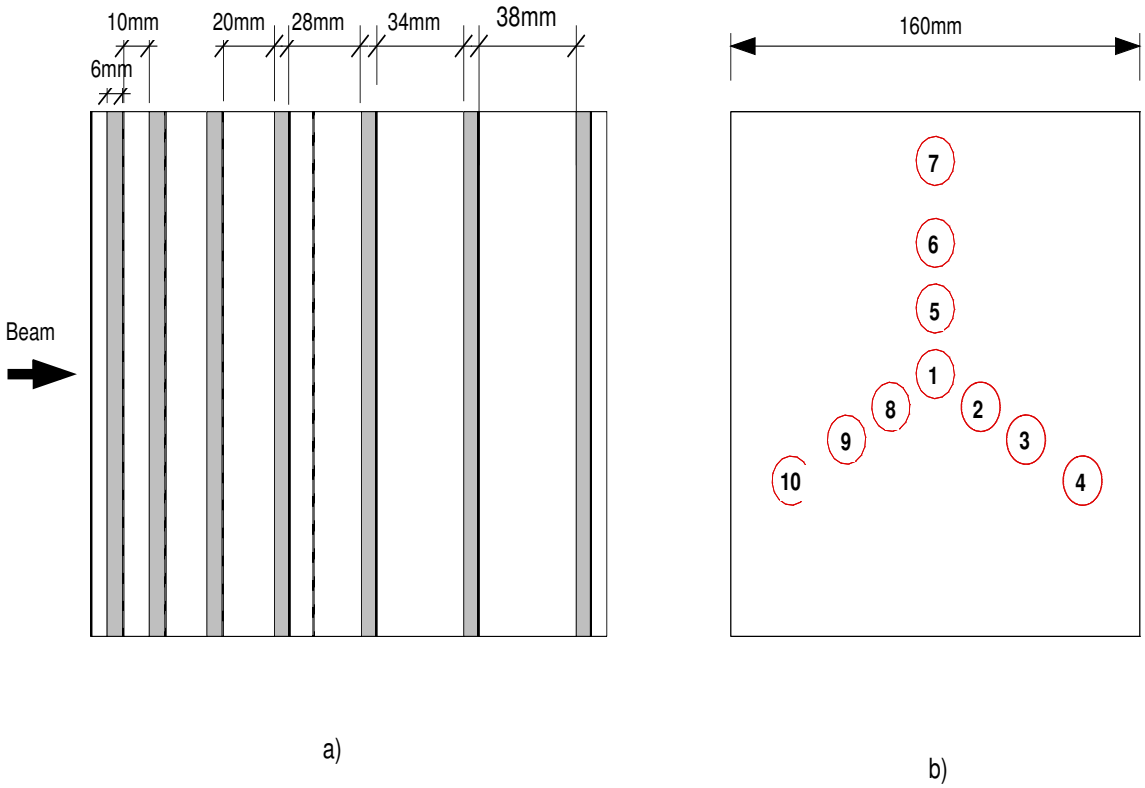

Figure 4.2: The second iron matrix (Fe II) consists of a sandwich of iron plates and sheets of radiation sensitive RISO paper. The RISO paper locations are shown in dark lines. The total depth of the stack is 200 mm. The transverse dimensions are 160 mm by 160 mm. b) For lateral activation studies, we used a 0.5 mm thick sheets (shown as shaded lines in a), where ten 1.5 cm diameter disks were located in the shape shown. From the center (disk 1), the center of disks 2, 5, and 8 are at 2 cm, the disks 3, 6 and 9 are 4 cm and the disks 4, 7 and 10 are 6.5 cm away.

Table 4.1: Impurities in the iron blocks.

Block	C(%)	Mn(%)	P(%)	S(%)
Fe-I	<0.10	<0.45	<0.035	<0.035
Fe-II	<0.17	0	<0.045	<0.045

4.2 LEP Pre-Injector (LPI) Beam

There is a ten-year time scale planned for the LHC experiments and the expected radiation doses are measured in many megarads. The existing facilities that are able to provide comparable integrated doses in practicable times are low-energy but intense particle beams. One such facility is the LIL Experimental Area (LEA) at CERN [19], which can provide up to 700 MeV electrons in a dedicated facility of the LPI, downstream of the linac. The samples are placed on a remotely controlled table, 2 meters downstream of a 0.1 mm (Al) thick vacuum window. Its contribution to the diffusion is 3.2 mm (RMS) in both planes at the location of the irradiation sample. The beam can be steered with a set of dipole magnets in a 10 cm by 10 cm area at the sample location. The integrated charge is measured by a beam position monitor just upstream of the exit vacuum window. Table 4.2 gives the nominal beam characteristics.

The first absorber matrix was exposed to beam for 3 hours and 11 minutes, collecting 1.68×10^{15} electrons at a constant rate. The second iron block accumulated 2.73×10^{15} electrons in 34 minutes due to a higher number of cycles. The beam was centered at the geometric center of the absorber at all times.

4.3 Dosimetry

RISO sheets were placed in the absorber structures (Figures 4.1 and 4.2) and were analyzed in 3 mm $\times$ 3 mm square grids. The typical precision of dose measurements

Table 4.2: Nominal beam parameters were used for this irradiation study. LPI can provide intense electron beams in a wide energy and intensity range and is especially well-suited for radiation damage studies of electromagnetic calorimeters. Note that beam sizes were slightly different for the first and the second iron block irradiations. We account for this difference in the simulation and dose calculations.

Parameter	Range	Nominal (for these tests)
Energy (MeV)	$180 - 700$	500
Charge/Pulse (e^-)	$5 \times 10^8 - 2 \times 10^{10}$	4×10^9
Frequency (Hz)	$1 - 100$	100
Pulse FWHM (nsec)	$10 - 40$	10
RMS Beam Size (mm)	$\sigma_x = 3.3 - 6.0$	$\sigma_x(\text{FeI}) = 4.7$
		$\sigma_x(\text{FeII}) = 3.4$
	$\sigma_y = 3.3 - 6.0$	$\sigma_y(\text{FeI}) = 3.6$
		$\sigma_y(\text{FeII}) = 3.3$

using this technique is ±20%. The glass RPL dosimeters were placed in small holes in the absorber, as mentioned in Section 4.1, and later analyzed. We assume ±20% uncertainty in these measurements. The RPL dosimeters are well-suited and reliable at lower doses. We depended on RISO paper measurements for doses that exceed ~ 1 kGray[1].

Figure 4.3 shows the longitudinal development of 500 MeV electrons in iron. The dose is normalized to 1.0×10^{15} electrons and at the shower maximum, the total dose is ∼660 kGrays. The data from Fe I and Fe II blocks are presented in the same figure. The longitudinal shower profile is usually expressed by a simple parameterization [20],

$$\frac{dE}{dz} = kz^{\alpha-1} \exp(-\beta z) \tag{4.1}$$

[1]One gray is equal to one joule of energy deposited by any type of radiation in one kg of a material

where z refers to the longitudinal coordinate and k is a normalization constant. The parameters α and β define the shower shape. The shower maximum takes place at

$$z_{max} = (\alpha - 1)/\beta. \tag{4.2}$$

The smooth solid line in Figure 4.3 is a fit to the data points according to Eq.(4.1). As known, in the first few radiation lengths, this simplified expression neither represents the data nor the simulation results well [21]. When the first two data points are excluded from the fit, it suggests a shower maximum at 2.7 cm. The simulation however suggests $z_{max} = 3.5$ cm as represented by the connected open circles in Figure 4.3. The agreement between the data, fit and the simulation improves after $z \geq 4$ cm. The simplified fit to the shower shape, Eq.(4.1), should be viewed with some caution since it underestimates both the dose at the shower maximum by $\sim 40\%$ and its location, z_{max}, by 20%.

Figure 4.4 shows the shower development at two different off-shower axis locations, 0.95 and 1.95 cm. The agreement between the data and the simulation results is good except the last two data points at 19 cm.

The characteristic parameter for lateral shower profiles is the Molière radius, R_M, defined as,

$$R_M = \frac{E_s}{E_c} X_0 \tag{4.3}$$

where $E_s \approx 21.2$ MeV, E_c is the critical energy and X_0 is the radiation length. We take $E_c^{Fe} = 22.4$ MeV and $X_0^{Fe} = 1.76$ cm.

On average, in one Molière radius ($R_M^{Fe} = 1.67$ cm), 90% of the energy is expected to be absorbed in an infinitely long absorber. 99% of the energy is absorbed in 3.5 R_M. The electromagnetic shower consists of a narrow and energetic core, and a wide halo surrounds it. As the shower develops, the core broadens. The lateral shower development as a function of depth is shown in Figure 4.5 for four different depths, 1 cm ($0.57X_0$), 3 cm ($1.70X_0$), 5 cm ($2.84X_0$) and 15 cm ($8.52X_0$). *EGS4* [22] reproduces the RISO data

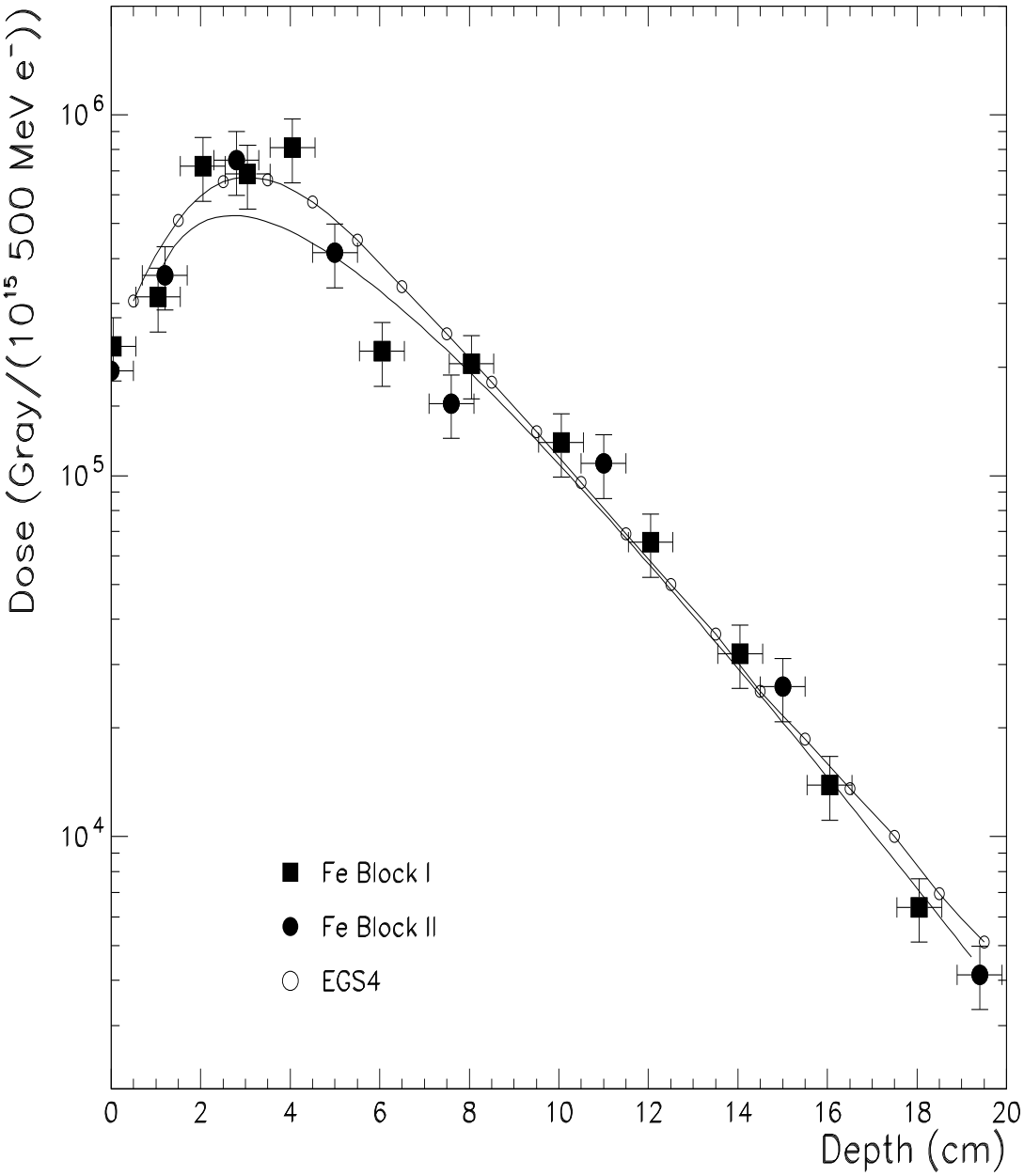

Figure 4.3: The longitudinal shower dose profile for 500 MeV electrons in iron is measured using radiation sensitive (RISO) paper and represented by filled squares (Fe I) and circles (Fe II). The solid line is a fit to the data points which gives $\alpha = 2.14$ and $\beta = 0.42$ cm^{-1}. The connected open circles represent the *EGS4* simulation result. All values are normalized to 1.0×10^{15} electrons.

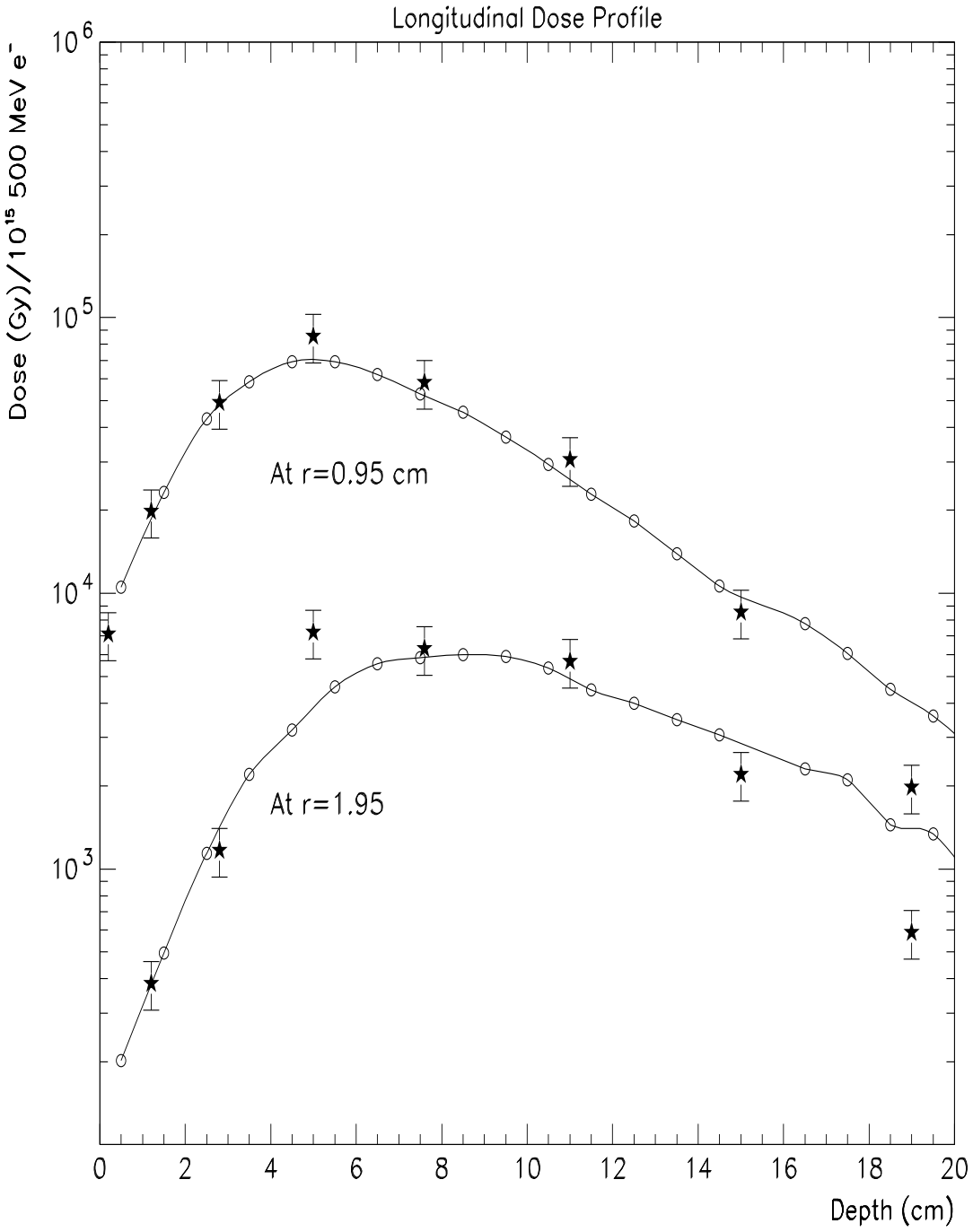

Figure 4.4: The longitudinal shower profile is shown at two off-axis shower positions (r = 0.95 and 1.95 cm) in iron for 500 MeV electrons. The stars are the RISO paper data and the connected open circles refer to the simulation results.

well in all depths and RPL data up to 5 cm depth. It is worthwhile to note that the energy threshold for gammas and electrons was set at 100 keV and 1.5 MeV in EGS4, respectively, for this lateral development study. When these thresholds were reduced to 10 keV for photons and 50 keV for electrons, there was no appreciable difference. The lateral shower profile within one R_M is not significantly sensitive to these cuts; but it is natural to expect that these cuts would be important for $r > R_M$, because of the fact that photons (bremsstrahlung and annihilation) will travel farther from the shower axis compared to electrons. The published data at similarly low energies are scarce; at 6 GeV, for instance, the comparison between Monte Carlo and data starts after the depth of 5 X_0, *i.e.* after the shower maximum [23]. When quoted at shallower depths ($\sim 2X_0$) by a different study at 1 GeV, the agreement between the data and simulation is poor [24]. In [25], the simulation underestimates the radial energy escape at 900 MeV – by a factor of two at one R_M. This is attributed to the annihilation photons that tend to penetrate larger distances from the shower axis and was not included in the simulations. It is also argued that the lighter the absorber material, the larger is the disagreement [26].

4.4 Activation Analyses

The reasons for performing activation studies were two-fold: To measure the activation levels of the iron absorber subjected to an intense electron beam and to attempt to measure the longitudinal shower profile using these data. In doing so, we have identified the active isotopes and their levels of activation and also observed that the activation profile along the depth of the detector is a good measure of average gamma profiles and energies within the absorber. We also attempted to determine the lateral activation profile for a given depth as depicted in Figure 4.2.

Less than an hour after the irradiation of the Fe I absorber matrix, the activation measurements were carried out to identify the relatively short-lived isotopes using the

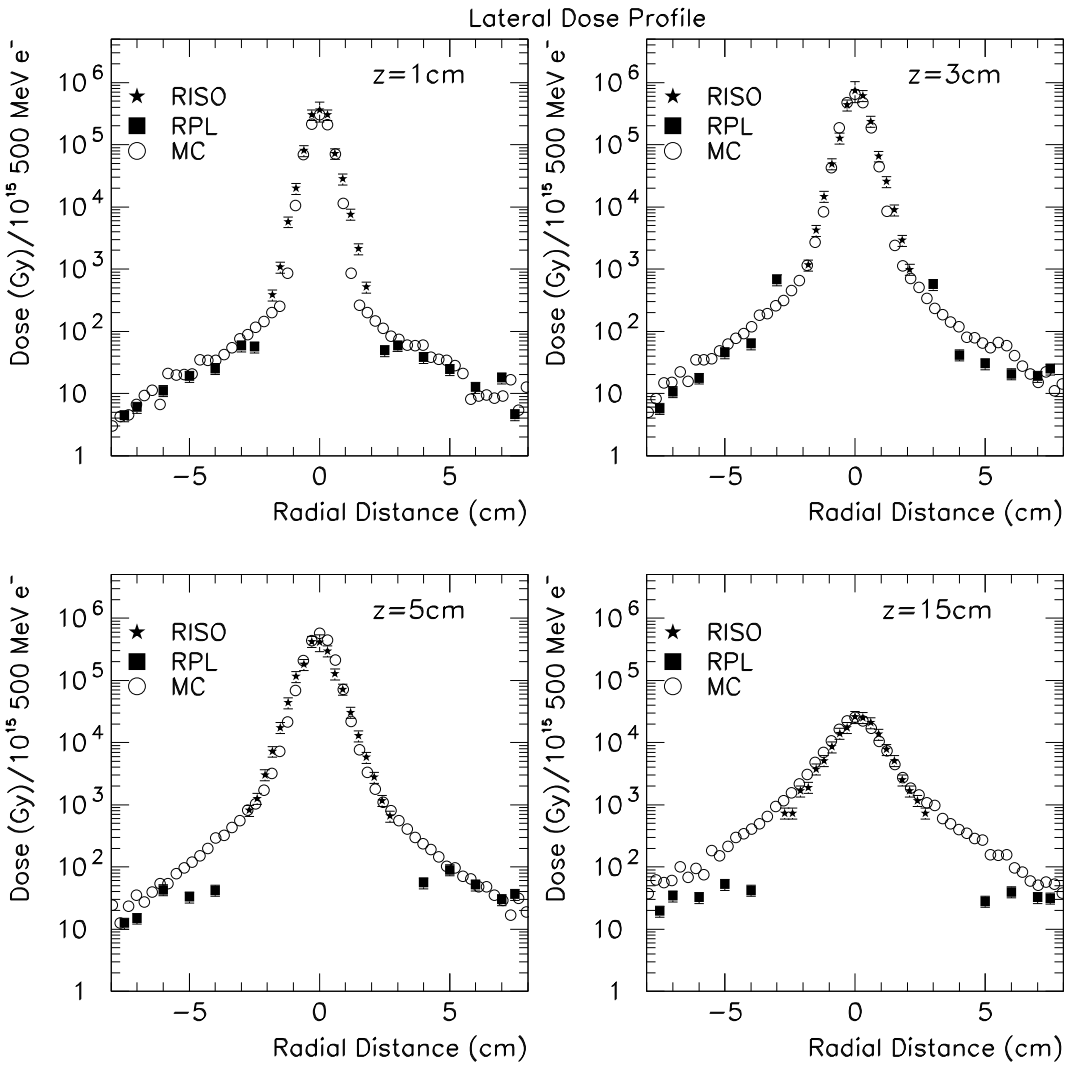

Figure 4.5: The lateral shower profile is shown for four depths ($z = 1, 3, 5$ and 15 cm) in iron for 500 MeV electrons. The black stars and squares are the dosimetry data and the open circles refer to the *EGS4* simulation results.

Table 4.3: The measured activity of 0.5-mm thick Fe plates placed at different depths in the iron absorber matrix (Fe I). The activity is indicated in kBq where measured. The column numbers correspond to the plate numbers in Figure 4.1.

Isotope	1	2	3	4	5	6	7	8	9	10	11
Na^{24}		1.4	1.1								
Cl^{38}	1.1	3.3									
Ar^{41}	0.5	2.4	1.7	1.3	1.1	0.5					
K^{42}		18.7	17.1	11.7	8.0						
K^{43}	2.2	6.3	5.4	5.3	2.5						
Sc^{43}	4.6	24.4	23.9	16.0	12.4	8.2	2.7	1.9		0.4	
Sc^{44}	10.3	49.1	47.1	36.3	25.9	13.4	6.4	2.9	1.6	0.7	0.4
Sc^{44m}	10.1	47.5	45.1	33.1	20.0	11.3	5.8	2.9	1.4	0.6	0.3
Sc^{46}	15.6	72.5	74.8	59.0	38.6	21.5	11.1	6.7	2.8	1.7	0.9
Sc^{47}	6.3	29.2	28.3	24.0	17.2	7.8	4.5	2.4	1.2	0.6	0.3
Cr^{48}	1.4	7.1	7.2	5.8	4.7	2.5	1.1	0.7			0.1
Sc^{48}	2.2	6.5	5.1	5.1	2.3	1.6	0.8				0.1
V^{48}	39.1	197.2	203.9	152.1	130.7	69.3	37.0	21.2	10.6	5.5	2.7
Cr^{49}	12.0	60.2	62.6	55.8	44.7	26.2	15.2	8.2	4.7	2.4	1.3
Cr^{51}	143.8	768.2	930.6	922.7	772.2	566.3	323.5	202.4	122.7	66.9	37.7
Fe^{52}	2.3	14.0	18.4	21.1	20.4	16.2	11.3	7.4	4.7	2.7	1.5
Fe^{53}	45.1	346.1	1148.4	982.1	1069.2	1100.9	562.3	792.0	240.8		
Mn^{52}	31.8	169.5	206.3	197.6	171.1	116.0	66.9	40.4	23.4	12.8	7.1
Mn^{54}	350.5	2106.7	3084.8	3682.8	3750.1	2970.0	2098.8	1338.5	855.4	502.9	291.9
Co^{55}	1.3	7.0	7.2	6.2	3.8	1.7		0.9			
Mn^{56}	41.6	166.3	252.7	305.7	322.7	281.2	203.5	136.6	79.6	53.1	32.3
Total	721.9	4103.4	6171.7	6523.7	6417.6	5237.1	3351.0	2565.3	1348.0	650.2	376.6

0.5-mm thick Fe plates (Figure 4.1). The measurements were performed using a 2-inch Ge(Li) detector with 20% relative efficiency. For the long-lived isotopes, the statistical accuracy was better than 3%. Table 4.3 shows all the identified isotopes for all 12 Fe plates.

Mn^{54} is the most active isotope, contributing $\sim$ 58% of the total activation near the shower maximum. This isotope is produced by bremsstrahlung photons via $Fe^{56}(\gamma, np)Mn^{54}$. Fe^{56} is 91.72% naturally abundant. The contribution from the $< 0.45\%$ trace Mn^{55} in the absorber to Mn^{54} is expected to be about 2.2% when scaled from $Fe^{54}(\gamma, n)\ Fe^{53}$. Mn^{54} has a 312-day half-life and emits 835 keV gammas. Alvarez *et al* quote 70 ± 4 mb for maximum cross section at $E_{max} = 17.4$ MeV [27].

The second highest contributor to the total activation is Fe^{53} via the $Fe^{54}(\gamma, n)Fe^{53}$ reaction. Fe^{54} is 5.8% naturally abundant. The gamma energy threshold for this reaction is 13.8±0.2 MeV [28]. As the photon energy increases, the cross section sharply increases to a maximum ($\sigma_m \approx 67$ mbarn) and falls again. The strong dependence of the cross section for gamma energies around $E_m = 18.7$ MeV selects photons in this energy range with full-width half maximum, $\Gamma = 6.3$ MeV. Norbury *et al.* studied the same reaction later and quote similar values [29]. The shape of the curve (dotted histogram) in figure 4.6 reflects the distribution of photons predominantly in this energy range as a function of absorber depth. The dotted line is the same curve as shown in figure 4.3 but normalized to at the shower maximum.

When compared with the longitudinal shower shape in figure 4.3, the exponential fall after the shower maximum is in this case slower, indicating that on average, the photons of this energy tend to range over the entire absorber and carry a larger fraction of the shower energy deeper into the absorber compared to electrons. When these β values are compared with the photon mass attenuation lengths, λ_a, there is good agreement. For 2 MeV photons (see figure 4.7), the Particle Data Group [21] gives $\lambda_a^{Fe} = 0.33$ cm^{-1} and we measure the same value for β's as shown in Table 4.4.

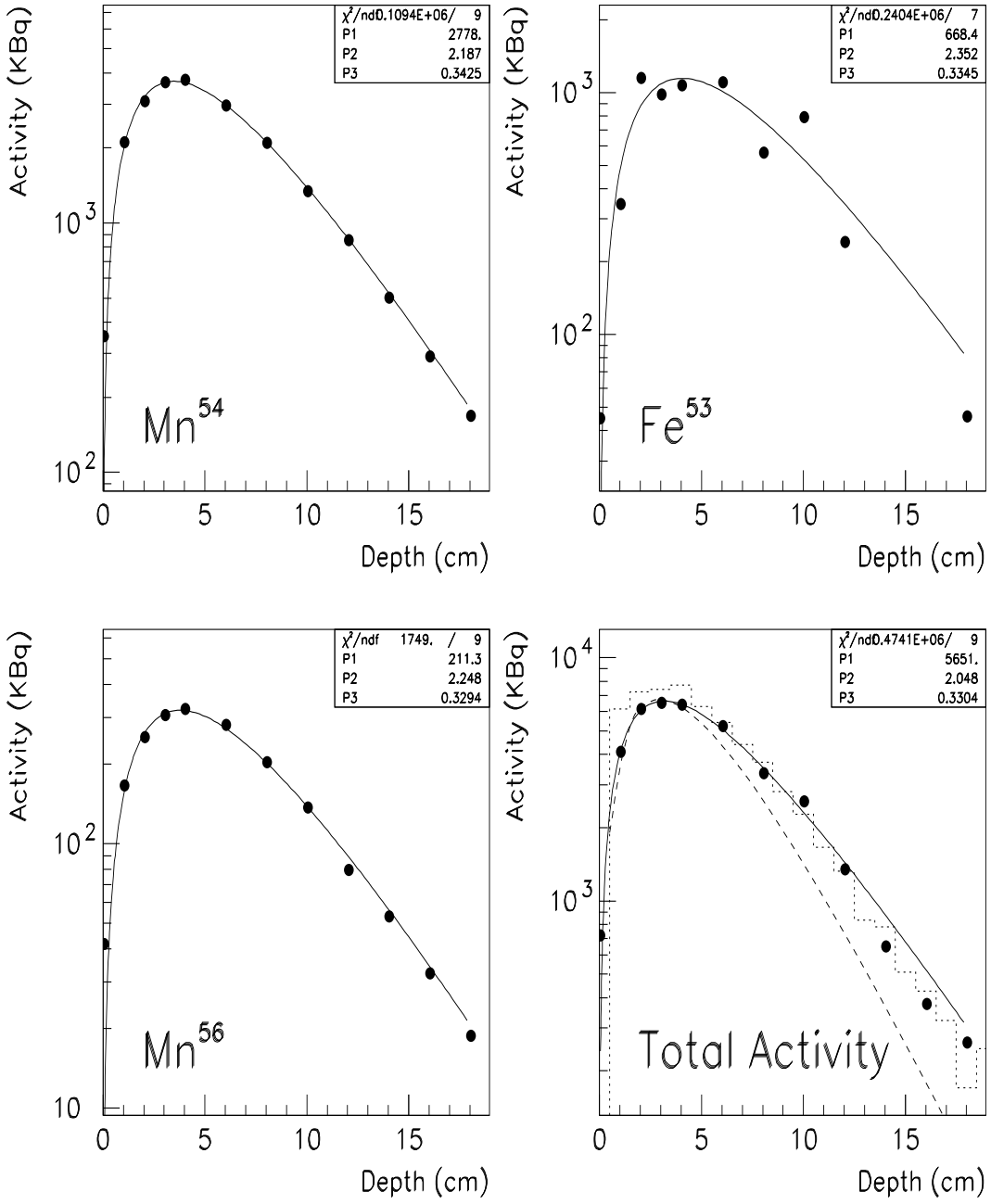

Figure 4.6: Mn^{54}, Fe^{53}, Mn^{56} and the total activation profiles as a function of the absorber depth are shown above in kBq and the fit parameters are discussed in the text.

The spectrum of the photons in the shower changes slowly with the depth of the absorber. While the mean photon energy goes from above 10 MeV to one MeV in 20 cm of iron, the fluctuations around these mean values are large, as *EGS4* results show in Figure 4.7. The development of the shower is a matter of balance and fluctuation between the absorbtion of low energy particles and their creation with more energetic secondaries.

Table 4.4: The fit parameters for Mn^{54}, Fe^{53}, Mn^{56} and the total activation curve shown in figure 4.6.

Isotope	k	α	β [cm^{-1}]	z_{max} [cm]
Mn^{54}	2778	2.19	0.34	3.5
Fe^{53}	668	2.35	0.33	4.1
Mn^{56}	211	2.25	0.33	3.8
Total	5651	2.05	0.33	3.2

The photo-production of neutrons and protons on complex nuclei strongly depends on energy. At low γ energies ($\sim 10-20$ MeV), the photons are absorbed via dipole (giant resonance) interactions and $(\gamma, n), (\gamma, 2n)$, (γ, np), (γ, p), *etc.* reactions ensue. These resonance reactions were first predicted by Goldhaber and Teller [30] and by Levinger and Bethe [31]. Cross sections for about twenty elements were studied experimentally in the early 1950's [28, 32, 33]. Two generalities emerge in (γ, n) reactions; the maximum cross section σ_m goes like $A^{5/3}$ where A is the atomic mass and the measured full width half maximum (FWHM), Γ, is about 6 MeV for $A > 30$. At higher energies, the cross section decreases quickly because only a part of the nucleus interacts with shorter wavelength photons. A common product at these energies is np, photo-disintegration of quasi-deuteron, as in the case of $Fe^{56}(\gamma, np)Mn^{54}$. For energies above 50 MeV, the

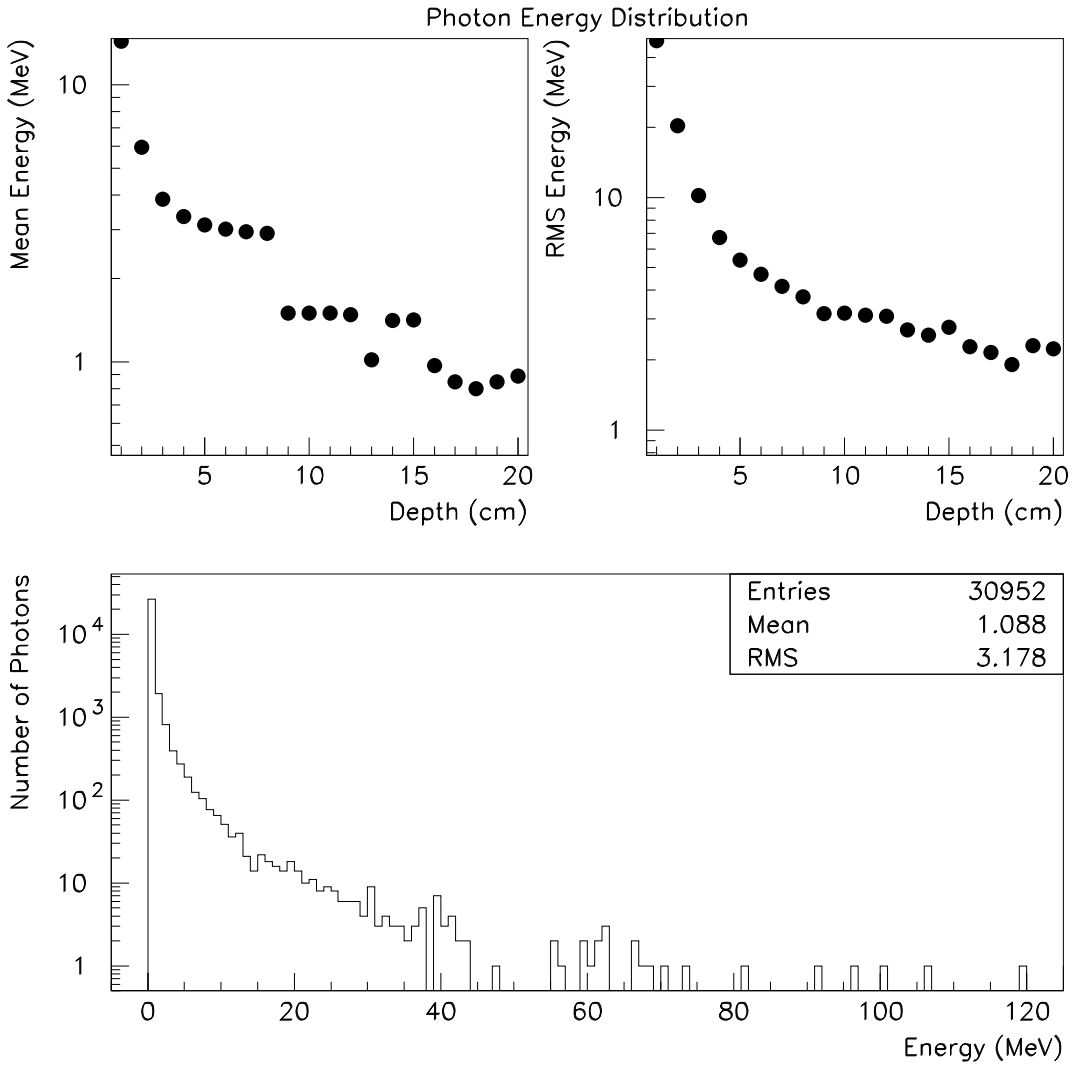

Figure 4.7: The *EGS4* simulation for the mean and rms-values of photons in an iron absorber shows a slowly changing energy spectrum as a function of depth for 500 MeV incident electrons. The rms values of the photon energy distributions remain relatively large. In the bottom plot, the photon energies are histogrammed between $10 - 11$ cm depth of iron.

cross section can be scaled from the known deuteron photo-disintegration cross section, σ_d, in the following form,

$$\sigma(\gamma, np) = L\frac{NZ}{A}\sigma_d \tag{4.4}$$

where N and Z are the neutron and proton numbers and A is the atomic mass. Although $6 \leq L \leq 8$ from theoretical arguments, the experiments suggest $L \approx 3$ [34, 35]. The cross section, σ_d peaks at 4.4 MeV and decreases rapidly, ($\propto 1/E_\gamma, E_\gamma \leq 125$ MeV), only to rise again at 300 MeV to a less than a tenth of its value at 4.4 MeV. When evaluated at 20 MeV, for example, $\sigma(\gamma, np) \approx 20$ mbarn if $L = 3$ for iron.

The lateral activation profile from the Fe-II block is shown in Figure 4.8. For this particular study only, the Fe-II block was subjected to 8.5×10^{12} electrons in 20 seconds and beta activity was measured soon after the termination of irradiation (t_0) and thirty minutes later in order to identify dominant radioisotopes. Note that at every two centimeters from the shower axis the total activity is down approximately by an order of magnitude. When the nature of activity is further analyzed, the major radioisotopes turn out to be Mn^{56} and Fe^{53} with half-lives of 2.58 hours and 8.51 minutes, respectively. The Fe^{53} curve, due to $Fe^{54}(\gamma, n)Fe^{53}$, indicates the distribution of energetic photons as already elaborated above. They tend to penetrate further and spread out from the axis of the cascade. Mn^{56} is mainly due to $Fe^{56}(n, p)Mn^{56}$ for which the cross section peaks at $E_n = 14$ MeV to 120 mb. The difference between the Fe^{53} and Mn^{56} curves clearly illustrates the energetic photon and neutron distributions in an electromagnetic shower. Activation due to neutrons seems constrained in the upstream end of the absorber and activation due to photonuclear reactions tends to be deeper and broader in the absorber.

4.5 Results and Discussions

The CMS forward calorimeter will experience integrated doses up to a $GRad$ or more at the highest rapidities. The activation of the iron absorber will reach $\sim 60MBq$,

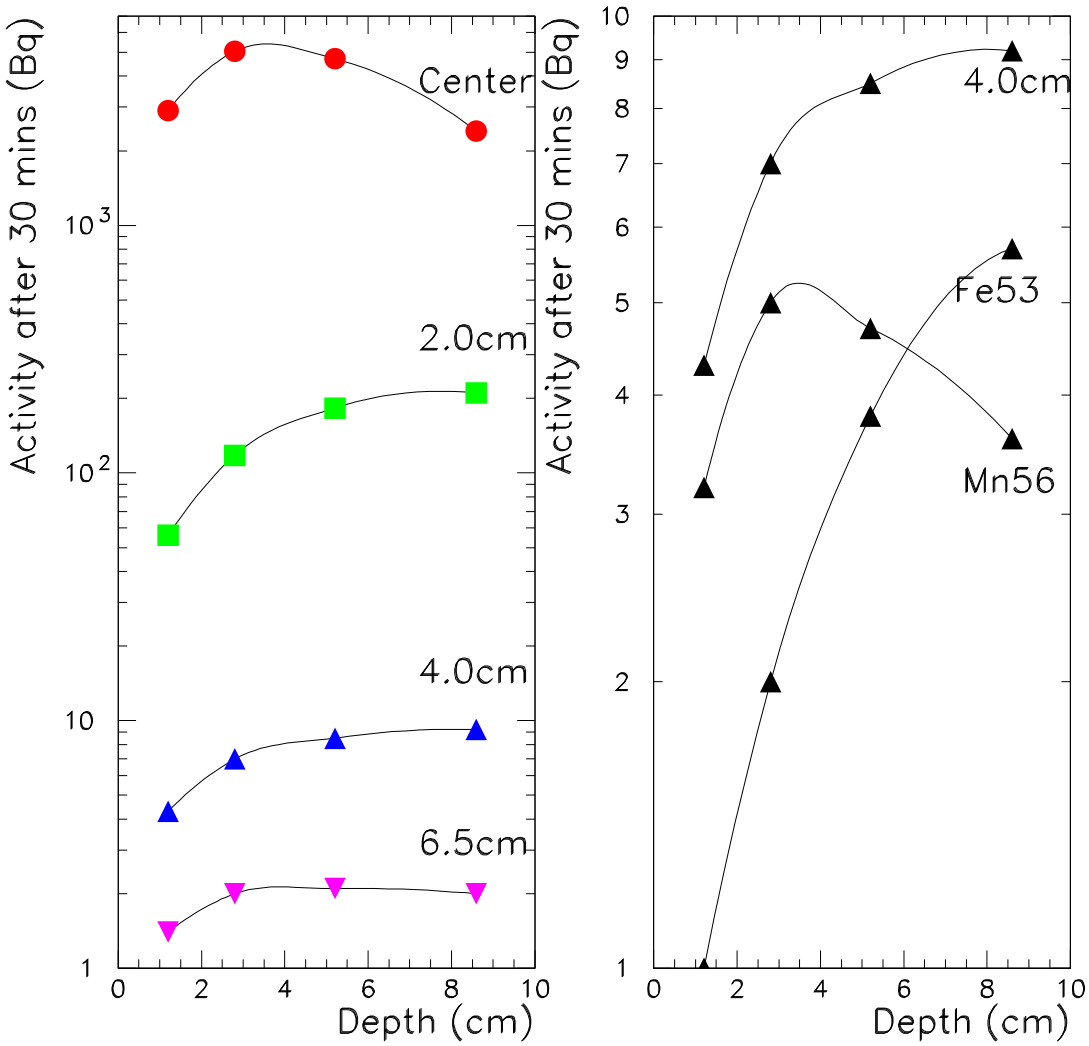

Figure 4.8: The total lateral activation profiles for beta emission as a function of off-axis distance are shown on the left plot. The nature of the activity at 4 cm from the shower axis is further shown on the right figure where the uncertainty is estimated to be ±15%.

if we use a simple conversion of $6Bq/Gray$ without being concerned with the short half-life isotopes and activation/deactivation cycles during runs and assuming that all of the dose is due to photonuclear reactions. This clearly would be an underestimate.

The *EGS4* simulation reproduces dose measurements fairly well for all depths. The agreement is within 20% at the shower maximum.

A simple parametrization as in Eq.(4.1) is a reasonable one when an average behavior of the shower is desired, but it is a poor one if precise information is sought at and around the shower maximum.

The lateral shower profile data are well reproduced by the simulation essentially at all depths.

CHAPTER 5
FORWARD CALORIMETER PRE-PRODUCTION-PROTOTYPE I (PPP-I) DESIGN AND TEST BEAM RESULTS

The HF calorimeters are cylindrically symmetric around the beam line and on each side of the CMS detector. The length of each is 1.65 m. This length is enough to contain the Čerenkov signal produced by hadrons up to 1 TeV. The HF has two longitudinal segments to optimize the energy resolution. The segmentation is achieved by two different fiber lengths; EM (1.65 m long) and HAD (1.43 m long). The Quartz Fibers will be embedded in steel blocks.

5.1 Pre-Production-Prototype (PPP-I)

The PPP-I is an iron absorber matrix with embedded quartz fibers of 300 μm core diameter which serve as the active material. The iron matrix is composed of 2.5 mm thick iron layers with grooves every 2.5 mm. The length of the absorber is 165 cm ($8.3\lambda_{int}$) with a cross sectional area of 18 cm x 18 cm. A single quartz fiber is inserted in each groove. A total number of 6000 fibers are then grouped into 27 bundles. In PPP-I, there are three different lengths of fibers to achieve a longitudinal segmentation. They are called electromagnetic (EM), 93.75 X_0, hadronic (HAD), 81.25 X_0, and tail catcher (TC), 17.05 X_0. Long fibers sample all shower components while the shorter fibers are biased to the hadron component. The physical spacing between fibers is the 2.5 mm groove spacing. The pattern used for the fiber insertion is shown in figure 5.1. There are two EM fibers for each HAD and TC fiber. PPP-I is divided into nine physical regions called towers, each with a 6 cm $\times$ 6 cm cross sectional area (see figure 5.1). At the center of each tower, a radioactive wire source-tube groove exists for calibration. Each fiber bundle (EM, HAD and TC) from a tower is coupled to a separate photomultiplier tube (PMT) via a light-guide and read out as a separate ADC channel. The performance of PPP-I was tested during a beam test in September 1999. The results are summarized

in the following sections.

5.2 Spatial Uniformity of PPP-I

In order to study the spatial uniformity of the PPP-I, a 120 GeV electron beam was moved with 1.0 cm steps across the face of the detector, and the signals of three adjacent towers (towers 4, 5 and 6. See figure 5.1.) were plotted as a function of the beam position. The beam spot size was $\sim$2 cm $\times$ $\sim$2 cm. With the help of drift chambers located upstream, the impact position of every single particle of the beam on the detector face was known with a precision of 200 μm.

Results of the beam scan are summarized in figures 5.2 and 5.3. As mentioned earlier, quartz fibers are embedded in the iron matrix as shown in figure 5.1. There are two EM fibers for each HAD and TC fiber giving rise to a 5 mm spacing between two EM fibers. This fiber periodicity can be seen in the beam scan data. The exact EM fiber locations are visible in figure 5.2 which plots only the response of the EM fibers. The area between (64 mm$\leq y \leq$66 mm) and (54 mm$\leq x \leq$60 mm) in this figure corresponds to a source-tube groove that does not have a quartz fiber so as to allow the insertion of a radioactive wire source for calibration purposes.

Figure 5.3 shows the x-projection of the two dimensional plot shown in figure 5.2 for two consecutive fiber layers. There is a $\pm$6% fluctuation in the response of the detector due to the fiber periodicity. This is the result of the fact that the response of the calorimeter is slightly higher for particles entering the calorimeter in the fiber plane than for those entering in the absorber plane.

In figure 5.4, the response of the detector is shown for three adjacent towers (4, 5, and 6) as open triangles, squares and circles respectively. As the beam moves from one tower to another, the measured signal amplitudes for adjacent towers change. A sharp tower to tower transition is seen due to the narrow lateral profile of Čerenkov light generating particles. The sum of the signals of three towers is also shown in the same

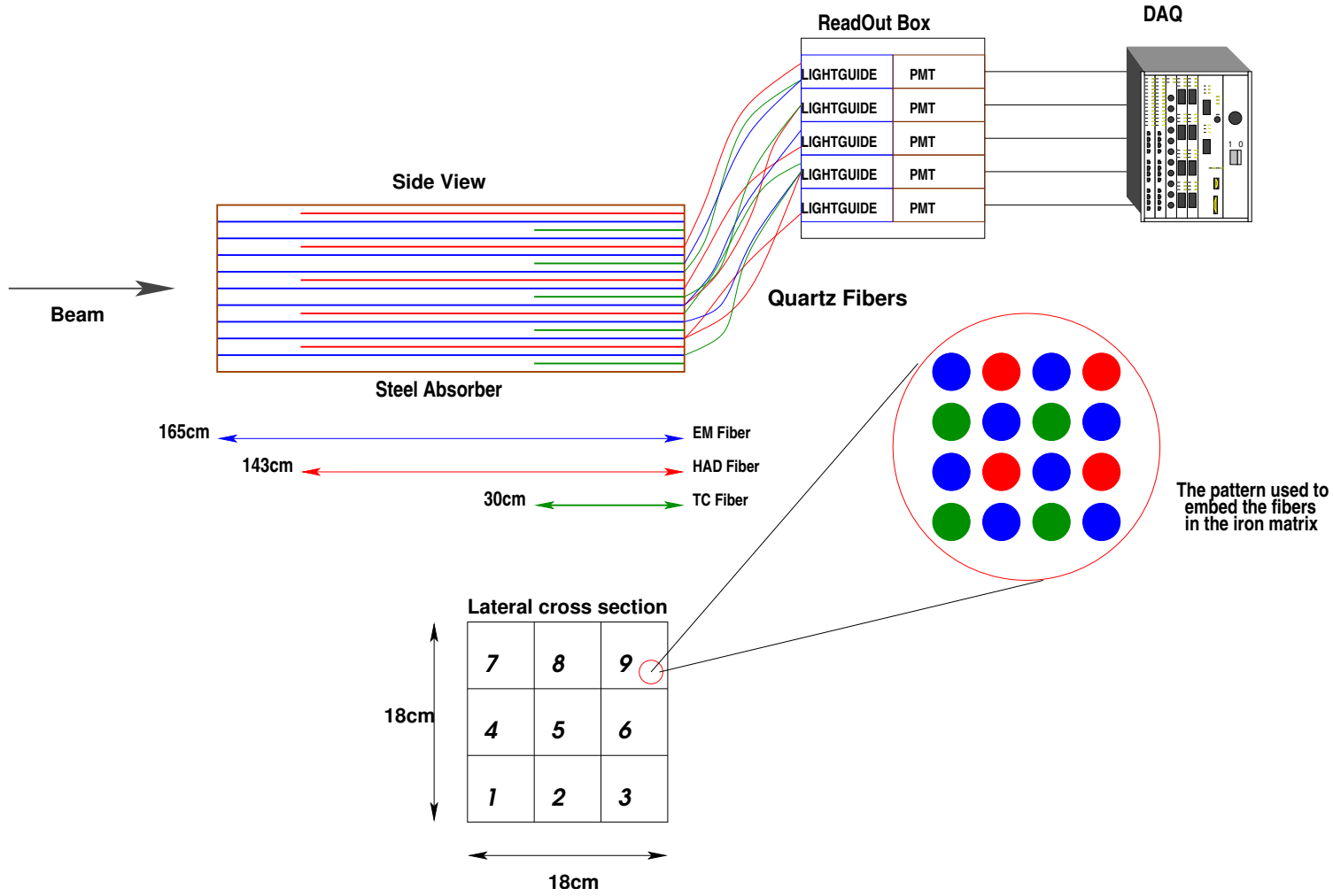

Figure 5.1: Schematic view of PPP-I.

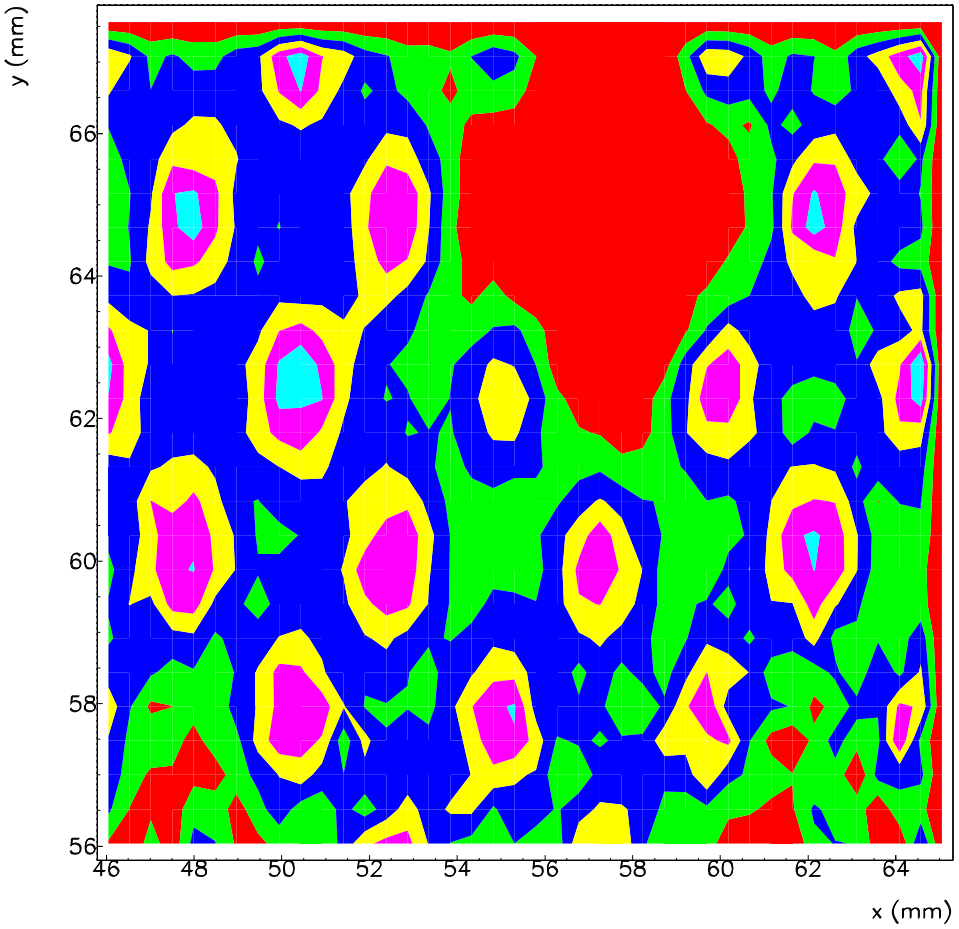

Figure 5.2: EM fiber locations revealed with 120 GeV electrons. The source tube location is also visible.

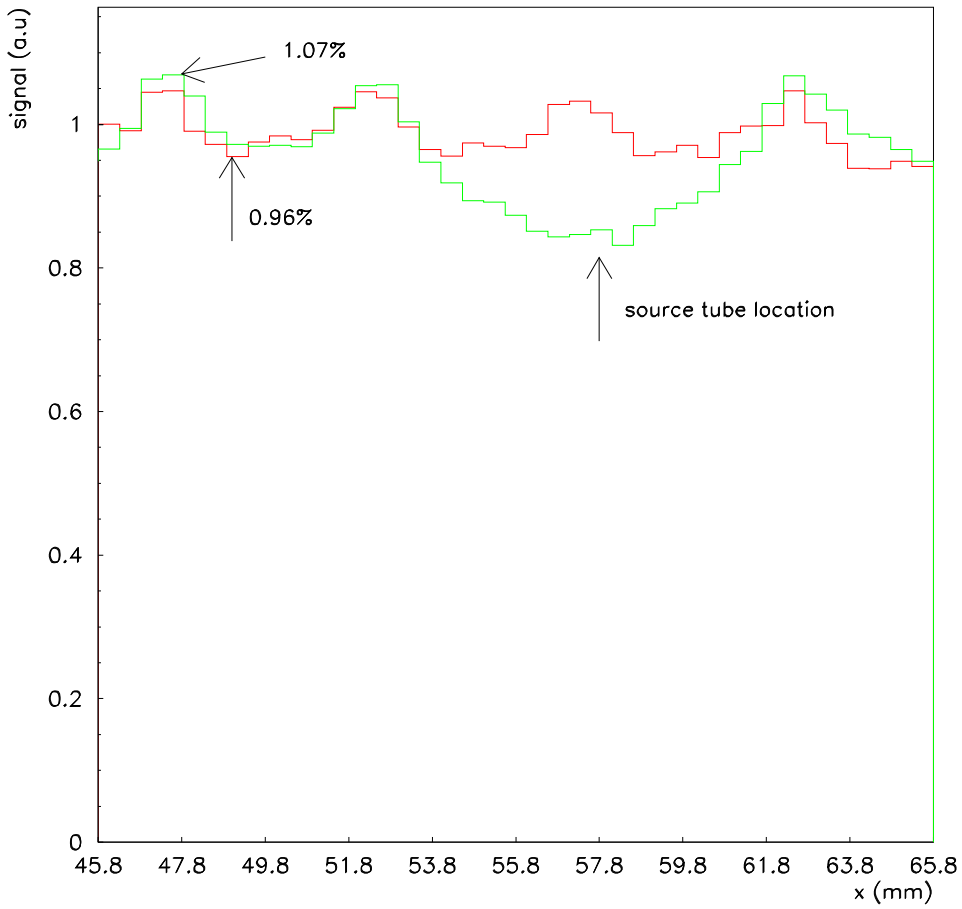

Figure 5.3: Overlayed x-projections of figure 5.2 at $y = 60$ mm and $y = 65$ mm

figure as stars with connected line.

A similar beam scan was also carried out with a 120 GeV π^- beam. The π^- beam was moved vertically across the face of the PPP-I. The signal amplitudes are shown in figure 5.5. Since the hadronic showers are not as narrow as electromagnetic ones, tower to tower transition profiles are not as sharp as in the electromagnetic case due to the larger tails. Therefore the contribution of the adjacent towers to the total signal at a given tower position is higher compared to the electromagnetic case giving rise to a larger total signal.

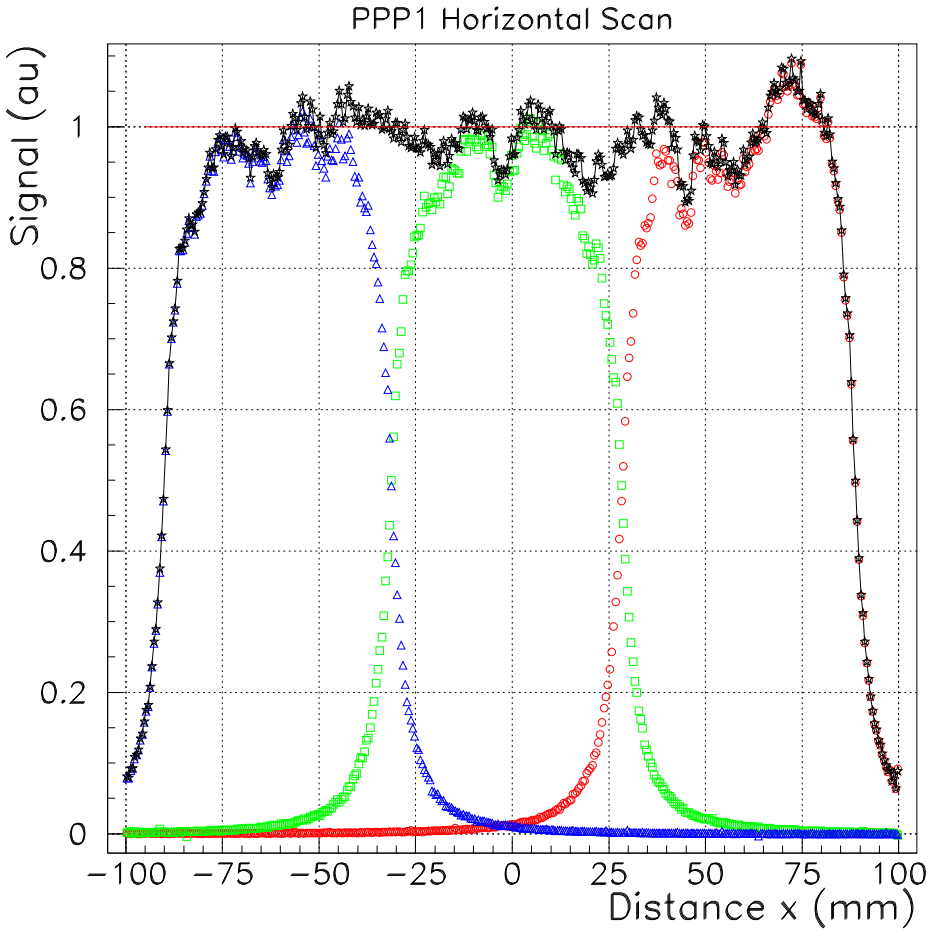

Figure 5.4: Horizontal scan along towers 4, 5, 6 (open triangles, squares and circles, respectively) with 120 GeV electrons and the sum of the signals of the three towers (stars connected with line)

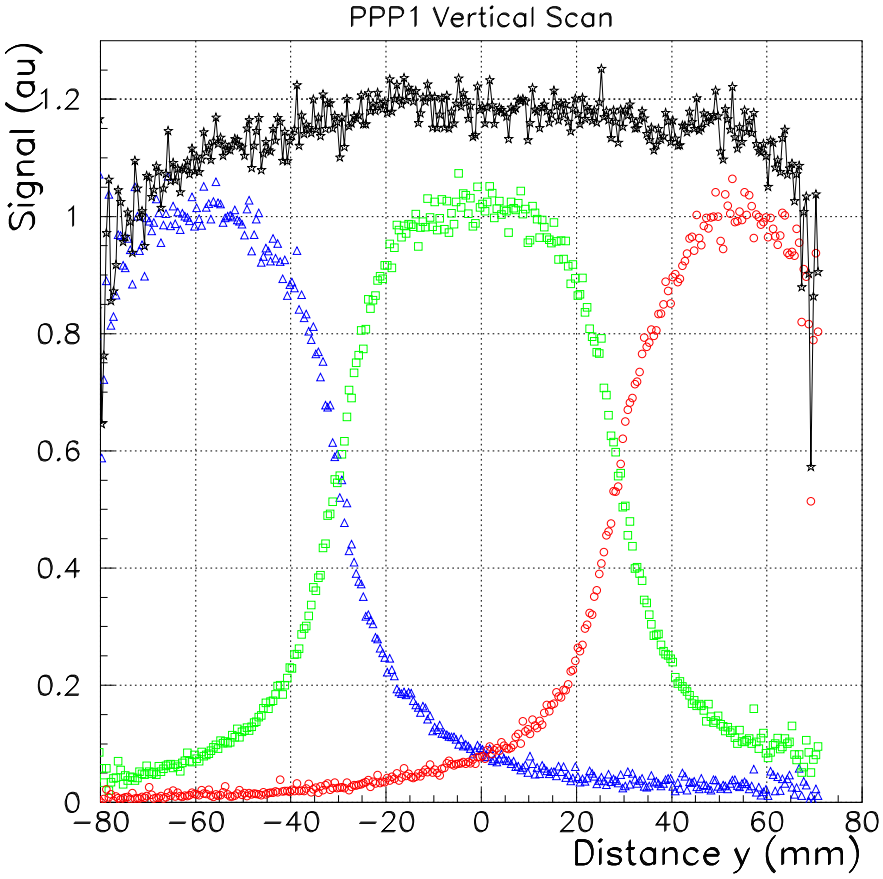

Figure 5.5: Vertical scan along towers 2, 5, 8 (open triangles, squares and circles, respectively) with 120 GeV pions and the sum of the signals of the three towers (stars connected with line)

5.3 PPP-I Energy Resolution

The energy resolution of a calorimeter, in general, can be parametrized as

$$(\frac{\sigma}{E})^2 = (\frac{a}{\sqrt{E}})^2 + (\frac{b}{E}) + c^2 \tag{5.1}$$

The first term is the sampling term and characterizes the statistical fluctuations in the signal generating processes. The second term corresponds to noise and includes the energy equivalent of electronic noise as well as pileup. The third term is the constant

term and is related to the imperfections of the calorimetry, signal generation and collection non-uniformity, calibration errors and fluctuations in the energy leakage from the calorimeter.

The energy resolution of PPP-I was studied in response to both electron and pion beams at different energies. The beam energies and the particle type used are summarized in Table 5.1.

Table 5.1: Beam type and energies used for energy resolution study

Beam	Energy (GeV/c^2)
e^-	6, 8, 15, 20, 35, 50, 80, 100, 120, 150, 200
π^-	12, 15, 20, 35, 50, 80, 100, 120, 150, 175, 200, 225, 250, 275, 300, 350, 375

It had been shown in one of our earlier prototype tests [40] that in a quartz fiber calorimeter the electromagnetic energy resolution is completely dominated by photoelectron fluctuations. Therefore when we characterize our electromagnetic energy resolution we will drop the noise term as

$$(\frac{\sigma}{E})^2 = (\frac{a}{\sqrt{E}})^2 + c^2. \tag{5.2}$$

The response of the PPP-I has been recorded as a function of beam energy. As an example of the typical response of the detector to electron and pion beams, the signals recorded for a 100 GeV electron beam and a 225 GeV π^- beam are shown in figures 5.6 and 5.7. The response of the calorimeter to electrons is seen to be Gaussian. However a deviation from Gaussian behavior is seen in the response to the π^- beam. This is a result of the different natures of electromagnetic and hadronic showers [39].

Of the secondary hadronic particles, mostly π^0s contribute to the Čerenkov signal since they decay into two photons which in turn contribute to the electromagnetic core and register in the detector as Čerenkov light. Other non-electromagnetic secondaries

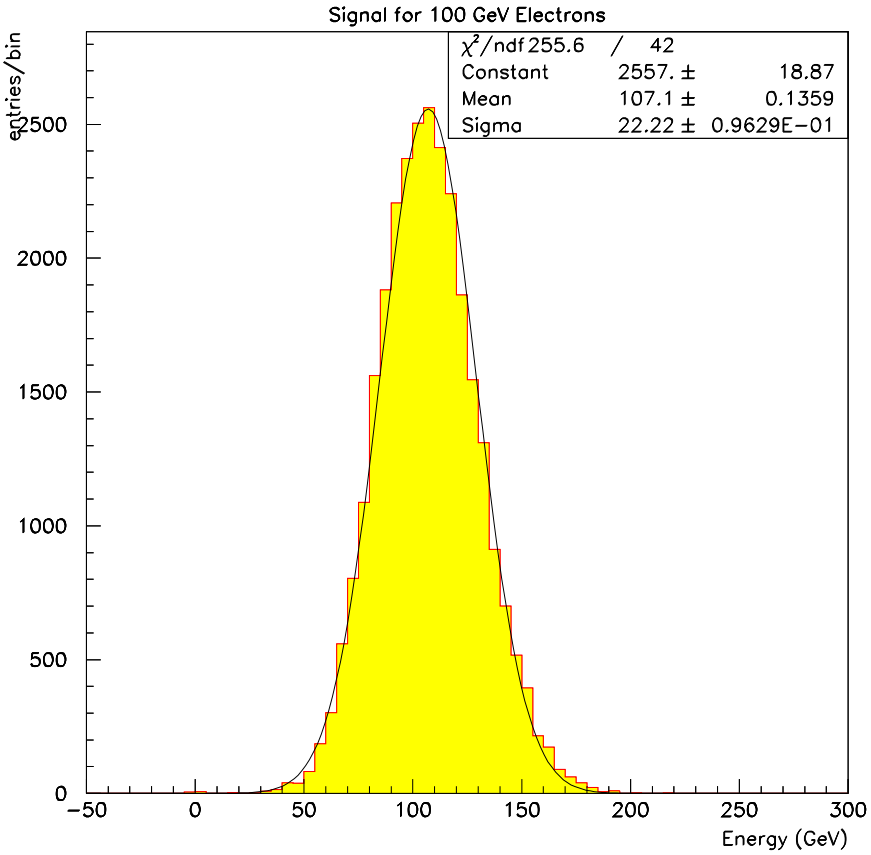

Figure 5.6: PPP-I response to 100 GeV e^-s

are mostly not relativistic and therefore do not give rise to Čerenkov light and hence do not register in the detector. At low energies, the number of π^0s in the shower is characterized by a Poisson distribution which becomes more and more Gaussian at high energies.

Figure 5.8 shows the energy resolution for electrons as a function of energy. The resolution (σ/E) is plotted against $1/\sqrt{E}$ and fitted to equation 5.2. The fit yields

$$(\frac{\sigma}{E})^2 = (\frac{197\%}{\sqrt{E}})^2 + (8\%)^2.$$

The Hadronic energy resolution of PPP-I as a function of energy is shown in figure 5.9. At 1 TeV, the energy resolution is 20%.

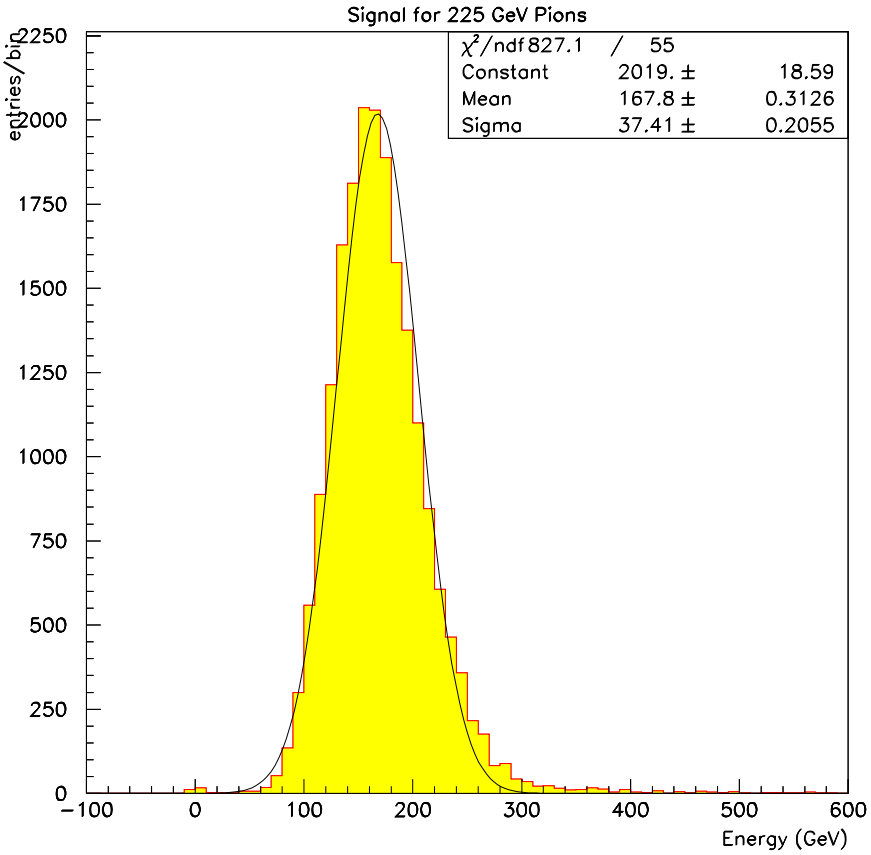

Figure 5.7: PPP-I response to 225 GeV π^-s

5.4 Energy Response Linearity

PPP-I exhibits a different response to electromagnetic and hadronic showers. The data sample shown in Table 5.1 is used in this study. The response of the PPP-I was recorded as a function of beam energy. The measured response, then, was normalized by dividing by the beam energy and then plotted against the beam energy (See figures 5.10 and 5.11).

The response as a function of electron beam energy is linear to within 1%. However, as seen in figure 5.11, the response is very non-linear for different energies of hadronic beams. This is due to the electromagnetic portion of the hadronic shower, that is, the π^0

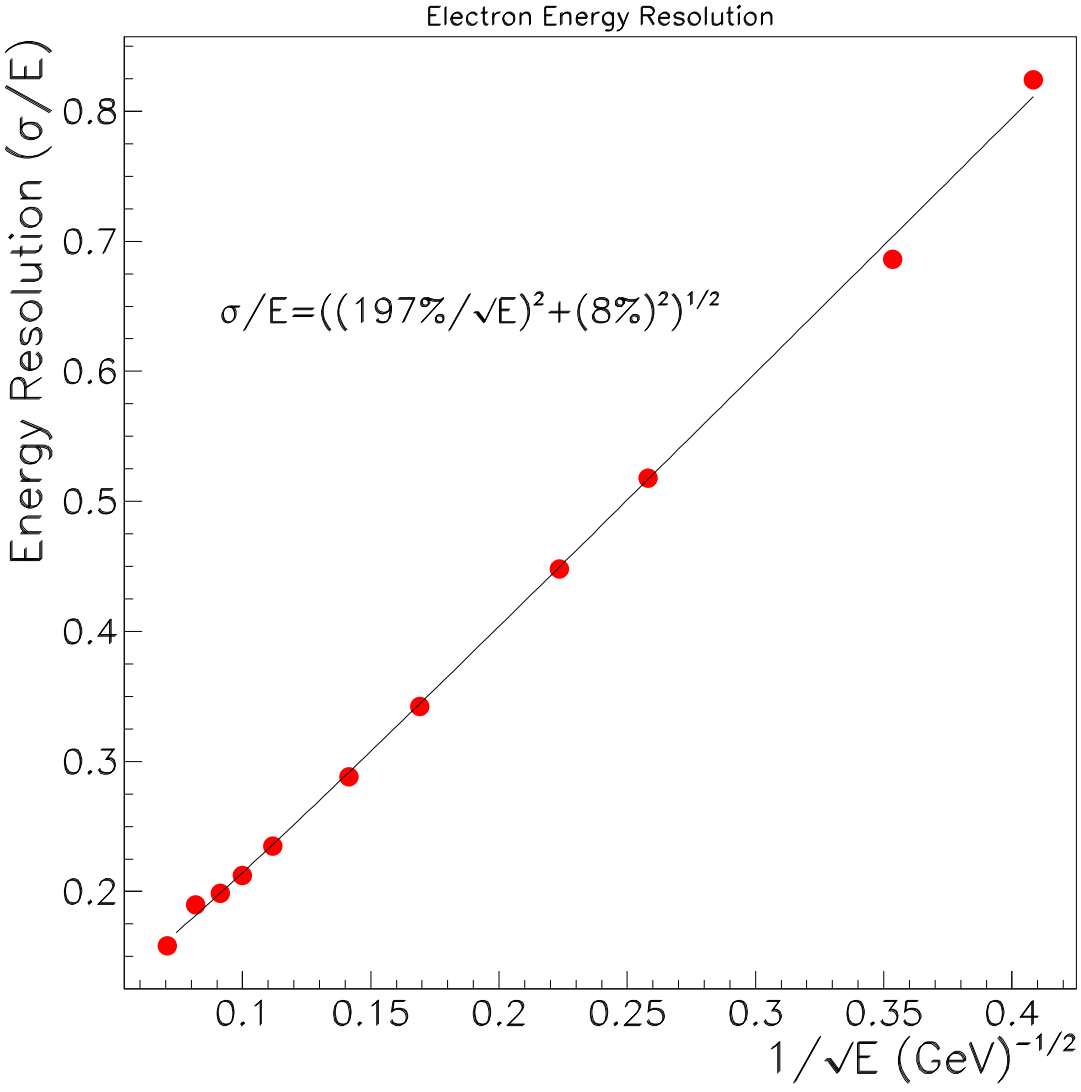

Figure 5.8: Electromagnetic energy resolution as a function of $1/\sqrt{E}$

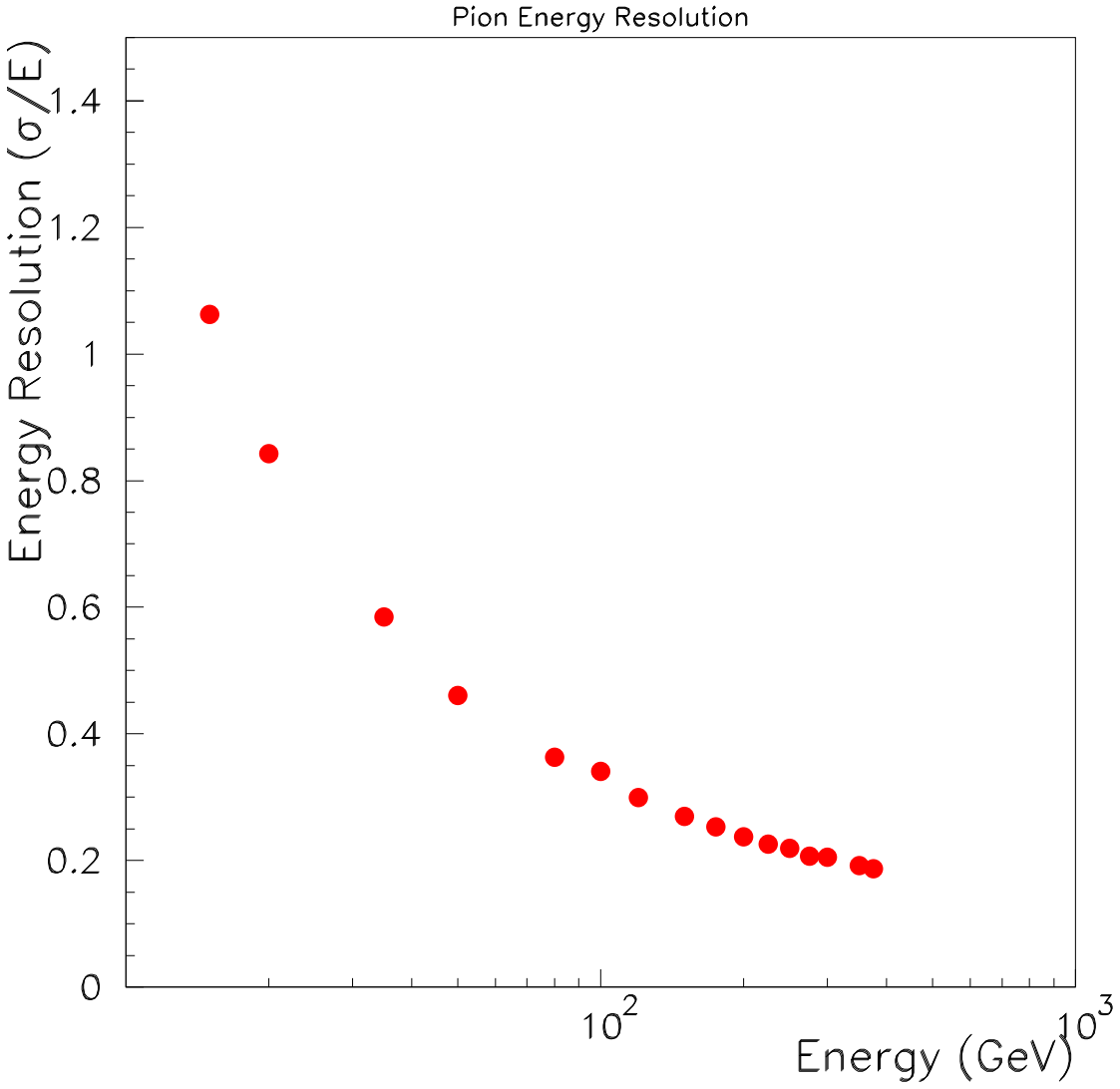

Figure 5.9: Hadronic energy resolution as a function of π^- beam energy

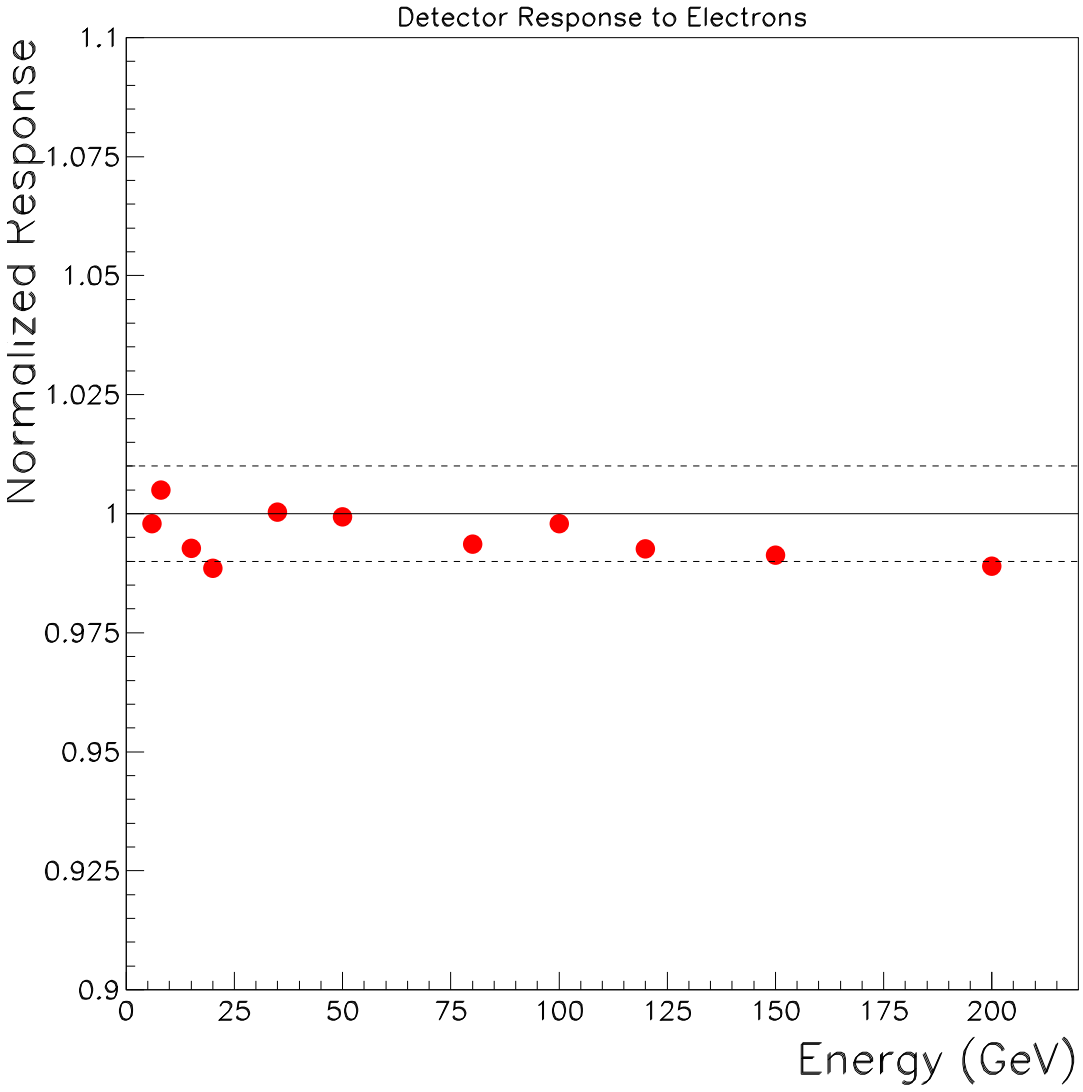

Figure 5.10: Normalized response to e^-s as a function of beam energy

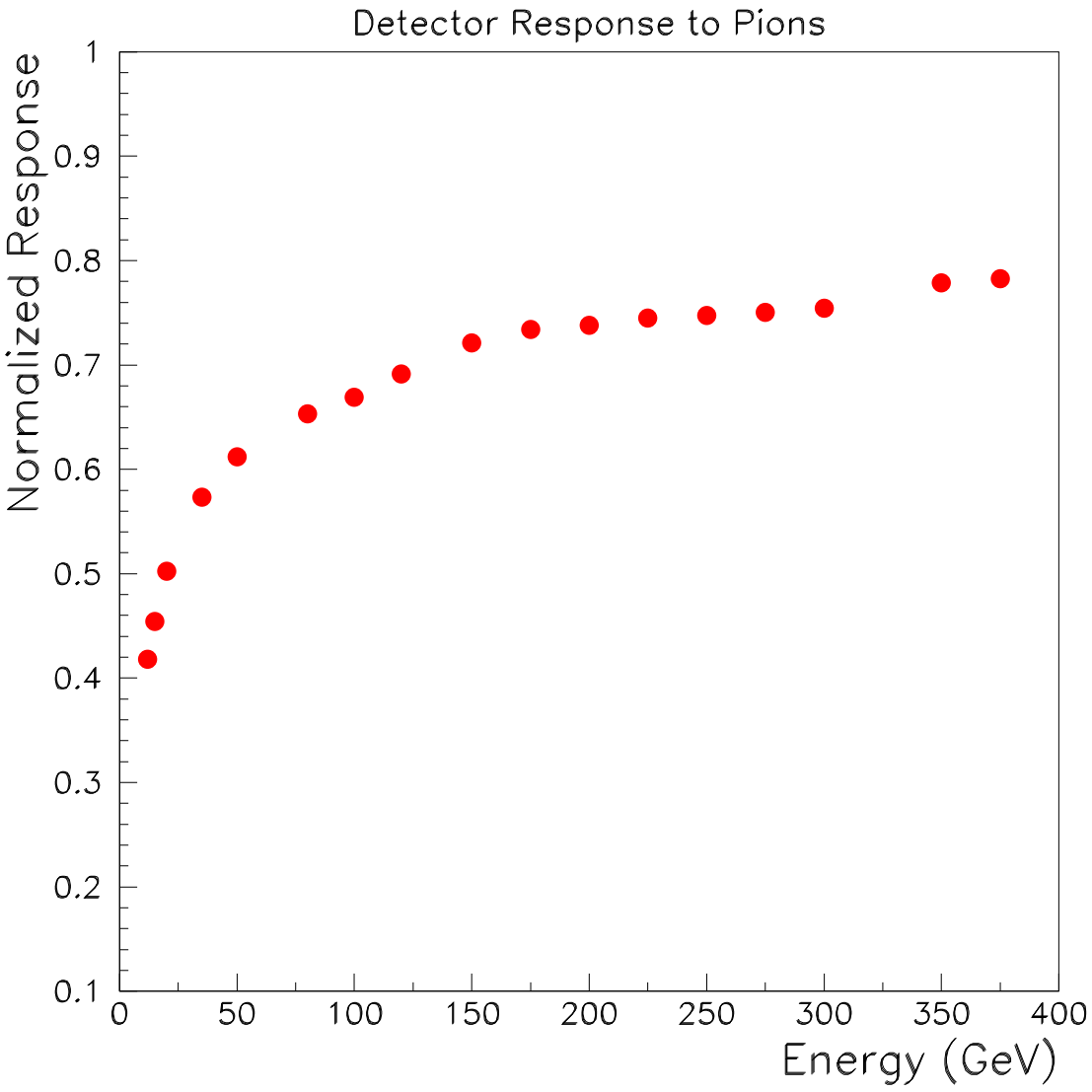

Figure 5.11: Normalized response to π^-s as a function of beam energy

content. As the beam energy increases, the π^0 fraction increases giving rise to a larger Čerenkov signal in the detector.

5.5 Longitudinal Hadronic Shower Profile

The hadronic shower is the result of a series of inelastic hadronic interactions of incoming hadrons with the absorber nuclei. The length scale of this cascade process is characterized by nuclear interaction length, λ_{int}, [41]

$$\lambda_{int} \approx 35\ g\ cm^{-2} A^{1/3} \tag{5.3}$$

The shower maximum, t_{max}, occurs, in units of λ_{int}, at

$$t_{max} \approx 0.2\ lnE(GeV) + 0.7 \tag{5.4}$$

95% energy containment is achived at a depth of

$$L_{0.95}(\lambda_{int}) \approx t_{max} + 2E^{0.13}(GeV) \tag{5.5}$$

PPP-I is sensitive only to Čerenkov light and the Čerenkov signal containment is achieved at a shorter depth than in ionization detectors. This is due to the production characteristics of Čerenkov light which is mainly by electrons and positrons, but not neutrons, heavily ionizing particles or nuclear breakup.

Longitudinal shower development profiles of PPP-I were studied with π^- particles at energies of 100 and 375 GeV. Iron bricks with thicknesses of 5 cm and 10 cm were stacked in front of the detector and the detector response recorded. The results are tabulated in Table 5.2. In order to calculate the signal at a particular depth, the difference of the signal averages from two consecutive thicknesses of iron corresponding to this depth is taken. The longitudinal shower profiles are shown in Fig. 5.12. A depth of ~ 135 cm ($8\lambda_{int}$) is sufficient to contain 95% of the Čerenkov signal.

5.6 Summary and Conclusions

A Pre-Production-Prototype for the forward calorimeter of the CMS detector has been tested at the H4 beam line at CERN. The electromagnetic energy resolution was

Table 5.2: Longitudinal shower profile measurements of the amplitude of the Čerenkov light signal

Fe Block (cm) [λ_{int}]	100 GeV π^- (a.u.)	375 GeV π^- (a.u.)
5 [0.29]	358	1603
15 [0.89]	337	1551
25 [1.49]	276	1338
35 [2.09]	212	1032
45 [2.69]	155	771
55 [3.29]	109	586
65 [3.89]	77	437
75 [4.49]	57	311
85 [5.09]	41	222
95 [3.89]	27	164
105 [6.29]	19	118
115 [6.89]	13	87
125 [7.49]	9	65
135 [8.08]	8	45
145 [8.68]	7	34
155 [9.28]	5	26

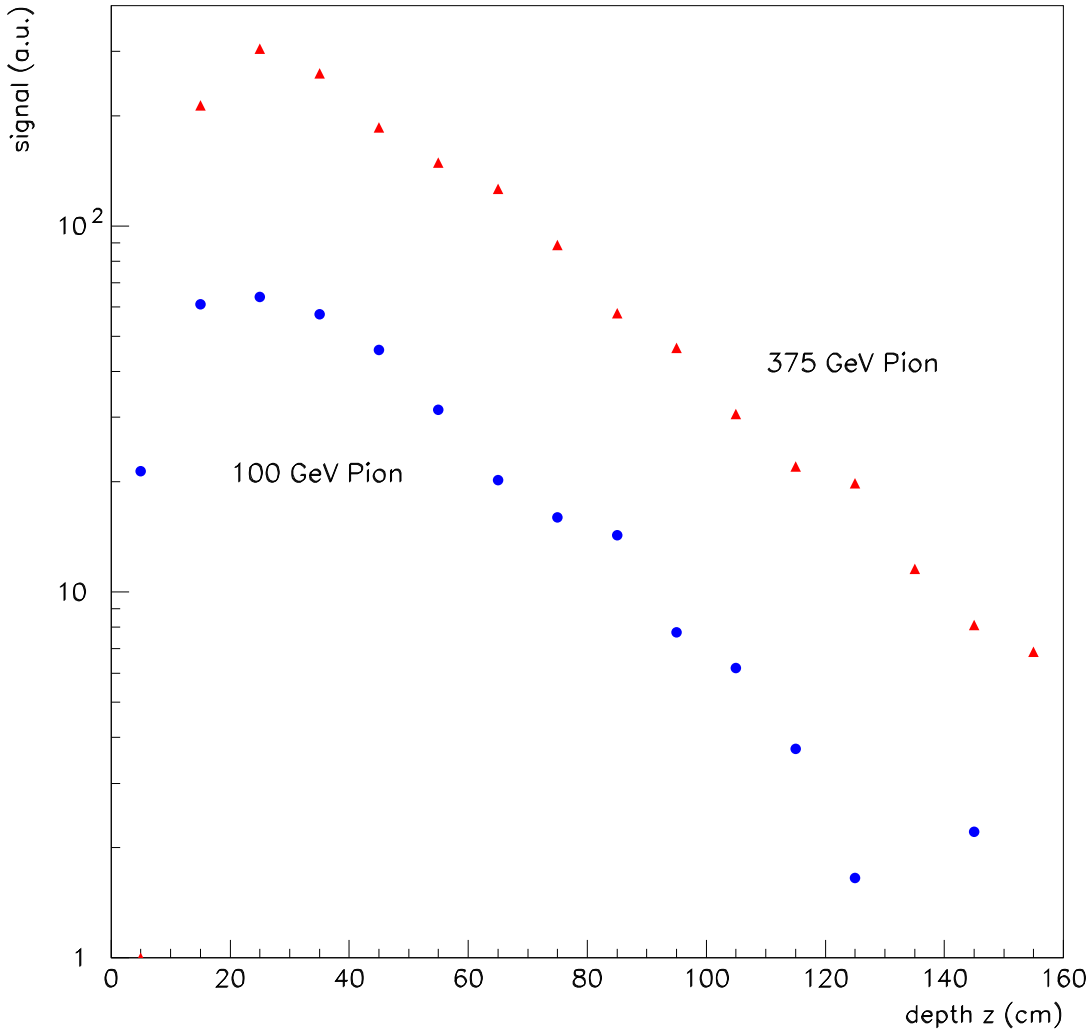

Figure 5.12: Longitudinal shower profiles of 100 GeV and 375 GeV π^- beam in PPP-I

measured to be $(\frac{\sigma}{E})^2 = (\frac{197\%}{\sqrt{E}})^2 + (8\%)^2$. The hadronic energy resolution was determined to be 20% at 1 TeV. The response was found to be linear to 1% for electrons. A highly non-linear behavior for hadrons was observed. More than 97% of the shower signal was contained by the PPP-I ($9.8\lambda_{int}$).

CHAPTER 6
Ω_C^0 SEARCH AT E781 (SELEX) EXPERIMENT

6.1 Introduction and Motivation

E781(SELEX) [42] is a fixed target experiment which took data during the years 1996-1997. The SELEX (SEgmented LargE-X spectrometer) is a multistage spectrometer for large acceptance of Feynman X-parameter, $x_F = 2P_{\parallel}^{cm}/\sqrt{s} > 0.1$ where $P_{\parallel}^{cm}$ is the momentum component of the particle under consideration along the beam particle's direction and s is the center of mass energy, to study high energy hadroproduction. It used both negative beam ($50\%\Sigma^-, 50\%\pi^-$) with 600 GeV/c momentum and positive ($92\%p, 8\%\pi^+$) beam with a 540 GeV/c momentum. During approximately two years of running, E781 recorded 15.2 billion hadronic interaction events. The physics goals of the SELEX experiment can be summarized as the study of the lifetime of weakly decaying charmed baryons, the study of the charmed baryon production, the excited charm baryon studies and the charm baryon semileptonic decay studies.

6.2 Ω_c^0 Charmed Baryon: Theoretical Background

Ω_c^0 is a doubly-strange charmed baryon. Its quark content is (ssc), and its existence was predicted within the framework of the quark model. The first experimental evidence was reported in 1985 by the WA62 experiment at CERN [43]. In the Particle Data Group (PDG) [44], the mass is given as 2697.5±2.6 MeV, and the lifetime τ is given as 64±20 fs.

6.2.1 Theoretical Background

Baryons are classified according to the irreducible representations of the $SU(N)$ group where N is the number of quarks. If the $SU(N)$ symmetry were exact, one would

expect that all members of the multiplets have the same mass. The $SU(4)$ symmetry is broken by the charm mass, however it describes the baryon families well. $SU(4)$ 20-plets are baryons consisting of up, down, strange, and charm quarks. The multiplets with spin $J = 1/2$ and $J = 3/2$ are shown in figures 6.1 and 6.2. In these multiplets,

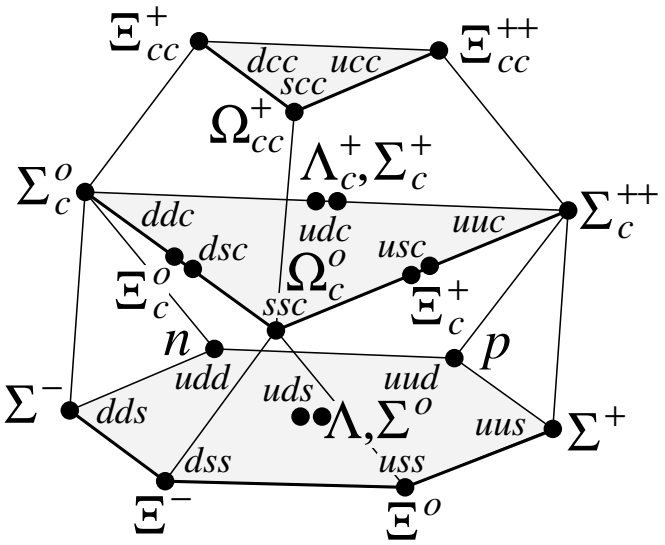

Figure 6.1: $SU(4)$ 20-plet baryon family with $J^P = (1/2)^+$

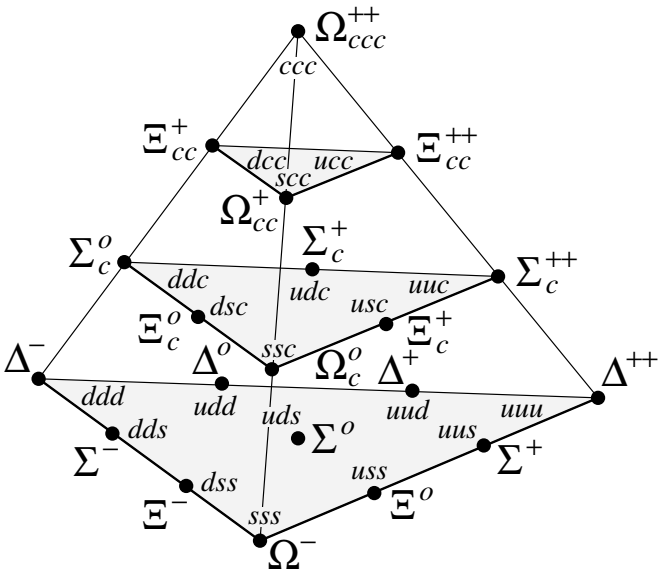

Figure 6.2: SU(4) 20-plet baryon family with $J^P = (3/2)^+$

the lowest level represent baryons with no charm quark. The baryons in the second level have single charm quark. The higher level baryons have two or more charm quarks.

There are three main classes of theoretical models that are used to explain the baryon structure. The first one is the non-relativistic quark model. This model assumes that the baryons are made of three non-relativistic constituent quarks confined in a potential. The mass differences of multiplets of baryons and members of multiplets can be explained by spin-spin interactions of the constituent quarks via exchange of colored gluons. The mass split due to spin-spin interactions between the quarks is analogous to hyperfine splitting in QED due to spin-spin interactions. A very simple model for baryons, for example, can be constructed from the constituent quarks as

$$m(q_1q_2q_3) = m_1 + m_2 + m_3 + a\sum_{i<j}\frac{\overrightarrow{s_1}.\overrightarrow{s_2}}{m_i m_j}$$

where a is a free parameter. A second class of model is the Bag Model. This model treats hadrons as color singlet bags consisting of the perturbative vacuum occupied by the relativistic quarks and gluons in color singlet combinations. Thirdly, in Soliton Models, baryons are defined as localized accumulations of energy that is formed by quarks and mesons.

There are several studies in the literature which try to explain the mass spectrum of charmed baryons. The predictions of these models for the Ω_c^0 mass vary over a wide range between 2610 MeV/c^2 and 2786 MeV/c^2. Table 6.1 gives a summary of the predictions of these studies for the Ω_c^0 mass. All but [45] and [46] of the cited studies in Table 6.1 are models with a central potential. Samuel et al., uses scalar lattice QCD methods to predict the masses of hadrons. Izatt et al., calculates the spectrum of hadrons with a single charmed quark using a bag model.

Martin and Richard[48] calculate the Ω_c^0 mass with a potential model whose parameters have been determined by fitting the heavy meson spectrum. The central two

Table 6.1: Theoretical predictions of Ω_c^0 mass

By	Year	Mass (MeV/c^2)
Martin and Richard [48]	1995	2708
Roncaglia et al [49]	1995	2710
Rho et al [50]	1990	2786
Samuel et al., [45]	1986	2717
Richard et al., [51]	1983	2664
Izatt et al., [46]	1982	2610
Maltman et al., [52]	1980	2730
Chan et al., [53]	1977	2773
De Rujula et al., [54]	1975	2680

body potential that they use has a simple power law; $V = -8.064 + 6.8698r^{0.1}$.
In order to construct the interaction Hamiltonian, they add a spin-spin interaction term

$$V_{ss} = 1.112\frac{\overrightarrow{s_1}.\overrightarrow{s_2}}{m_1 m_2}\delta^3(\overrightarrow{r})$$

where m_i is the mass of the constituent quark. They tuned their model to reproduce the $J/\psi - \eta_c$ hyperfine splitting of charmonium. They can reproduce some of the measured heavy meson masses like $c\bar{c}$, $b\bar{b}$, $s\bar{s}$, $c\bar{s}$. They predict the mass of the Ω_c^0 to be 2708 MeV/c^2. It will be shown later in this thesis that our measurement for the Ω_c^0 mass agrees well with this model's prediction.

As it can be seen, theoretical models make different assumptions obout the quark-quark interactions and use some measured parameters to tune their predictions. Therefore statistically sound experimental measurements are important for understanding the

charmed baryons, and in particular, Ω_c^0 .

6.2.2 Charmed Baryon Weak Decay

Charm is conserved in strong and electromagnetic interactions. Therefore its decay can only be via the weak interactions. Charmed baryon weak decays can occur in two ways: hadronic and semi-leptonic, depending on the final state particles. The dynamics of the charmed baryon decays are mainly determined by the strong interactions between the quarks in the decaying baryon and the weakly decaying charm quark. The charm quark can decay into a strange quark or a down quark through the emission of W^+-boson. The W^+ in turn decays into either a quark anti-quark pair ($q\bar{q}$) or a lepton pair. The Cabbibo-GIM formalism describes the quark states involved in the weak interaction. Considering only u, d, c, and s quarks, the weak charged current can be written as

$$J^+_{weak} = (\bar{u}\bar{c})\gamma^\mu(1-\gamma^5)\begin{pmatrix} cos\theta_c & sin\theta_c \\ -sin\theta_c & cos\theta_c \end{pmatrix}\begin{pmatrix} d \\ s \end{pmatrix}$$

The experimental data confirms that a unique Cabbibo angle θ_c[1] $\simeq 13^o$ explains the data well. Since $\theta_c = 13^o$ is a small angle, amplitudes proportional to $cos\theta_c$ are close to unity and therefore called Cabbibo Favored (CF) and those proportional to $sin\theta_c$ are called Cabbibo Suppressed (CS). This formalism can be extended by the inclusion of the t and b quarks as

$$J^+_{weak} = (\bar{u}\bar{c}\bar{t})\gamma^\mu(1-\gamma^5)\mathbf{V_{KM}}\begin{pmatrix} d \\ s \\ b \end{pmatrix}$$

where $\mathbf{V_{KM}}$ is the Kobayashi-Maskawa [55] matrix and is given as

[1] One can interpret θ_c as the probability that one flavor of quark will change into another under some weak force action

$$\mathbf{V_{KM}} = \begin{pmatrix} c_1 & -s_1c_3 & -s_1s_3 \\ s_1c_2 & c_1c_2c_3 - s_2s_3e^{i\delta} & c_1c_2s_3 + s_2c_3e^{i\delta} \\ s_1s_2 & c_1s_2c_3 + c_2s_3e^{i\delta} & c_1s_2s_3 - c_2c_3e^{i\delta} \end{pmatrix}$$

In this representation c_i and s_i refer to $cos\theta_i$ and $sin\theta_i$ and the θ_i is the mixing angle. The experimentally measured values of the elements of matrix are [21];

$$\begin{pmatrix} |V_{ud}| & |V_{us}| & |V_{ub}| \\ |V_{cd}| & |V_{cs}| & |V_{cb}| \\ |V_{td}| & |V_{ts}| & |V_{tb}| \end{pmatrix} = \begin{pmatrix} 0.974 - 0.976 & 0.219 - 0.226 & 0.0025 - 0.0048 \\ 0.219 - 0.226 & 0.9732 - 0.9748 & 0.038 - 0.044 \\ 0.004 - 0.014 & 0.037 - 0.044 & 0.9990 - 0.9993 \end{pmatrix}$$

The decay of Ω_c^0 into Ω^- and Ξ^- final state hyperons occurs via the direct decay of the c-quark into an s-quark by the emission of a W^+ boson ($c \rightarrow sW^+$ ($W^+ \rightarrow u\bar{d}$)). Quark-antiquark, $q\bar{q}$, pairs created in the process out of the vacuum determine the final particles and hence the decay mode. The Feyman diagrams for this process for the three decay modes of Ω_c^0 is shown in figure 6.3. Figure 6.3(a) shows the hadronization process for $\Omega_c^0 \rightarrow \Omega^-\pi^+$ decay. The decay products of W^+, u and $\bar{d}$ quarks, hadronize into a π^+ and the three s quarks form the Ω^- hyperon. The two s-quarks of the Ω_c^0 act as spectators in this process and therefore this diagram is called an *external spectator* diagram. In figure 6.3(b), the weak decay diagram of $\Omega_c^0 \rightarrow \Xi^-K^-\pi^+\pi^+$ is shown. In this case, the $q\bar{q}$ pairs interact with the $W^+ \rightarrow u\bar{d}$ in the formation of the two π^+'s. Ξ^- is formed out of the two spectator s-quarks and a d quark. This is an example of the *internal spectator* diagram. In figure 6.3(c), the decay diagram for $\Omega_c^0 \rightarrow \Omega^-\pi^-\pi^+\pi^+$ is shown.

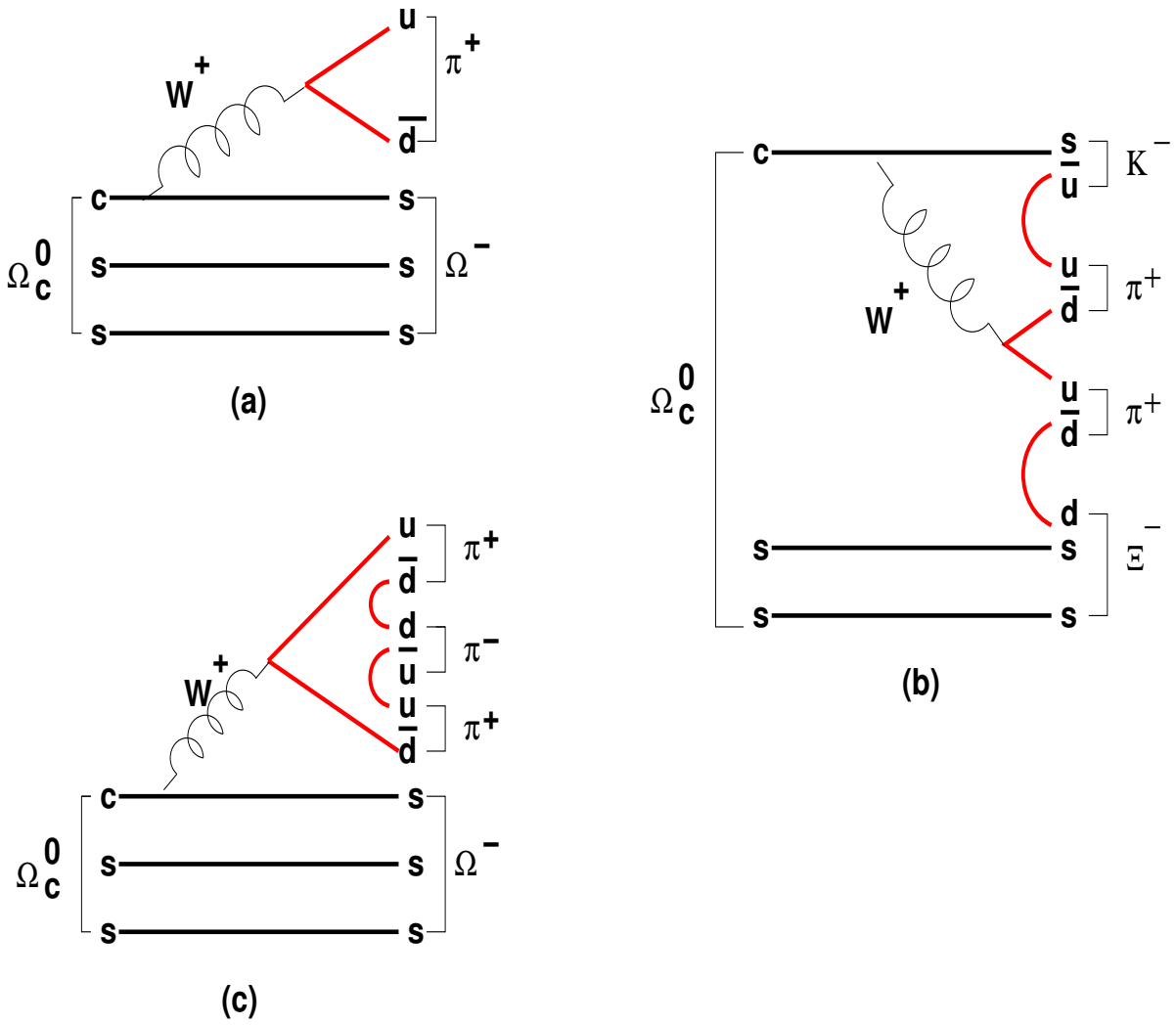

Figure 6.3: The quark diagrams for for three Ω_c^0 decay modes are shown: (a) $\Omega_c^0 \to \Omega^-\pi^+$, (b) $\Omega_c^0 \to \Xi^- K^-\pi^+\pi^+$, and (c) $\Omega_c^0 \to \Omega^-\pi^-\pi^+\pi^+$.

6.3 Experimental Observation of Charmed Particles

Some charmed particles can be observed either directly by observing their flight path and decay vertex or indirectly by observing their decay products. The Ω_c^0 is a neutral particle. Therefore it does not leave any trace in the detector. Besides it has an extremely short lifetime, in fact the shortest of all the singly charmed baryons. Therefore it is impossible to detect it by observing its flight trajectory. Instead its mass is reconstructed from its decay products. In hadron-hadron interactions, heavy flavored

particles are created rarely compared to the high number of light particles. Most of these particles could wrongly be interpreted as if they are the decay products of a heavier particle. This creates a huge combinatorial background. The typical decay lengths of charmed particles are of the order of a few millimeters (a few hundred μm times the Lorentz boost, typically $\gamma \sim 100$).

6.4 Experimental Measurements of Ω_c^0 Mass

There are several measured values for Ω_c^0 mass. However the number of events observed is very small.

WA62 [43] experiment of CERN reported three events for the decay mode $\Omega_c^0 \rightarrow \Xi^- K^- \pi^+ \pi^+$ with a mass of 2740 $\pm$ 20 MeV/c^2. WA62 used a 135 GeV/c, Σ^- beam on a beryllium target.

ARGUS [56] collaboration used $e^- e^+$ interactions at $\sqrt{s}$=10 GeV/c^2 center of mass energy, reported evidence for the production of Ω_c^0. They observed 12.5$\pm$4.5 events in $\Omega_c^0 \rightarrow \Xi^- K^- \pi^+ \pi^+$ decay mode and 6.5$\pm$3.2 events in $\Omega_c^0 \rightarrow \Omega^- \pi^- \pi^+ \pi^+$ mode at a mass of 2719 $\pm$ 7.0 $\pm$ 2.5 MeV/c^2 in $e^- e^+$ interactions.

E687 [57] experiment of FermiLab presented evidence for signals for the decay channels $\Omega_c^0 \rightarrow \Omega^- \pi^+$ (10.3$\pm$3.9 events) at a mass 2705.9$\pm$3.3 $\pm$ 2.3 MeV/c^2 and $\Omega_c^0 \rightarrow \Sigma^+ K^- K^- \pi^+$ (42.5$\pm$8.8 events) at a mass of 2699.9$\pm$1.5 $\pm$ 2.5 MeV/c^2.

The CLEO [58] collaboration, which also used $e^- e^+$ interactions at $\sqrt{s}$=10 GeV/c^2 center of mass energy like the ARGUS collaboration, reported no evidence for $\Omega_c^0 \rightarrow \Xi^- K^- \pi^+ \pi^+$ with a 90% CL upper limit on the $(\sigma \cdot Br)$ of 0.40 pb as opposed to ARGUS's 2.41$\pm$0.90 $\pm$0.30 pb result. CLEO collaboration's later analysis [59] with the CLEO II and upgraded CLEO IV data, reported a total of 40.4 $\pm$ 9.0 events in five decay modes ($\Omega^- \pi^+$, $\Omega^- \pi^+ \pi^0$, $\Xi^- K^- \pi^+ \pi^+$, $\Omega^- \pi^- \pi^+ \pi^+$and $\Xi^0 K^- \pi^+$) at a mass of 2694.6 $\pm$ 2.6 $\pm$ 1.9 MeV/c^2.

The WA89 [60] experiment of CERN observed seven decay modes with Λ, Ξ^- or

Ω^- in the final states. These decay channels are: $\Omega^-\pi^+$, $\Omega^-\pi^-\pi^+\pi^+$, $\Xi^-K^-\pi^+\pi^+$, Ξ^- K_s^0 π^+, Ξ^- K_s^0 π^+ π^+ π^-, Λ K_s^0 K^- π^+ and Λ K^- K^- π^+ π^+ at an average mass of $2708.3 \pm 1.0 \pm 1.6$ MeV/c^2.

The most recent results for Ω_c^0 came from the FOCUS [61] experiment (FNAL-E831). They report observation of Ω_c^0 in $\Omega^-\pi^+$ and $\Xi^-K^-\pi^+\pi^+$ modes with 64 ± 14 events at a mass of 2698 MeV/c^2. FOCUS is a photo-production experiment. A photon beam, which is derived from the bremsstrahlung of secondary electrons (E_{max} =250 GeV) produced from the Tevatron proton beam is incident on a beryllium target.

Only five relative decay fractions are reported in the latest Particle Data Group (PDG) [44] data summary. These are

- $\mathcal{B}(\Sigma^+K^-K^-\pi^+)/\mathcal{B}(\Omega^-\pi^+) < 4.8$
- $\mathcal{B}(\Xi^0K^-\pi^+)/\mathcal{B}(\Omega^-\pi^+) \sim 4.0 \pm 2.5 \pm 0.4$
- $\mathcal{B}(\Xi^-K^-\pi^+\pi^+)/\mathcal{B}(\Omega^-\pi^+) \sim 1.6 \pm 1.1 \pm 0.4$
- $\mathcal{B}(\Omega^-\pi^+)/\mathcal{B}(\Omega^-e^+\nu_e) \sim 0.41 \pm 0.19 \pm 0.04$
- $\mathcal{B}(\Omega^-\pi^+\pi^0)/\mathcal{B}(\Omega^-\pi^+) \sim 4.2 \pm 2.2 \pm 0.9$.

For $\mathcal{B}(\Omega^-\pi^-\pi^+\pi^+)/\mathcal{B}(\Omega^-\pi^+)$ there are two measurements published: [57] and [59] quotes upper limits as < 0.56 and < 1.6 respectively. However the PDG does not quote any value for the relative decay fraction for these decay modes.

In this thesis , we report the observation of 107 ± 22 Ω_c^0 candidate events [62] with the SELEX detector, which is currently the world's largest sample, at a mass of $2708 \pm 1.8 \pm 2.6$ MeV/c^2. The $\mathcal{B}(\Omega^-\pi^-\pi^+\pi^+)/\mathcal{B}(\Omega^-\pi^+)$ measurement is also presented.

CHAPTER 7
E781 SELEX EXPERIMENTAL SETUP

The SELEX experimental setup consisted of a beam line, a target area and a multistage spectrometer (figure 7.1). We will describe the major components of the detector in more detail in below:

7.1 Coordinate System

The origin of the SELEX coordinate system is chosen to be at the end of the target region. The beam direction is chosen to be the z-axis, the y-axis points vertically upward.

7.2 Beam and Beam Spectrometer:

The Fermilab Proton Center hyperon facility provided the Σ^- and π^- beams at 600 GeV/c and p and π^+ beams at 540 GeV/c. Before the beam particles hit the charm targets, they pass through the beam spectrometer. The beam spectrometer is composed of Hyperon Magnet, Beam Transition Radiation Detector (BTRD) and the Beam Silicon Strip Detectors (BSSD). The aim of the beam spectrometer is to characterize the beam. BTRD identifies the particle, and the BSSD measures the direction and momentum of the beam particles.

7.3 Targets and Vertex Spectrometer

There are 5 targets, 3 carbon and 2 copper, separated by 1.5 cm. The target properties are summarized in table 7.1. The vertex silicon detectors come after the targets. They detect tracks created in the beam-target interactions. Hence primary and secondary vertices can be differentiated. Their angular resolution is 30 μrad for 100 GeV/c tracks.

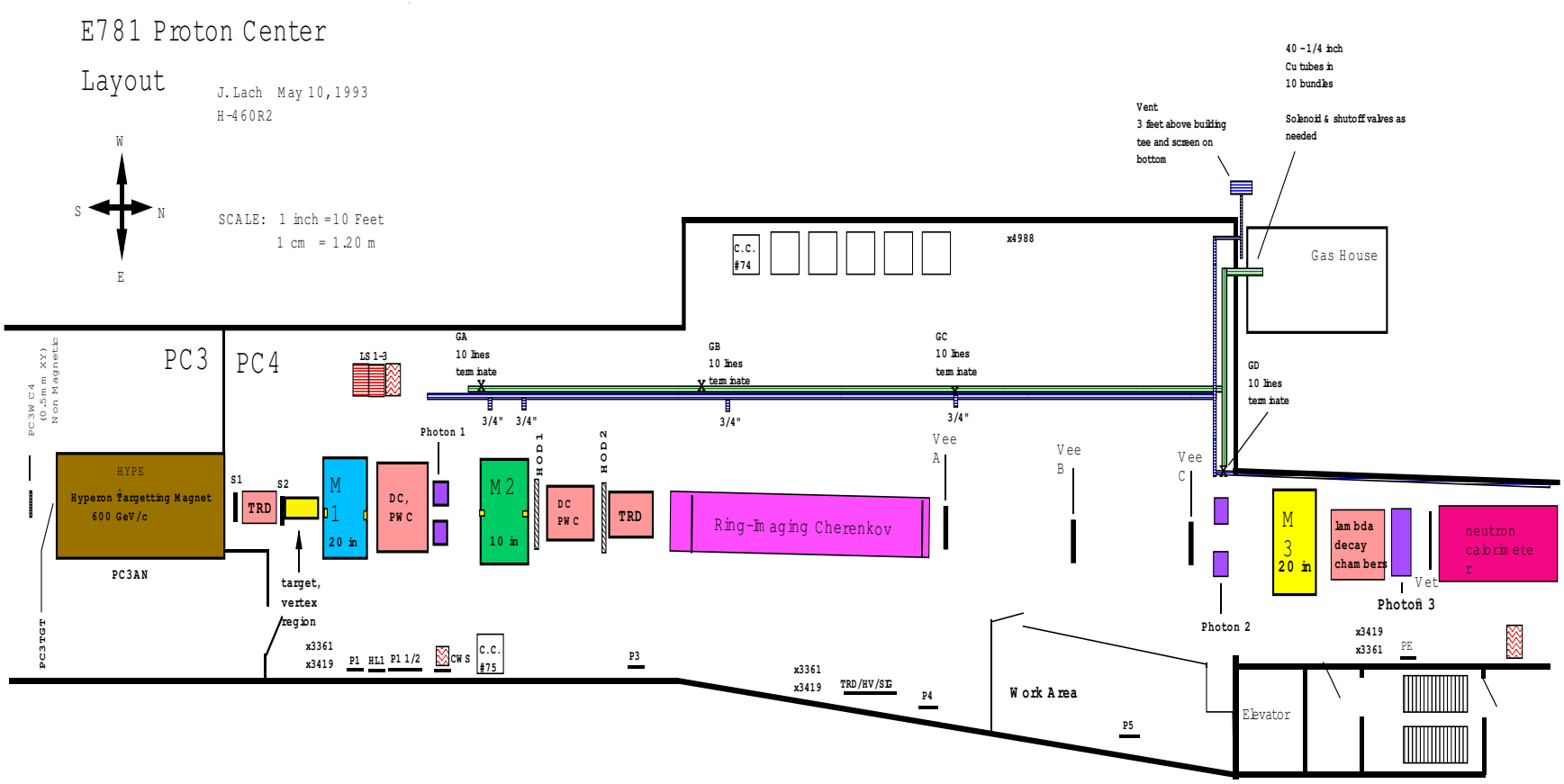

Figure 7.1: E781 SELEX Detector Layout

Table 7.1: Target properties

target	thickness [mm]	z [cm]	Density $[g/cm^3]$
Cu	1.6	-6.08	8.96
Cu	1.1	-4.55	8.96
C	2.2	-3.11	3.20
C	2.2	-1.61	3.20
C	2.2	-0.11	3.20

7.4 M1 Spectrometer

The M1 spectrometer is made up of a magnet with 1.3 T magnetic field which gives a transverse momentum, p_t, kick of 0.74 GeV/c, large angle silicon micro-strip detector (LASD), proportional wire chambers (PWC), drift chambers (DC), and a photon calorimeter. Low energy particles from the vertex region are tagged and photon energies are measured at this stage. The M1 spectrometer plays a crucial role in measuring the momentum of upstream tracks. The M1 spectrometer has three wire chambers measuring x, y, u, and v projections. u and v projections are at 28 degrees on each side of the x projection. The M1 spectrometer was built at the University of Iowa.

Two large area silicon detectors (LASD) are stationed in the M1 spectrometer; one at the end of the M1 magnet, the other at the beginning of the M2 magnet. A third LASD station is at the end of the M2 magnet.

7.5 M2 Spectrometer

The M2 spectrometer consists of a magnet with a 1.5 T magnetic field and a momentum kick of p_t=0.845 GeV/c, LASDs, PWCs, two hodoscopes, an electron TRD

and Ring Imaging CHerenkov (RICH) detector. It is designed to detect particles with momentum larger than 15 GeV/c. These particles are mostly decay products of charmed baryons with $x_F > 0.1$.

The RICH detector is used for particle identification. It consists of 16 hexagonal spherical mirrors. As explained earlier in section 2.5, the Cherenkov light is generated in a cone whose opening angle is determined by the particle's velocity

$$cos\theta = 1/\beta n(w) \tag{7.1}$$

where

$$\beta = v/c \tag{7.2}$$

The observed ring's radius (see figure 7.2) is therefore a function of the velocity of the particle. A greater velocity of the particle gives rise to a greater radius of the ring (figure 7.3) [69][70].

One can then measure the ring radius and calculate the opening angle θ and the energy of this particle. A maximum likelihood analysis algorithm is run for each track's particle identification. In figure 7.4 a sample single RICH event display is shown. In this particular event, four rings corresponding to four tracks are seen. The calculated momenta and particle IDs are also shown in this figure. The red ring, for example,

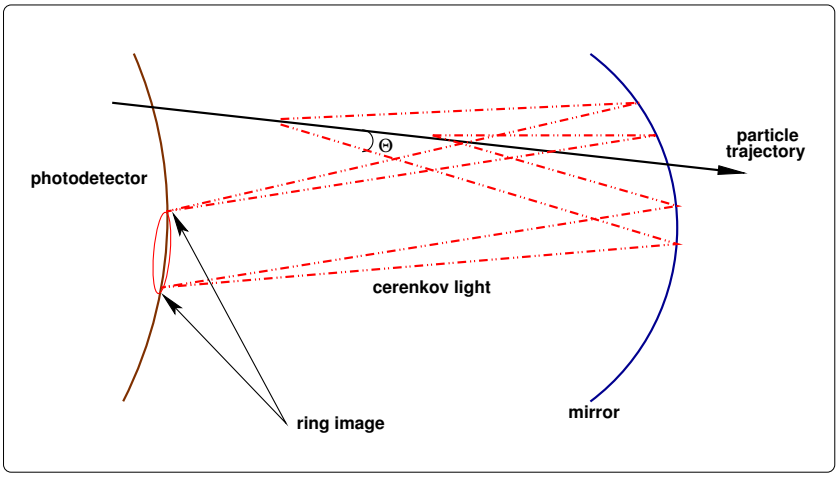

Figure 7.2: Schematic view of Ring Imaging Cherenkov counter

corresponds to a K^- with a 154 GeV/c momentum.

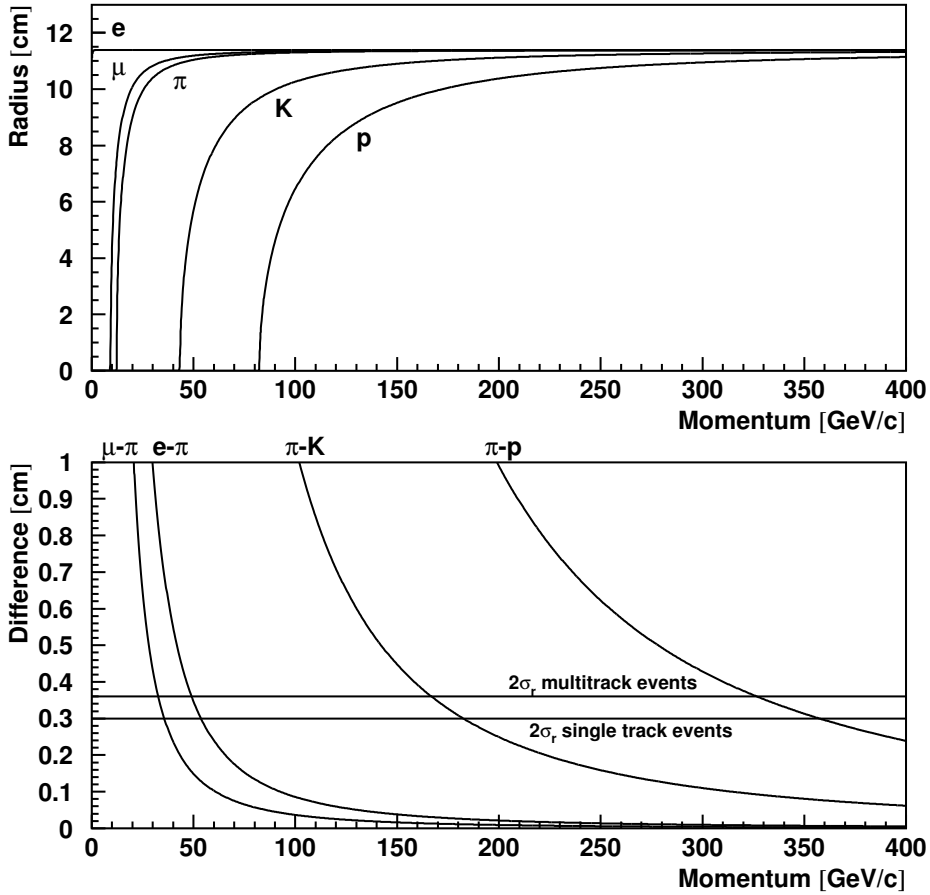

Figure 7.3: Ring radii and separation for different particles

RICH detector achieves a K/π separation up to 165GeV/c. In our analysis, RICH played an important role. As it will be explained later, particle identification by RICH was used in order to differentiate the daughter particle of hyperons.

7.6 M3 Spectrometer

The M3 is the last spectrometer, which consists of a magnet, PWCs, drift chamber, photon calorimeter and a neutron calorimeter. A 1.3 T magnetic field provides a momentum kick of p_t=0.72 GeV/c. The M3 spectrometer was built jointly by the

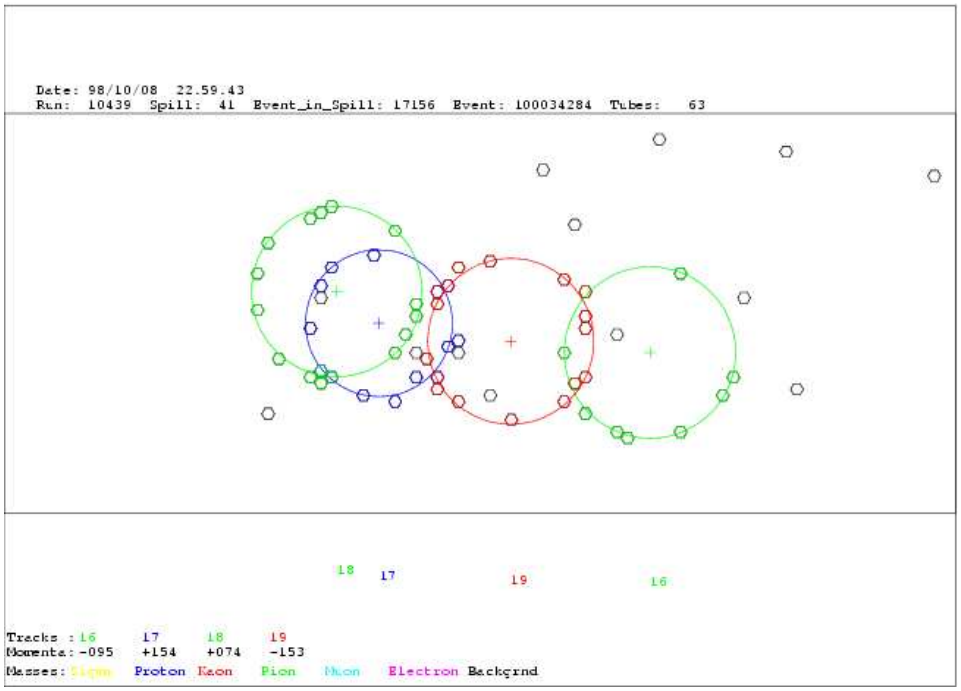

Figure 7.4: A single event in RICH

University of Iowa and the Trieste groups.

7.7 Detectors used in this analysis

For the Ω_c^0 search, not all detectors were used. Silicon strip detectors measured the beam and primary and secondary vertex tracks. The momenta of the tracks were measured by the PWCs, drift chambers and silicon strip detectors after they were deflected by the magnetic fields of the M1 and the M2 magnets. The RICH detector provided the particle identification information for the hyperon's daughter particles.

CHAPTER 8
Ω_c^0 SEARCH IN SELEX

The processing of the SELEX raw data was done in 1998 and called Pass I. Since then there were some improvements in the reconstruction packages of the off-line program, SOAP, especially in "Kink", "downstream Vee" and "Photon" packages. In the Pass II phase, the raw SELEX data was refined one more time with these improved reconstruction algorithms. One of the big improvements is in the RICH particle identification capabilities. RICH is now capable of identifying Σ^-, Σ^+, Ξ^-, Ξ^+ and Ω^- particles up to 300 GeV/c. Another improvement is the addition of new reconstruction packages to Selex Offline Analysis Program, SOAP. V0 reconstruction, for example, is a new reconstruction package added to SOAP, which searches for two-prong decay vertices of opposite charged tracks. The "kink by disappearance", KBD, reconstruction package is also improved which searches for hyperon partial reconstruction where there is a track recorded by the M1 spectrometer but not by M2.

8.1 Data Set

The charm trigger is very loose. It requires a valid beam track, at least 4 charged secondaries in the forward 150 mrad cone, and two hodoscope hits after the second bending magnet from tracks of charge opposite to that of the beam. We triggered on about 1/3 of all inelastic interactions. A computational filter linked PWC tracks having momenta > 15 GeV/c to hits in the vertex silicon and made a full reconstruction of primary and secondary vertices in the event. Events consistent with only a primary vertex are not saved. About 1/8 of all triggers are written to tape, for a final sample of about 10^9 events.

In the full analysis, the vertex reconstruction was repeated with tracks of all momenta. Again, only events inconsistent with having a single primary vertex were considered. The RICH detector identified charged tracks above 25 GeV/c. The simulated

reconstruction efficiency of any charmed state is constant at about 40% for $x_F > 0.3$ where $> 60\%$ of SELEX events lie.

In this analysis, we use all data available in Pass II. The raw data was converted into ROOT[71] format by using Roottools [72]. We studied the following Ω_c^0 decay modes:

- $\Omega_c^0 \to \Omega^- \pi^+$
- $\Omega_c^0 \to \Omega^- \pi^- \pi^+ \pi^+$
- $\Omega_c^0 \to \Xi^- K^- \pi^+ \pi^+$

8.2 Hyperon Reconstruction

The Ω_c^0 decays into a hyperon and mesons. In order to reconstruct the decay, an algorithm called "kink by disappearance" was used. When the hyperons decay into the aperture of M1 before the MultiWire Propotional Chambers (MWPC) the decay topology is called "kink". They are represented by one charged track that decays to another charged particle and a neutral particle undetected by the spectrometer. The algorithm loops over all tracks and isolates the unlinked micro-strip vertex tracks that point to the M1 aperture and then pairs them with all unlinked MWPC tracks. A rough estimate of the x and z coordinates is computed. The momentum of the parent particles, Ω^-, Ξ^- and $\Sigma^\pm$ is calculated by momentum conservation using the reconstructed momentum of the daughter particle. In the decays where there is a neutral strange particle (Λ^0), the tracks are paired with each Vee, which satisfies the Λ hypothesis. The parent particle must be consistent with originating from an upstream vertex. If the z kink coordinate is upstream of M1, the y distance is projected to the silicon vertex to eliminate spurious kinks. If the z kink coordinate is within M1 then one solution is found. If there are two solutions for the parent particle momentum both solutions are recorded for further analysis.

8.3 Charm Selection

The Ω_c^0 signal did not reveal itself when the Ω_c^0 invariant mass was plotted. It was immersed in a huge non-charm combinatorial background (See figure 8.1). Therefore it was necessary to devise and apply some cuts which are the signal selection criteria. In this section, the cuts that were thought to be possibly useful for the Ω_c^0 search will be described. Not all of them were used as will be explained in the following sections. Figure 8.2 shows the quantities from which the cuts are formed. These are as follows

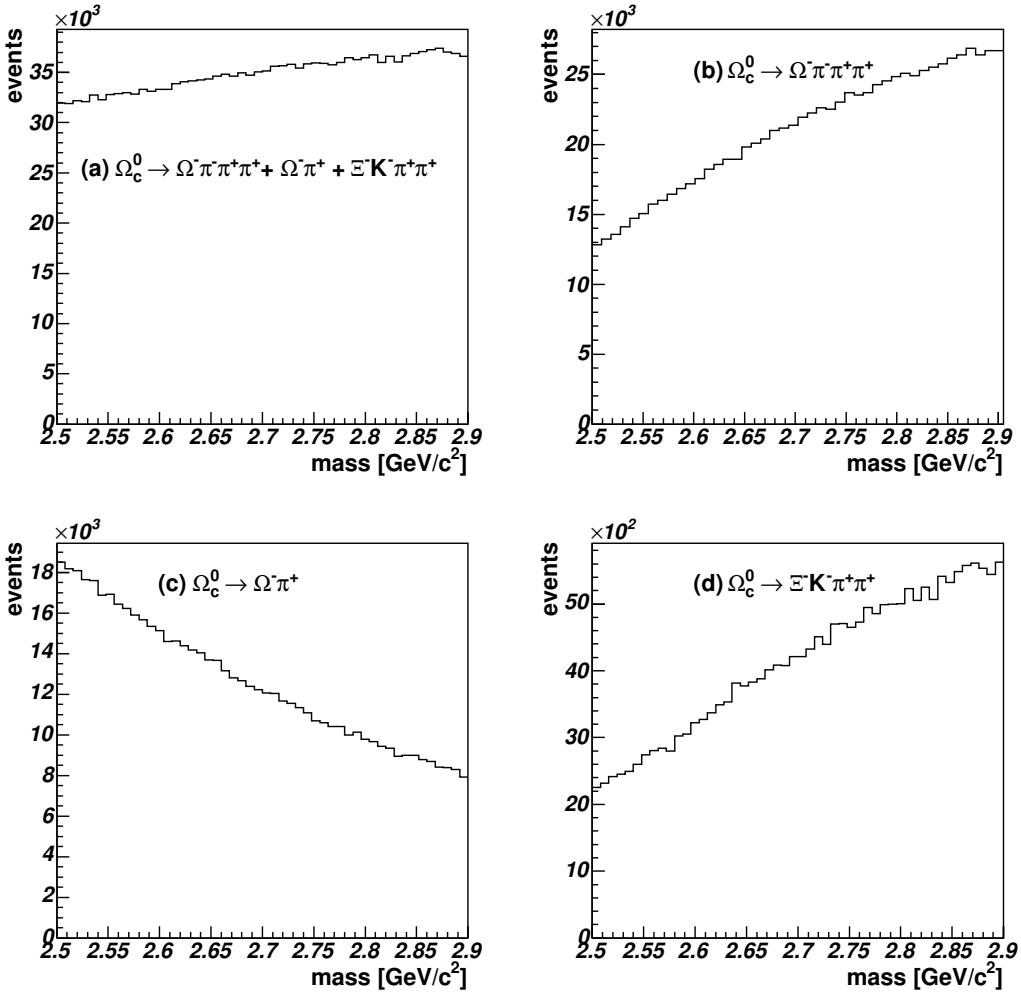

Figure 8.1: Ω_c^0 data without observation cuts: Top right $\Omega_c^0 \to \Omega^-\pi^-\pi^+\pi^+$, bottom left $\Omega_c^0 \to \Omega^-\pi^+$, bottom right $\Omega_c^0 \to \Xi^-K^-\pi^+\pi^+$, and top left the sum of three modes mentioned.

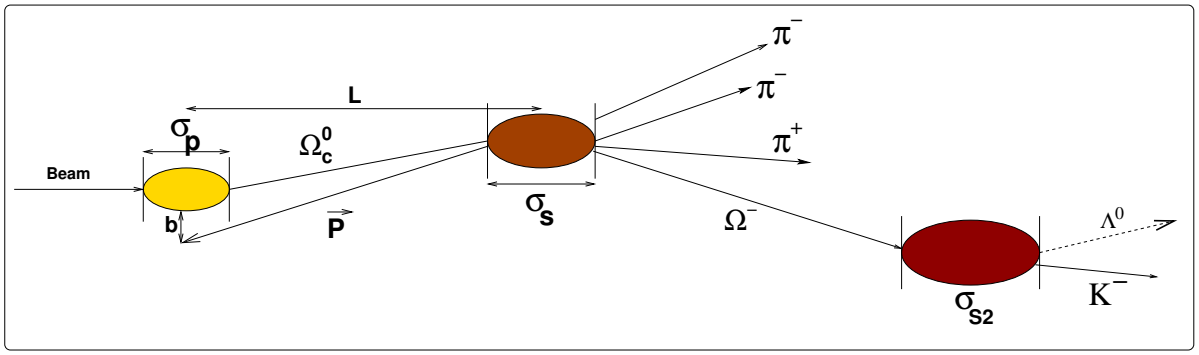

Figure 8.2: Graphical representation of the cuts

- l/σ_l cut: l is defined as (shown as L in figure 8.2) the distance between the primary and the secondary vertex. The primary vertex is the point where the beam particle interacts with the target and the Ω_c^0 is created. The secondary vertex is where the Ω_c^0 decays into several daughter particles depending on the decay mode. The decay vertex of the daughter hyperon of the Ω_c^0 is defined as the second secondary vertex. Since the angular separation between the 1^{st} and the 2^{nd} vertices are ($\leq$10 mrad), one can approximate the distance l as the difference between the z-coordinates of the primary and the secondary vertices. Each vertex coordinate also has an uncertainty associated with them due to the finite resolution of the detectors. They are represented as ellipses in figure 8.2 (shown as σ_p and σ_s). The uncertainty in the distance l is calculated as $\sigma_l = \sqrt{\sigma_p^2 + \sigma_s^2}$. The quantity l/σ_l is the ratio of l and σ.

- *pvtx* cut: The Ω_c^0's momentum vector, calculated from the sum of momenta of its daughters, is extrapolated back to the primary vertex. The *pvtx* is then calculated as the ratio of the impact parameter (shown as b in figure 8.2) and the impact parameter's error (b/σ_b).

- *dca* cut: The transverse distance between the hyperon (Ξ^- or Ω^-) track and its daughter meson (π^- or K^-) in the 2^{nd} secondary (*kink*) vertex is defined as the

distance of closest approach (dca). The smaller the dca, the better the vertex definition.

- Slow pion removal cut: There are many slow pions in the sample. The errors on these slow pion tracks are usually much larger than the high momentum tracks because of multiple scattering. Those tracks with a large error are more likely to be wrongly associated to a different vertex than to the vertex that they belong to. This gives rise to a combinatoric background.

- RICH particle identification probability cut: The particle identification of vertex tracks is done by the RICH detector. RICH calculates the likelihood for each track for being a pion, a proton, and kaon. This cut is especially important in the analysis as it removed events with the wrong secondary daughter track (K^- or π^-) associated with the hyperon daughter track (Ω^- or Ξ^-).

- tgt cut: There are five targets, 3 Carbon and 2 Copper. In the analysis, all targets were used.

8.3.1 Cut Significance

The selection cuts were chosen such that they reject as many background events as possible while keeping as many signal events as possible. This leads to a smaller statistical error. A general method of obtaining the maximum signal to noise ratio is the maximization of the quantity *significance*. Significance is defined as

$$significance = S/\sqrt{S+B}$$

where S is the number of signal events and B is the number of background events. However this method is not very useful when the number of signal events S is small compared to the number of background events. The expected number of Ω_c^0 events in the sample is only of the order of tens while a huge non-charm combinatorial background is seen. Therefore a slightly different approach was employed to overcome this problem.

In the significance calculation, the number of signal events was taken from Monte Carlo simulated events while the number of background events was taken from the data.

8.3.2 Ω_c^0 Analysis Cuts

In order to separate the signal from the non-charm background a general set of cuts was used for all decay modes as:

- both the primary and secondary vertices have $\chi^2/ndf < 5$
- the spatial separation l between the reconstructed production and decay vertices exceeds 6 times the combined error σ_l, $l/\sigma_l > 6$
- χ^2 of pvtx, $pvtx < 20$
- kink vertex tracks extrapolated to the *kink* vertex z position, must have a maximum transverse distance length at kink vertex ≤ 300 μm.

Aside from these general cuts, to help extract signal events from the background events, a few more cuts specific to the decay modes were employed as explained below:

$\Omega_c^0 \to \Omega^-\pi^-\pi^+\pi^+$ **mode:** A RICH probability cut on the daughter K^-, the kaon in the decay of $\Omega^- \to \Lambda^0 K^-$ is required to improve the selection of Ω^-. The probability of being identified as a K^- must be greater than 70% and also greater than the probability of being a proton (p) and a pion (π). The total transverse momentum of pions from $\Omega^-\pi^-\pi^+\pi^+$ decay must be greater than 0.35 GeV/c^2 relative to the Ω_c^0 direction.

$\Omega_c^0 \to \Omega^-\pi^+$ **mode:** As in the previous cases, the daughter K^-'s RICH probability must be greater than the probability of being a proton and a pion. The pion in the Ω_c^0 decay vertex is also required to have a momentum greater than 12 GeV/c.

$\Omega_c^0 \to \Xi^- K^-\pi^+\pi^+$ **mode:** Similar to the previous case, Ξ^-'s daughter π^-'s RICH probability must to be greater than the probability of being a proton and a kaon.

8.4 Monte Carlo Studies

For studies of branching decay fraction one has to know the detector acceptance and reconstruction efficiencies. For this purpose, SELEX has a tool called *event embedding* [73] which is incorporated in SOAP. With this tool, events which are generated with our preferred event generator are embedded with real data events. The real underlying data events serve as the real background events, and in this background the generated events are reconstructed. By knowing how many events are generated and how many of those are reconstructed, the total acceptance (reconstruction efficiency and the detector acceptance) can easily be calculated.

8.4.1 QQ Event Generator

QQ [74] was used for embedding event generation. QQ requires some input parameters specifying the nature of the event to be generated. First the particle of interest and its decay mode is defined as a text file. As an example, in Table 8.1, a decay chain of $\Omega_c^0 \to \Omega^-\pi^-\pi^+\pi^+$, $\Omega^- \to \Lambda^0 K^-$, $\Lambda^0 \to \pi^- p$ is shown. The branching ratios for each decay can also be defined. In the example shown, all decays have 100% branching ratios. Similarly, in a decay control file, the number of events to be generated, the beam particle type, momentum, mean transverse momentum, the X_F distribution power are defined. With the parameters defined in control and decay files, QQ generates the event as the particle trajectory parameters. Each tracks' starting points (x, y, z), the first three columns, its directional cosines $(\alpha x, \alpha y, \alpha z)$, and the momentum and the particle mass are recorded in a text file. An example of QQ generated $\Omega_c^0 \to \Omega^-\pi^+$ events is shown in Table 8.3. Each track is read by SOAP and translated and rotated in the detector. Multiple Coulomb scattering smearing effects and detector resolution effects are taken into account when the tracks are used to fill the detector hit banks. Each event is then passed through SOAP for the reconstruction.

Table 8.1: QQ sample decay file for $\Omega_c^0 \rightarrow \Omega^-\pi^-\pi^+\pi^+$

DECAY CSS1	
CHANNEL	0 1.0000 OME- PI+ PI- PI+
ENDDECAY	
DECAY OME-	
CHANNEL	0 1.0000 LAM K-
ENDDECAY	
DECAY LAM	
CHANNEL	0 1.0000 P+ PI-
ENDDECAY	

Table 8.2: QQ sample decay control file

nevent 1000	! number of events
decay_id 4332	! Ω_c^0 StdHEP ID number
beam_id 3112	! Σ^- StdHEP ID number
beam_momentum 600.0	! beam momentum
mean_pt 1.0	! p_t distribution
xf_power 4.0	! X_f distribution
data_out oc0_oiii.dat	! Output Embedded file
hist_out oc0_oiii.hbk	! Output Histogram file
decay_file xic_lkii.dec	! Input File with decay mode

Table 8.3: QQ generated for $\Omega_c^0 \rightarrow \Omega^-\pi^+$ decay

x	y	z	αx	αy	αz	p	mass
0.0000	0.0001	0.050	0.004260	0.006507	0.999970	109.95	1.672
0.0000	0.0001	0.050	-0.018517	-0.021425	0.999599	26.23	0.140
2.3141	3.4516	534.345	-0.001941	0.005115	0.999985	31.07	0.494
3.8865	5.0293	762.231	0.005982	0.007691	0.999953	61.91	0.938
3.8865	5.0293	762.231	0.010245	0.004120	0.999939	16.97	0.140

8.4.2 Ω_c^0 Embedding Studies

In order to see how well the embedded Monte Carlo simulates the data, several properties of the Ω_c^0 decays were examined with both data and Monte Carlo events. In figure 8.3(a), the primary vertex distributions are shown. The primary vertex is the one where the beam particle interacts with the target and Ω_c^0 is created. The solid histogram is the Monte Carlo and the dashed histogram is the data. The positions of the five targets are clearly seen. Similarly, in figure 8.3(b), the secondary vertex that Ω_c^0 decays, is seen. Again the solid histogram is from the Monte Carlo and the dashed one is the data.

Several momentum distributions of the decay product particles were also compared. In figures 8.3(c) and 8.3(d), for example, the π^- and π^+ z-component momentum distributions, p_z, are plotted respectively. The solid histogram in these plots is again the data, the filled circles are Monte Carlo. As a final check, the Ω_c^0 momentum distributions after the observation cuts for the Monte Carlo and the data are compared (figure 8.4). Hence the conclusion is that QQ embedded Monte Carlo simulates our detector and describes the data well. For each decay mode, several Monte Carlo samples were generated with different numbers of events with transverse momentum of p_t=1 GeV/c. The Ω_c^0 input

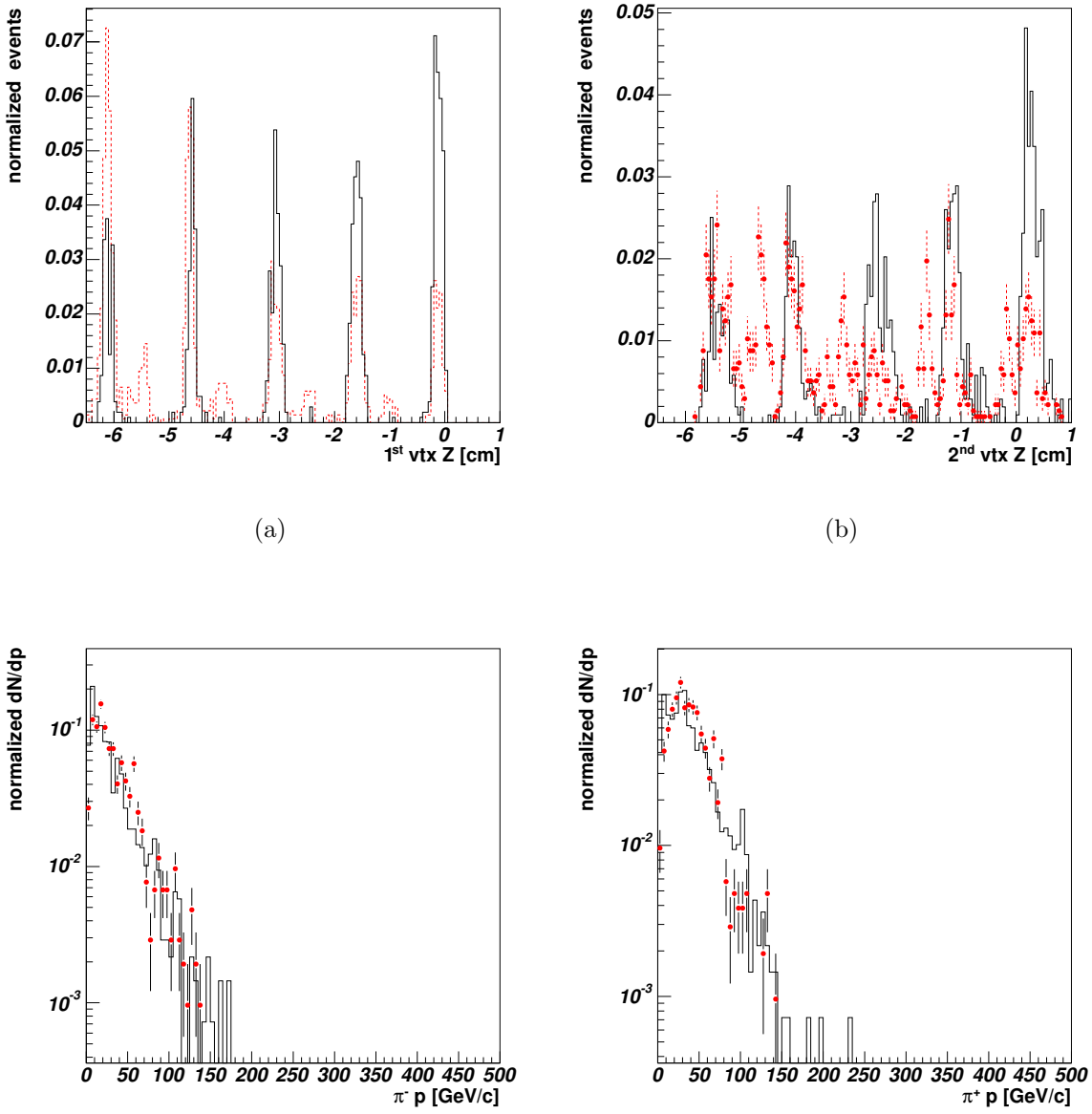

(a) (b)

(c) (d)

Figure 8.3: QQ embedded Monte Carlo (dashed histogram and filled circles) and data (solid histogram) comparison after the observation cuts: (a) primary vertex z-position, (b) secondary vertex z-position, (c) π^- p_z and (d) π^+ p_z

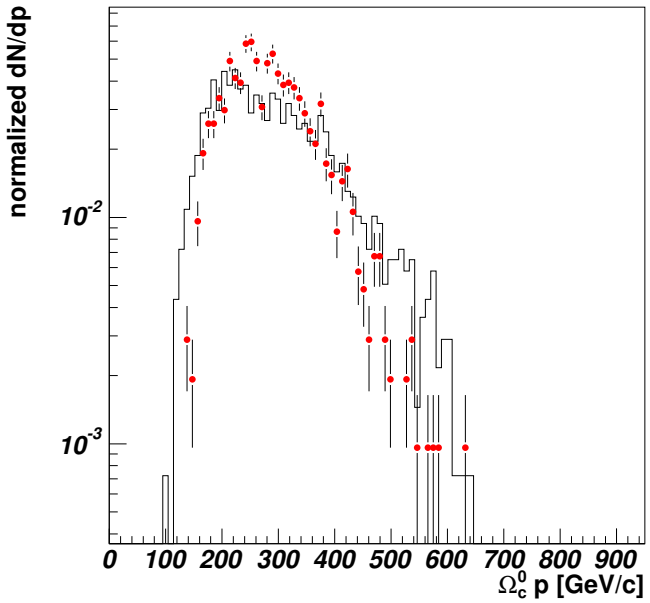

Figure 8.4: Ω_c^0 p_z after observation cuts for data (histogram) and MC (points)

mass to QQ was 2704 MeV/^{2} and the input Ω_c^0 lifetime was 64 fs. For the acceptance calculation, the number of reconstructed events has to be known accurately. In order to accommodate both *well* and *poorly* reconstructed events, a sum of two Gaussians with the same mean but different σ values (see *sgauss.for* in [75]) + second order polynomial function (*pol2*), was used. The second Gaussian has only a fraction of the events of the first one. Two different histogram binnings were investigated (see figures 8.5(a), 8.5(b), 8.5(c), 8.5(d)). The results are tabulated in table 8.4. The ratio of reconstructed events to generated events, $\epsilon_{acc} = N_{Rec}/N_{Gen}$, for $\Omega_c^0 \rightarrow \Omega^-\pi^+$ decay mode is 0.053 and for $\Omega_c^0 \rightarrow \Omega^-\pi^-\pi^+\pi^+$ mode is 0.044. ϵ_{acc} represents the total acceptance for the decay modes $\Omega_c^0 \rightarrow \Omega^-\pi^+$ and $\Omega_c^0 \rightarrow \Omega^-\pi^-\pi^+\pi^+$. It should be noted again that the events shown in these plots were not obtained with any cuts but just the results of the SOAP reconstruction. Therefore the acceptance values quoted, ϵ_{acc}, do not yet include the cut efficiencies.

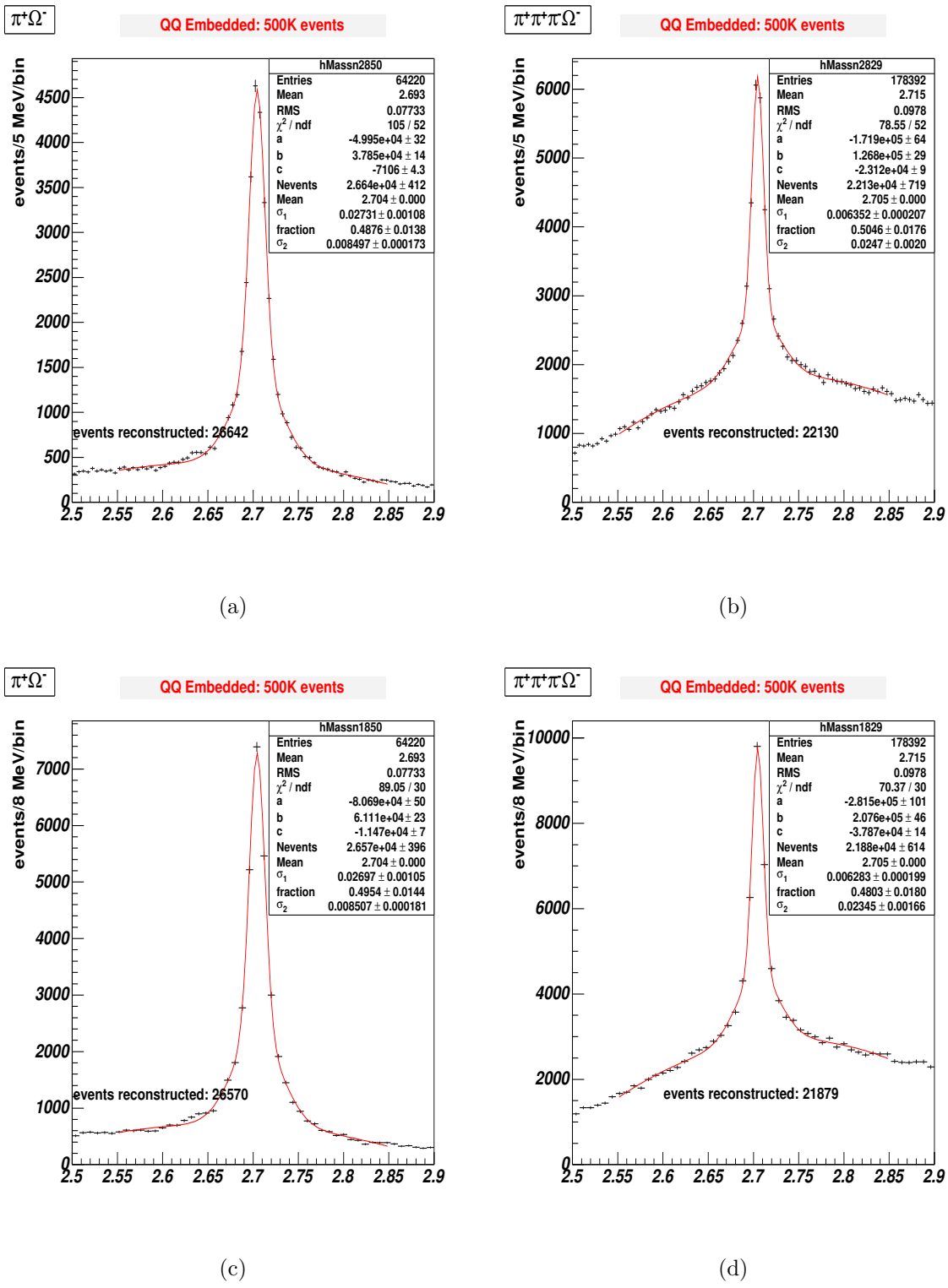

Figure 8.5: Reconstructed Monte Carlo events fitted with two Gaussians + 2^{nd} order polynomial; $\Omega_c^0 \to \Omega^-\pi^+$ with (a) 5 MeV/bin and (c) 8 MeV/bin, $\Omega_c^0 \to \Omega^-\pi^-\pi^+\pi^+$ with (b) 5 MeV/bin and (d) 8 MeV/bin

Table 8.4: Summary of QQ embedding study results

Bin size	Decay mode	σ_1 GeV/c^2	σ_2 GeV/c^2	mass GeV/c^2	χ^2/ndf	N_{Rec}/N_{Gen}
5MeV	$\Omega^-\pi^+$	0.027	0.009	2.704	105.00/52	0.0533
	$\Omega^-\pi^-\pi^+\pi^+$	0.006	0.024	2.705	78.55/52	0.0443
8MeV	$\Omega^-\pi^+$	0.027	0.009	2.704	89.05/30	0.0514
	$\Omega^-\pi^-\pi^+\pi^+$	0.006	0.023	2.705	70.37/30	0.0438

8.5 Ω_c^0 Observation

A total of 107 $\pm$ 22 Ω_c^0 candidate events pass the cuts explained above and their break down into three decay modes are summarized in table 8.5 (Also see figure 8.6). The number of signal events are calculated from the fit of the form of a Gaussian plus a second order polynomial which characterized the background. In the $\Xi^-K^-\pi^+\pi^+$ decay mode, 28 ± 12 events are observed with a significance of $S/\sqrt{B} = 5.4$. A total of 44 ± 14 events with a significance of $S/\sqrt{B} = 4.9$ are observed in the $\Omega^-\pi^-\pi^+\pi^+$ decay mode. The $\Omega^-\pi^+$ decay mode has 35 ± 12 events with a significance of $S/\sqrt{B} = 3.2$. When the three decay modes are combined and fitted as shown in figure 8.6(d), the fit yields the same total number of 107 ± 26 events. The signal significance $S/\sqrt{B}$ for the sum of the three decay modes is calculated as 6.8.

The Ω_c^0 invariant mass is measured as 2708.0 $\pm$ 1.8 $\pm$ 2.6 MeV/c^2. The systematic error was obtained by comparing the SELEX Ξ_c^+ mass measurement to the current world average in PDG. Recent FOCUS[61] measurement for the Ω_c^0 mass is 2697.5$\pm$2.2 MeV/c^2. Our measurement is 3.7 ($=(2708.0-2697.5)/\sqrt{1.8^2+2.2^2}$) standard deviations above the FOCUS measurement. We believe our mass measurement is quite accurate because the previous SELEX charm invariant mass measurements such as D,D_s and Λ_c

Table 8.5: Invariant mass results and signal yields for observed Ω_c^0 modes.

Ω_c^0	$Mass$(MeV/c^2)	Signal Events	$S/\sqrt{B}$
$\Omega^-\pi^+\pi^+\pi^-$	2708.0 ± 4.5	44 ± 14	4.9
$\Omega^-\pi^+$	2708.0 ± 2.0	35 ± 12	3.2
$\Xi^-K^-\pi^+\pi^+$	2703.0 ± 8.0	28 ± 12	5.4
	Weighted Average	Total	
	2708 ± 1.8	107 ± 22	6.8

agree well with the world average [44]. The mass resolution and accuracy is confirmed also by Monte Carlo studies. In our embedded Monte Carlo study, the Ω_c^0 mass was defined as 2704 MeV/c^2. After passing our observation cuts, we get a mean mass value of 2704 MeV/c^2 for the Monte Carlo study. Therefore we conclude that there is no systematic shift in the reconstructed mass for the Ω_c^0.

The mass resolution of the $\Omega_c^0 \rightarrow \Xi^-K^-\pi^+\pi^+$ decay mode, σ ~19 MeV/c^2, is considerably worse compared with $\Omega_c^0 \rightarrow \Omega^-\pi^+$, σ ~6 MeV/c^2, and $\Omega_c^0 \rightarrow \Omega^-\pi^-\pi^+\pi^+$, σ ~11 MeV/c^2. Also the fitted mass for $\Omega_c^0 \rightarrow \Xi^-K^-\pi^+\pi^+$, 2703 MeV/c^2 is lower than the two other modes' values, 2708 MeV/c^2. Additionally, the error on the mass fit for $\Xi^-K^-\pi^+\pi^+$ mode, 8 MeV/c^2, is worse when compared to $\Omega^-\pi^+$ and $\Omega^-\pi^-\pi^+\pi^+$ modes. These imply that the reconstruction of $\Omega_c^0 \rightarrow \Xi^-K^-\pi^+\pi^+$ decay mode is not as accurate as the others. Therefore the relative decay fractions for this decay mode will not be calculated.

8.6 Reflection and Contamination Studies

Misidentified particles may result in incorrect invariant mass calculations. A kaon, for example, which is wrongly identified as a pion would cause a lower invariant mass

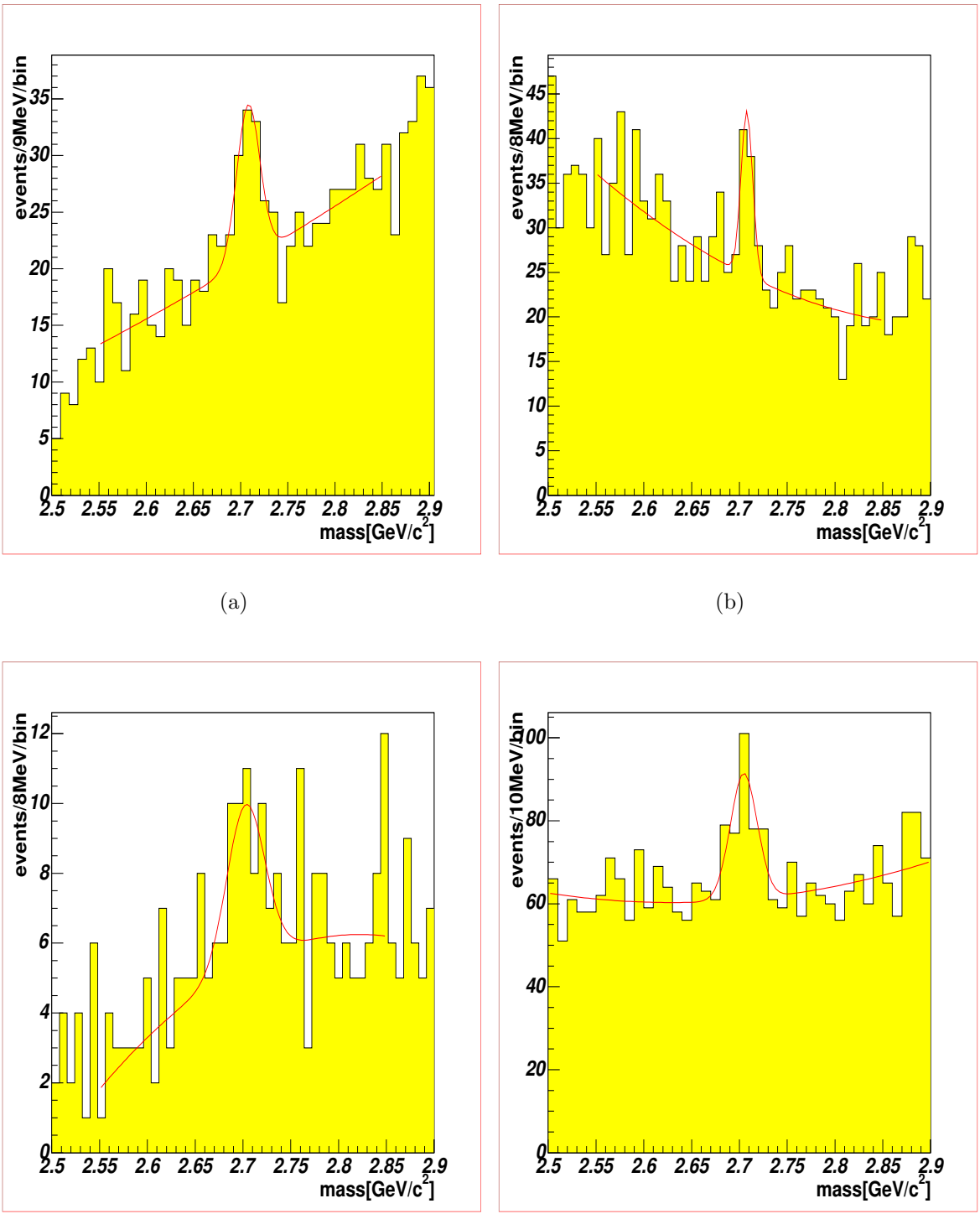

Figure 8.6: Invariant mass plots of three decay modes of Ω_c^0 : (a) $\Omega^-\pi^-\pi^+\pi^+$, (b) $\Omega^-\pi^+$, (c) $\Xi^-K^-\pi^+\pi^+$and (d) sum of (a)+(b)+(c). See text for details.

estimation in a decay. For this reason, several possible reflection and contamination sources in our analysis were investigated.

8.6.1 Possible Contamination and Reflection in $\Omega_c^0 \rightarrow \Omega^-\pi^+$mode

In the $\Omega^-\pi^+$ decay mode of Ω_c^0, four types of interferences may be present. Table 8.6 summarizes these possibilities and their mass shift appearances in the Ω_c^0 invariant mass calculation. Two decay modes in this table have positive mass shift in the $\Omega_c^0 \rightarrow \Omega^-\pi^+$ hypothesis and might contaminate our sample. In a Cabbibo Favored $\Xi_c^0 \rightarrow \Xi^-\pi^+$ decay, if the Ξ^- is wrongly identified and interpreted as an Ω^- in the invariant mass calculation as a $\Omega^-\pi^+$ decay, this might cause a reflection under our real $\Omega_c^0 \rightarrow \Omega^-\pi^+$ signal. In this analysis this is avoided by the RICH particle identification cut on the hyperon's daughter particle. The particle ID probability cut on the hyperon's daughter eliminates the possibility of wrong hyperon assignment to the $\Omega_c^0 \rightarrow \Omega^-\pi^+$ decay.

8.6.1.1 Investigation Of Cabbibo Suppressed (CS) $\Omega_c^0 \rightarrow \Xi^-\pi^+$ Decay

In our $\Omega^-\pi^+$ invariant mass plot, an excess of 85 events over an estimated 52 background events in the last three bins, 2879-2900 MeV/c^2, is seen. If this is due to a Ξ^- misidentified as a Ω^-, it can only be due to (see table 8.6) CS $\Omega_c^0 \rightarrow \Xi^-\pi^+$. It can be checked if this is the case of a particle misidentification, by simply assigning the Ξ^- mass to the Ω^- candidates and recalculating the invariant mass. A peak in the recalculated $\Xi^-\pi^+$ invariant mass spectrum would then imply a possible contamination. The exercise of recalculating the invariant mass with a $\Xi^-\pi^+$ hypothesis is seen after our observation cuts in figure 8.7. There is no peak or particular structure that would suggest a misidentification of Ξ^- as Ω^-. The conclusion is that the excess events in the last three bins is just a statistical fluctuation and not evidence of CS, $\Omega_c^0 \rightarrow \Xi^-\pi^+$

events.

8.6.2 Possible Reflection of $\Omega_c^0 \to \Omega^-\pi^-\pi^+\pi^+$Mode

Similarly, as in section 8.6.1, there might be two possible contaminations: $\Xi_c^0 \to \Xi^- K^+\pi^+\pi^-$ and $\Omega_c^0 \to \Omega^- K^+\pi^+\pi^-$.

The reconstructed mass of the $\Xi_c^0 \to \Omega^- K^+\pi^+\pi^-$ decay is smaller than the invariant Ξ_c^0 mass calculated using the $\Omega^-\pi^-\pi^+\pi^+$ hypothesis. Therefore, no contribution (contamination) to our $\Omega_c^0 \to \Omega^-\pi^-\pi^+\pi^+$ mass peak is expected.

The CS $\Omega_c^0 \to \Omega^-\pi^- K^+\pi^+$ reconstructed mass is lower than the Ω_c^0 mass under the $\Omega^-\pi^-\pi^+\pi^+$ hypothesis (Replacing K, m_K=494 MeV/c^2, with π, m_π=140 MeV/c^2, takes the $\Omega_c^0 \to \Omega^-\pi^-\pi^+\pi^+$ hypothesized invariant mass to a lower value). Therefore no contamination is expected from this mode either.

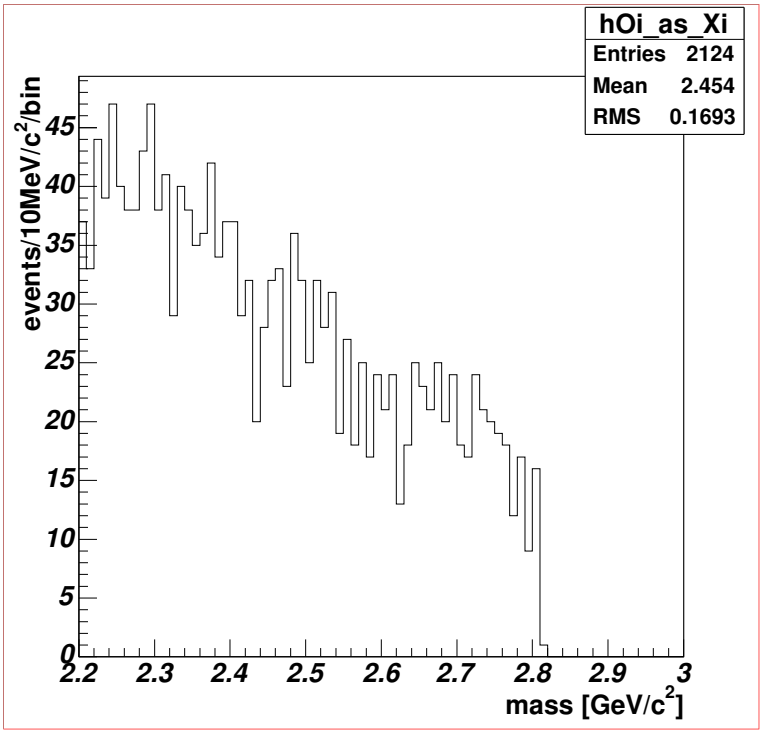

Figure 8.7: $\Omega_c^0 \to \Xi^-\pi^+$ from the $\Omega_c^0 \to \Omega^-\pi^+$ events by replacing Ω^- with Ξ^-

8.6.3 Possible Reflection of $\Omega_c^0 \to \Xi^- K^- \pi^+ \pi^+$Mode

If the π^- in the decay $\Xi_c^0 \to \Xi^- \pi^+ \pi^+ \pi^-$ is misidentified as K^- then this decay may look like a $\Omega_c^0 \to \Xi^- K^- \pi^+ \pi^+$ decay. Therefore a RICH identification for the K^- was required to avoid possible reflection from $\Xi_c^0 \to \Xi^- \pi^+ \pi^+ \pi^-$. 25,000 Monte Carlo $\Xi_c^0 \to \Xi^- \pi^+ \pi^+ \pi^-$ events were generated with QQ and used to reconstruct these events with SOAP as if they were $\Omega_c^0 \to \Xi^- K^- \pi^+ \pi^+$ events. In figure 8.8(a), the reconstructed $\Xi_c^0 \to \Xi^- \pi^+ \pi^+ \pi^-$ events are shown. In 8.8(b), the reconstructed $\Omega_c^0 \to \Xi^- K^- \pi^+ \pi^+$ events from the same Monte Carlo sample are shown without any observation cuts. There is no indication of any signal enhancement in the Ω_c^0 signal region. When the Ω_c^0 observation cuts are applied to these events, in fact none of them survive the cuts. Therefore we conclude that there are no reflection in our $\Omega_c^0 \to \Xi^- K^- \pi^+ \pi^+$ sample due to the misidentification of π^- as K^-.

8.6.4 $\Omega_c^0 \to \Omega^- \pi^+ \pi^0$ and $\Omega_c^0 \to \Omega^- \pi^- \pi^+ \pi^+ \pi^0$ Contamination

One of the earlier reported [59] decay modes of Ω_c^0 is $\Omega_c^0 \to \Omega^- \pi^+ \pi^0$. This decay mode's signature in the SELEX detector would be very similar to that of the $\Omega^- \pi^+$ if the π^0 went undetected. The same argument holds true for $\Omega^- \pi^- \pi^+ \pi^+ \pi^0$. An undetected π^0 would make this event look like a $\Omega^- \pi^- \pi^+ \pi^+$ decay.

This might in fact be another source of contamination for our sample. Therefore we wanted to see how $\Omega_c^0 \to \Omega^- \pi^+ \pi^0$ and $\Omega_c^0 \to \Omega^- \pi^- \pi^+ \pi^+ \pi^0$ events would look like in our sample of $\Omega^- \pi^+$ and $\Omega^- \pi^- \pi^+ \pi^+$ events. The embedded Monte Carlo was used for this study. With QQ we generated 120,000 events for each of the $\Omega_c^0 \to \Omega^- \pi^+ \pi^0$ and $\Omega_c^0 \to \Omega^- \pi^- \pi^+ \pi^+ \pi^0$ decay modes. These events were then reconstructed as if they were $\Omega^- \pi^- \pi^+ \pi^+$and $\Omega^- \pi^+$events by ignoring the π^0s. The reconstructed Ω_c^0 invariant masses for both of these decay modes appear as background without any enhancement in the expected Ω_c^0 nominal mass region as shown in figures 8.9(a) and 8.9(b). When we

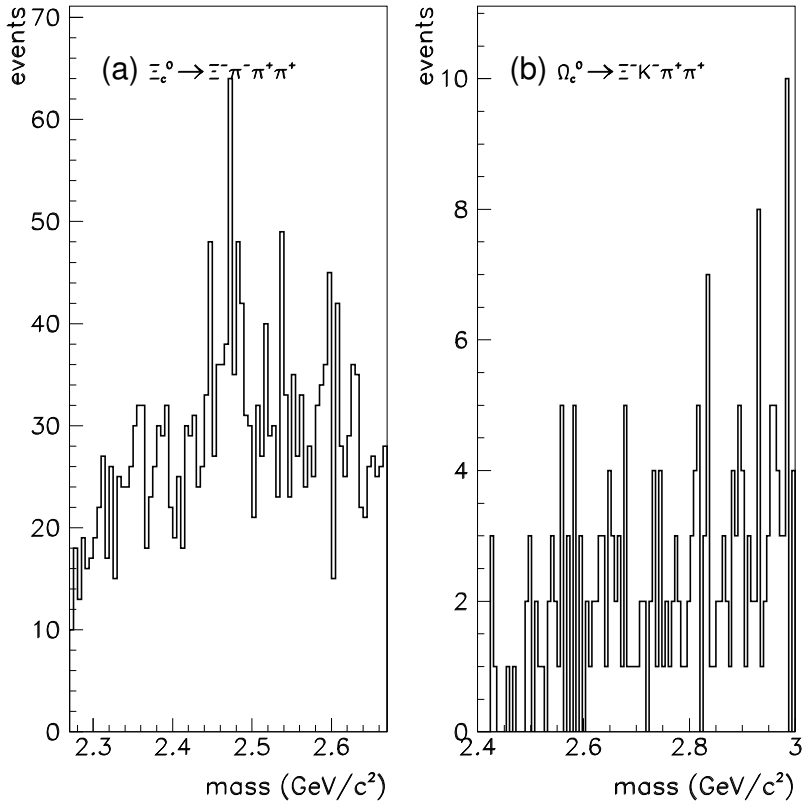

Figure 8.8: Ξ_c^0 Monte Carlo events reconstructed with SOAP: (a) $\Xi_c^0 \to \Xi^-\pi^+\pi^+\pi^-$, (b) SOAP reconstruction of the same $\Xi_c^0 \to \Xi^-\pi^+\pi^+\pi^-$ Monte Carlo sample under $\Omega_c^0 \to \Xi^-K^-\pi^+\pi^+$ hypothesis.

apply our observation cuts for $\Omega^-\pi^+$ and $\Omega^-\pi^-\pi^+\pi^+$ decay channels, only a few of these events survive as seen in figures 8.9(c) and 8.9(d). The conclusion from this study is that $\Omega_c^0 \to \Omega^-\pi^+\pi^0$ and $\Omega_c^0 \to \Omega^-\pi^-\pi^+\pi^+\pi^0$ events with a possible undetected π^0 appear only as a background in our $\Omega_c^0 \to \Omega^-\pi^+$ and $\Omega_c^0 \to \Omega^-\pi^-\pi^+\pi^+$ sample and do not survive the observation cuts as $\Omega^-\pi^+$ and $\Omega^-\pi^-\pi^+\pi^+$ decay modes. No contamination is expected to the signal in $\Omega_c^0 \to \Omega^-\pi^+$ and $\Omega_c^0 \to \Omega^-\pi^-\pi^+\pi^+$ decay modes.

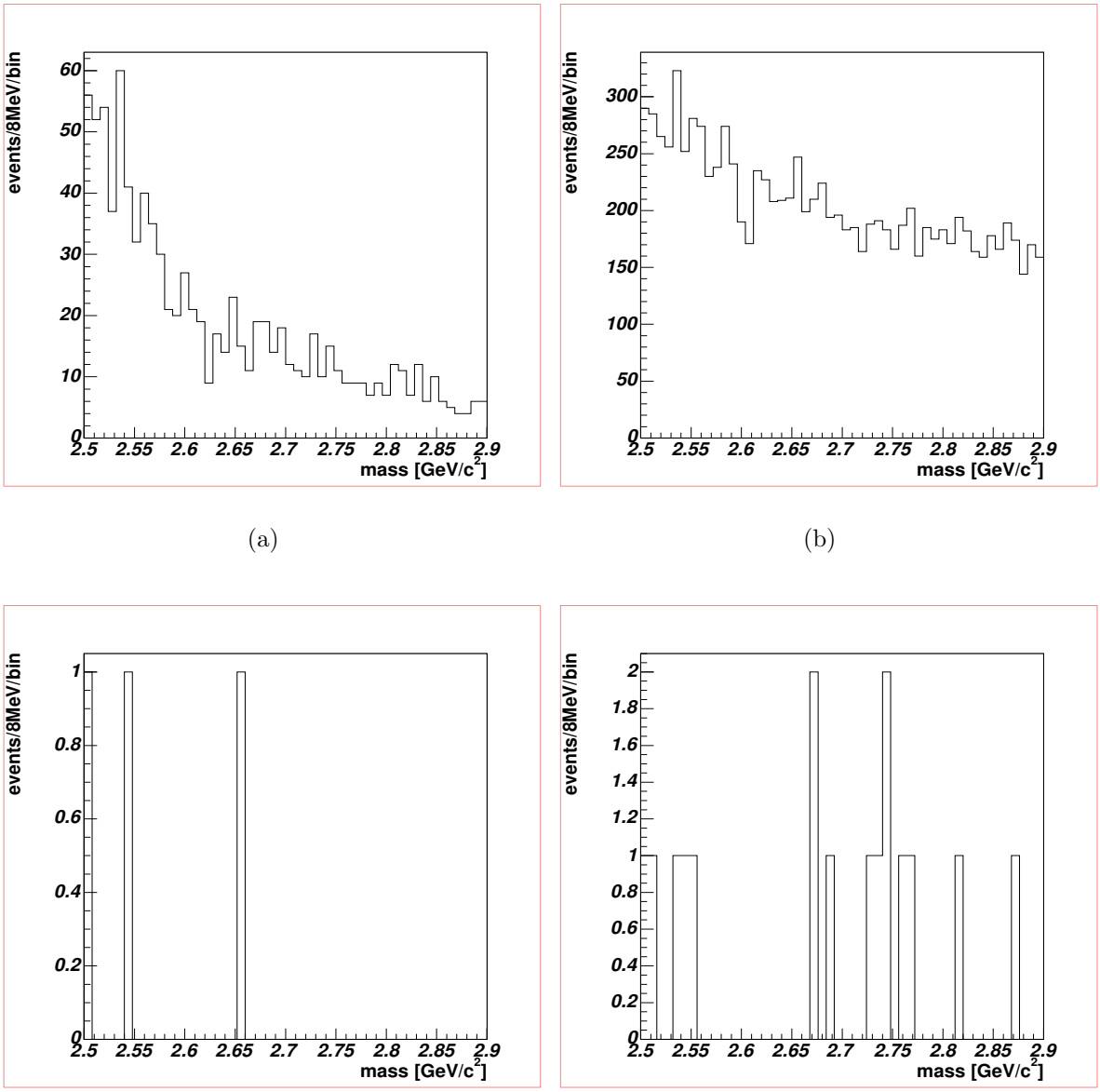

Figure 8.9: The Monte Carlo generated $\Omega_c^0 \to \Omega^-\pi^+\pi^0$ and $\Omega_c^0 \to \Omega^-\pi^-\pi^+\pi^+\pi^0$ events reconstructed as $\Omega_c^0 \to \Omega^-\pi^+$ and $\Omega_c^0 \to \Omega^-\pi^-\pi^+\pi^+$ (a),(b) before and (c),(d) after the observation cuts.

8.7 $\mathcal{B}(\Omega^-\pi^-\pi^+\pi^+)/\mathcal{B}(\Omega^-\pi^+)$ Relative Branching Fraction Measurement

As the production cross section of the Ω_c^0 baryon is unknown, the absolute branching ratios for $\Omega^-\pi^+$ and $\Omega^-\pi^-\pi^+\pi^+$ can not be calculated. However the relative branching fractions for these decay channels with respect to each other can be calculated.

8.7.1 D^0 4-body/2-body Relative Branching Fraction

In order to verify our ability to calculate a relative decay fraction measurement with four-body and two-body decay modes, and to check our method, first a measurement of relative branching fraction was carried out with $D^0 \rightarrow K^-\pi^-\pi^+\pi^+$ and $D^0 \rightarrow K^-\pi^+$ decays. The relative branching ratio for these decays is well established, $\mathcal{B}(D^0 \rightarrow K^-\pi^-\pi^+\pi^+)/\mathcal{B}(D^0 \rightarrow K^-\pi^+) = 1.96 \pm 0.06$ [21]. The same exercise was carried out earlier with the first pass of SELEX data in the measurement of the branching fractions of the $\Xi_c^+ \rightarrow pK^-\pi^+$ charm baryon decay relative to $\Xi_c^+ \rightarrow \Sigma^+K^-\pi^+$ and $\Xi_c^+ \rightarrow \Xi^-\pi^+\pi^+$ [77]. We used the same set of cuts as the above mentioned study and they are listed below:

- the primary vertex should be between -6.5 cm$< Z_p <$0.2 cm
- $l/\sigma > 8$, the significance of the primary-secondary vertex separation must be greater than 8
- the error on l should be less than 0.15 cm, $\sigma < 0.15$
- $Z_s <$2.5 cm
- the beam momentum should be greater than 500 GeV/c, $P_z^{beam} >$500 GeV/c
- the second largest miss distance of secondary tracks extrapolated back to primary vertex over its error, *scut* should be greater than 7.5, $scut > 7.5$
- $pvtx < 5$
- $p_\pi >$10 GeV/c, ($D^0 \rightarrow K^-\pi^+$ mode)
- $p_\pi >$5 GeV/c, ($D^0 \rightarrow K^-\pi^-\pi^+\pi^+$ mode)

The D^0 signal events after these cuts are shown figures 8.10(a) and 8.10(b). In order to calculate the acceptance, 99,000 Monte Carlo events were generated with QQ

for each $D^0 \to K^-\pi^-\pi^+\pi^+$ and $D^0 \to K^-\pi^+$ modes. In table 8.7, the acceptances for $D^0 \to K^-\pi^-\pi^+\pi^+$ and $D^0 \to K^-\pi^+$ decay modes and the measured relative branching ratio are shown. The relative decay fraction for $\mathcal{B}(D^0 \to K^-\pi^-\pi^+\pi^+)/\mathcal{B}(D^0 \to K^-\pi^+)$ is calculated as 2.06 ± 0.10. This value is in good agreement with the value reported in PDG, 1.96 ± 0.09. within the errors.

8.7.2 $\mathcal{B}(\Omega_c^0 \to \Omega^-\pi^-\pi^+\pi^+)/\mathcal{B}(\Omega_c^0 \to \Omega^-\pi^+)$ Calculation

The evaluation of the branching ratio requires the Ω_c^0 acceptance of the SELEX spectrometer. This value was computed using the Monte Carlo. Figures 8.6(a) and 8.6(b) show the Ω_c^0 mass reconstructed for two decay modes used to evaluate the branching ratio. The number of signal events was taken from the fits. The acceptance is calculated as the ratio of the Monte Carlo events after observation cuts divided by the total number of generated events. As seen in table 8.8, the acceptances are smaller than what was quoted in table 8.4 in that they now also include the cut efficiencies. The number of signal events for each decay mode corrected for the acceptance, give the relative branching ratio

$$\frac{\mathcal{B}(\Omega_c^0 \to \Omega^-\pi^-\pi^+\pi^+)}{\mathcal{B}(\Omega_c^0 \to \Omega^-\pi^+)} = 2.00 \pm 0.45$$

The quoted error is statistical only. The systematic error analysis will be presented in section 8.8.

8.8 Relative Branching Fraction Systematics Study

The estimation of the systematic errors is often done by employing the combination of two methods [76]. The first method is to split the data sample into several sub-samples and repeat the analysis with these smaller samples. This provides a measure of how much of the error in the measurement is due to the statistical fluctuations

Table 8.6: Possible mass reflections in $\Omega^-\pi^+$ hypothesis

decay mode	Cabbibo	mass shift in $\Omega_c^0 \to \Omega^-\pi^+$hypothesis
$\Xi_c^0 \to \Xi^-\pi^+$	favored (CF)	+
$\Xi_c^0 \to \Omega^- K^+$	favored (CF)	-
$\Omega_c^0 \to \Xi^-\pi^+$	suppressed (CS)	+
$\Omega_c^0 \to \Omega^- K^+$	suppressed (CS)	-

Table 8.7: $\mathcal{B}(D^0 \to K^-\pi^-\pi^+\pi^+)/\mathcal{B}(D^0 \to K^-\pi^+)$ Relative Branching Fraction

$D^0 \to K^-\pi^+$ acceptance	$D^0 \to K^-\pi^-\pi^+\pi^+$ acceptance	$\mathcal{B}(K^-\pi^-\pi^+\pi^+)/\mathcal{B}(K^-\pi^+)$ Relative BR
$12.1\% \pm 0.11\%$	$6.15\% \pm 0.08\%$	2.06±0.10

Table 8.8: Summary of the number of events and the acceptances for Ω_c^0 modes used for the relative decay fraction calculation

	Events	Acceptance (%)
$\Omega_c^0 \to \Omega^-\pi^-\pi^+\pi^+$	44 ± 15	0.0120 ± 0.0013
$\Omega_c^0 \to \Omega^-\pi^+$	35 ± 12	0.0191 ± 0.0015

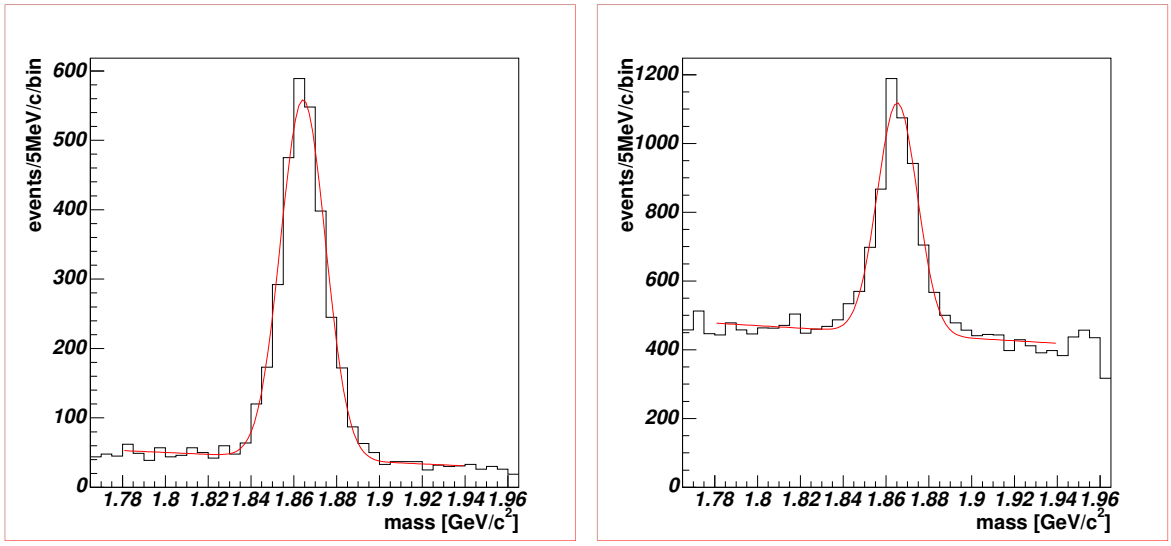

(a) (b)

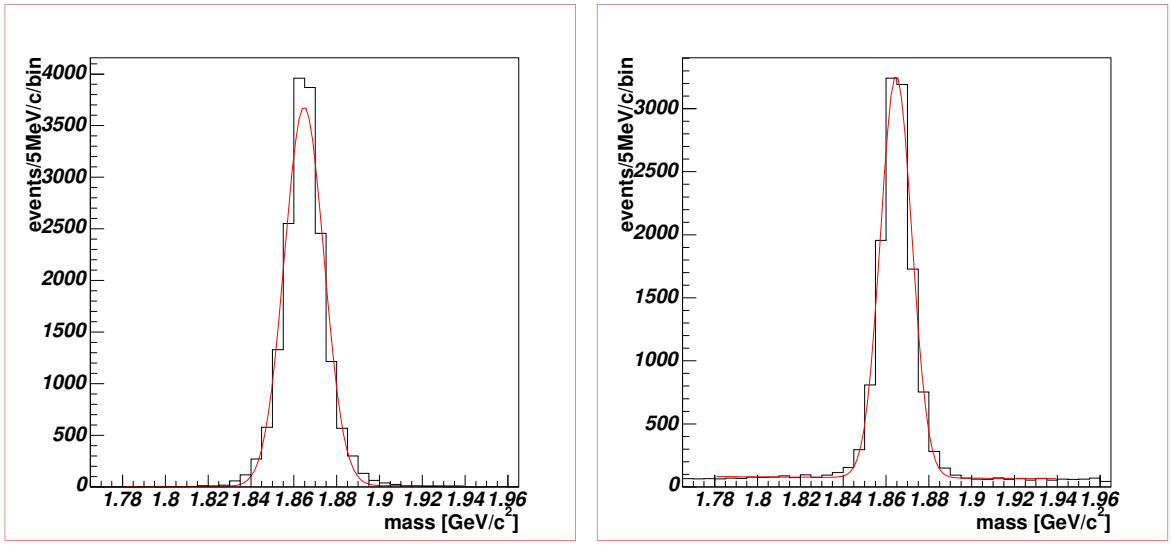

(c) (d)

Figure 8.10: D^0 data and the Monte Carlo events after observation cuts: (a) data $D^0 \to K^-\pi^+$, (b) data $D^0 \to K^-\pi^-\pi^+\pi^+$, (c) Monte Carlo $D^0 \to K^-\pi^+$, (d) Monte Carlo $D^0 \to K^-\pi^-\pi^+\pi^+$.

and how much of it could actually be assigned as systematic error. This method by its nature requires a data (signal) sample large enough that it can be divided into two or more sub-samples. However with only 107 total signal events for Ω_c^0 in three decay modes, this method is not applicable in our analysis. The second method is the estimation of systematic errors due to the fitting techniques used. The variations in the fitting technique, background parameterizations, and the fit functions may all have an effect on the final results. The information on the systematic error is then calculated as the RMS spread in a set of estimations. This method ensures that the systematic error is independent of the number of the considered systematic error sources. Mathematically speaking, the systematic error, σ_{sys}, due to the N different fitting techniques is

$$\sigma_{sys} = \sqrt{\frac{\sum_i^N x_i^2 - N(\overline{x})^2}{N-1}} \tag{8.1}$$

where

$$\overline{x} = \sum_i^N x_i/N \tag{8.2}$$

It is assumed here that the systematic due to all fit variations are equally likely, hence the straight average rather than the weighted average is taken. In the estimation of the systematic errors in our relative branching fraction calculation, the fit function and the range that the function fitted were varied. As a seperate method to calculate the number of signal events, the signal events were calculated by counting the total number of events in a signal window and subtracting the estimated number of background events from the total number of events counted. These studies will be explained in detail in the subsequent sections.

8.8.1 Fit Function and Fit Range Variation

In the calculation of the number of signal events, the signal events were characterized with a Gaussian function. The background is parametrized as a polynomial of

order n. The invariant mass distributions are fitted to a function which is the sum of the Gaussian and the background functions.

8.8.1.1 Fit function: Gaussian + pol^2 (2^{nd} order polynomial)

Using a Gaussian plus a second order polynomial fit function, the range over the function was fitted was varied. The number of events calculated are tabulated in tables 8.9 and 8.10.

8.8.1.2 Fit function: Gaussian + pol^1 (1^{st} order polynomial)

The background parametrization is changed from a 2^{nd} order polynomial function to 1^{st} order polynomial function. As in the previous section, the two different fit ranges were studied. The fit results are tabulated in tables 8.11 and 8.12.

The $\mathcal{B}(\Omega_c^0 \to \Omega^-\pi^-\pi^+\pi^+)/\mathcal{B}(\Omega_c^0 \to \Omega^-\pi^+)$ relative branching ratios corresponding to the number of signal events and acceptance values reported in tables 8.9, 8.10, 8.11 and 8.12 are presented in table 8.13

Table 8.9: Gaussian + pol^2; fit range: 2550-2850 MeV/c^2

	Events	Acceptance (%)
$\Omega_c^0 \to \Omega^-\pi^-\pi^+\pi^+$	44 ± 14	0.0120 ± 0.0013
$\Omega_c^0 \to \Omega^-\pi^+$	35 ± 12	0.0191 ± 0.0015

Table 8.10: Gaussian + pol^2; fit range: 2500-2900 MeV/c^2

	Events	Acceptance (%)
$\Omega_c^0 \to \Omega^-\pi^-\pi^+\pi^+$	40 ± 14	0.0122 ± 0.0013
$\Omega_c^0 \to \Omega^-\pi^+$	37 ± 13	0.0193 ± 0.0015

Table 8.11: Gaussian + pol^1; fit range: 2550-2885 MeV/c^2

	Events	Acceptance (%)
$\Omega_c^0 \to \Omega^-\pi^-\pi^+\pi^+$	45 ± 15	0.0124 ± 0.0013
$\Omega_c^0 \to \Omega^-\pi^+$	31 ± 12	0.0195 ± 0.0015

Table 8.12: Gaussian + pol^1; fit range: 2500-2900 MeV/c^2

	Events	Acceptance (%)
$\Omega_c^0 \to \Omega^-\pi^-\pi^+\pi^+$	46 ± 15	0.0128 ± 0.0013
$\Omega_c^0 \to \Omega^-\pi^+$	28 ± 12	0.0195 ± 0.0015

8.8.2 Counting The Number of Signal Events

As a different method to measure the number of signal events, the number of events $(S+B)$ in the mass window (2685-2725) MeV, 40 MeV band, were counted. The number of background events in this band (B), was estimated by a fit to the background. By subtracting B from $S+B$, the number of signal events, S was calculated. The results are tabulated in table 8.14. The relative branching ratios calculated with this method

Table 8.13: $\mathcal{B}(\Omega_c^0 \to \Omega^-\pi^-\pi^+\pi^+)/\mathcal{B}(\Omega_c^0 \to \Omega^-\pi^+)$ relative branching fraction calculated by a fit with a Gaussian + a polynomial of order n, pol^n, with varying fit ranges. The errors are statistical only.

Fit Function	Fit Range (MeV/c^2)	$\mathcal{B}(\Omega_c^0 \to \Omega^-\pi^-\pi^+\pi^+)/\mathcal{B}(\Omega_c^0 \to \Omega^-\pi^+)$
Gauss+pol^2	2550-2850	2.00±0.45
Gauss+pol^2	2500-2900	1.71±0.39
Gauss+pol^1	2550-2850	2.28±0.53
Gauss+pol^1	2500-2900	2.50±0.59

are tabulated in table 8.15.

Table 8.14: The number of signal events by counting in (2685-2725) MeV/c^2 window

Decay	$(S+B)_{count}$	B_{fit}		S	
		G+p1	G+p2	G+p1	G+p2
$\Omega^-\pi^+$	159	130	124	29	35
$\Omega^-\pi^-\pi^+\pi^+$	127	83	83	44	44

8.8.3 $\mathcal{B}(\Omega_c^0 \to \Omega^-\pi^-\pi^+\pi^+)/\mathcal{B}(\Omega_c^0 \to \Omega^-\pi^+)$ Total Systematic Error

In order to calculate the total systematic error of the relative branching fraction measurement, the results of the fit variant studies presented in sections 8.8.1, and 8.8.2 were combined by using the method described in section 8.8. The systematic errors calculated with different fitting techniques are tabulated in table 8.16. In the fit

Table 8.15: $\mathcal{B}(\Omega_c^0 \to \Omega^-\pi^-\pi^+\pi^+)/\mathcal{B}(\Omega_c^0 \to \Omega^-\pi^+)$ relative branching fraction calculated by counting the number of signal events in the signal window (2685-2725 MeV/c^2) and estimating the background events in the same range from by a fit to the background with function, B_{fit}.

B_{fit} function	B_{fit} range (MeV/c^2)	$\mathcal{B}(\Omega_c^0 \to \Omega^-\pi^-\pi^+\pi^+)/\mathcal{B}(\Omega_c^0 \to \Omega^-\pi^+)$
Gauss+pol2	2550-2850	2.00±0.45
Gauss+pol1	2550-2850	2.41±0.58

technique "1", for example, a Gaussian is used to describe the signal region. The background parametrization is done with a second order polynomial in the range [2550-2850] MeV/c^2. Fit technique 5 finds the number of signal events by subtracting the number of background events, which was calculated from a second order polynomial fit to the background in the range [2550-2850] MeV/c^2, from the total number of events obtained by counting the events in the [2685-2725] MeV/c^2 signal window.

A total systematic error of our measurement of relative branching fraction was calculated as ±0.30.

In figure 8.11, the relative branching fraction measurements tabulated in table 8.16 are plotted. The "fit method" number corresponds to the "Fit[#]" in the table. The horizontal lines are drawn at the statistical error limits.

8.9 Summary and Discussion of Results

In summary, the observation of 107 ± 22 Ω_c^0 events with a mass $2708 \pm 2.0 \pm 2.6$ MeV/c^2 in three decay modes is reported. In the $\Omega_c^0 \to \Omega^-\pi^-\pi^+\pi^+$ decay mode, 44 ± 14 events with mass 2708.0 ± 4.5 MeV/c^2, in the $\Omega_c^0 \to \Omega^-\pi^+$ decay mode 35 ± 12 events with mass 2708.0 ± 2.0 MeV/c^2, and finally in the $\Omega_c^0 \to \Xi^- K^-\pi^+\pi^+$ decay mode 28 ± 12 events with mass 2703.0 ± 8.0 MeV/c^2 is found.

Table 8.16: $\mathcal{B}(\Omega_c^0 \to \Omega^-\pi^-\pi^+\pi^+)/\mathcal{B}(\Omega_c^0 \to \Omega^-\pi^+)$ relative branching fraction measurements for different fit techniques are listed.

Fit [#]	function signal + background	[Range] MeV/c^2	Relative Branching Fraction
1	Gaussian + $a + bx + cx^2$	[2550-2850]	2.00 ± 0.45
2	Gaussian + $a + bx + cx^2$	[2500-2900]	1.71 ± 0.39
3	Gaussian + $a + bx$	[2550-2850]	2.28 ± 0.53
4	Gaussian + $a + bx$	[2500-2900]	2.50 ± 0.59
5	Counting + $a + bx + cx^2$	[2550-2850]	2.00 ± 0.45
6	Counting + $a + bx$	[2550-2850]	2.41 ± 0.58

We measured $\mathcal{B}(\Omega_c^0 \to \Omega^-\pi^-\pi^+\pi^+)/\mathcal{B}(\Omega_c^0 \to \Omega^-\pi^+)$=$2.00 \pm 0.45(stat) \pm 0.32(sys)$. This result is the first relative branching ratio measurement for these decay modes.

The measurement of the Ω_c^0 mass agrees with the theoretical predictions of Martin et al.[48] (2708 MeV/c^2) and of Roncaglia et al.[49] (2710 MeV/c^2).

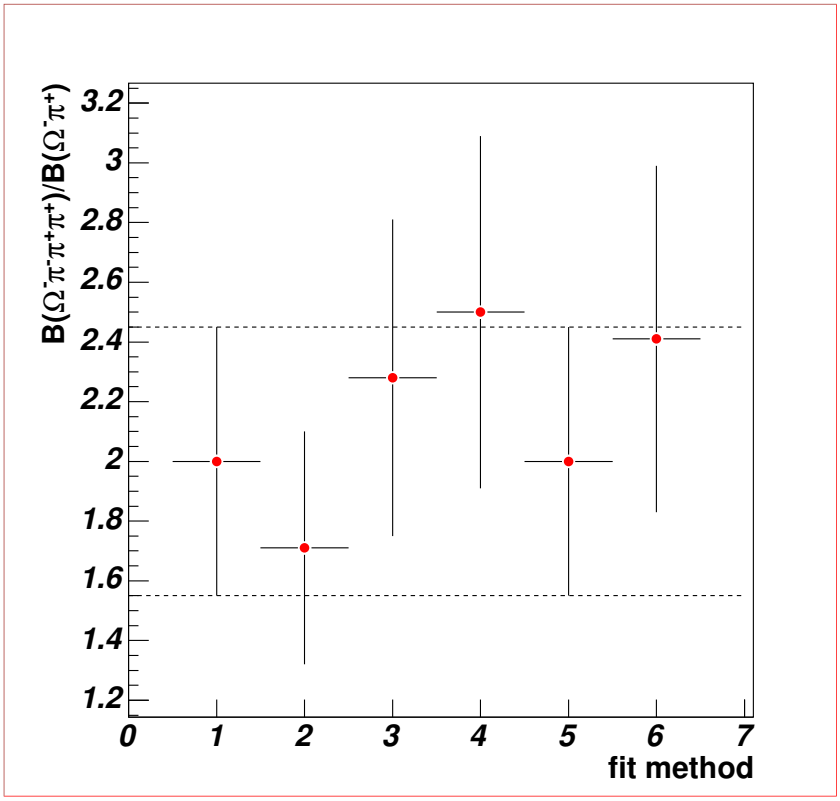

Figure 8.11: The relative branching fraction measurements corresponding to different signal event calculation methods

CHAPTER 9
SUMMARY AND CONCLUSION

In the first part of this thesis, the results of the design studies of the CMS forward calorimeter are presented. The forward calorimeter of the CMS experiment will operate in an extremely harsh radiation environment. Therefore it was necessary to come up with a design for a forward calorimeter that would withstand the high radiation levels over the ∼10 years of the LHC operation. The effects of the radiation on the forward calorimeter will be seen mostly as the degradation of quartz fiber performance. Therefore the characterization of the fibers under radiation is needed in order to predict the behavior for the detectors using these fibers. Three different types of quartz-core fibers were tested and their attenuation under radiation and recovery when the exposure of radiation is removed were characterized.

All of the tested fibers showed a recovery when the neutron fluence was removed or reduced. We determined the typical recovery time constant to be of the order of $10^3 - 10^4$ seconds. This is an important parameter for the calibration of the forward calorimeter. However it should again be noted that the attenuation is restored when the fibers are again exposed to the radiation. The neutron rates at which the tests were done were higher than what is expected at the location of forward calorimeter. This confirmed that this detector is operable in such a high radiation environment. We characterized the kinetic behavior of attenuation of the fibers with a function of the form of a power-law, aD^b. The FSHA and FIA type fibers showed a somewhat similar behavior for the parameter, b. The attenuation of the IN type fiber was found to be larger.

In order to understand the dose and the activation levels of the forward calorimeter's absorber and its effect on the quartz fibers, a second type of radiation study was carried out at the electron beam pre-injector facility (LIL) at CERN. We determined the lateral and longitudinal dose and radioactivity profiles in the calorimeter absorber. With

500 MeV electrons, a total dose of ∼660 kGrays at the shower maximum were measured. By underestimating effects of the short-lived isotopes we determined a simple conversion factor between the dose and the induced radioactivity as ∼6 Bq/Gy. The integrated dose at the location of the forward calorimeter of CMS will reach ∼1 GRad. Using this value and without being concerned much about the operation cycles of the LHC, and hence ignoring activation-deactivation effects, we calculate approximately ∼60 MBq of radioactivity for the forward calorimeter.

The first pre-production-prototype (PPP-I) of the forward calorimeter was constructed and tested at CERN. Several different properties of this detector was studied. The response non-uniformity of the PPP-I due to the fiber periodicity was found to be within ±6%. A sharp tower to tower signal transition which suggests narrow shower profiles was also observed. This is an important feature for a calorimeter in that it eliminates the energy leakage out of the calorimeter hence not yielding any wrong energy measurement. The energy resolution of PPP-I was tested with both electron and hadronic (π) beams. The electromagnetic energy resolution was measured to be $(\sigma/E)^2 = (197\%/\sqrt{E})^2 + (8.0\%)^2$. The hadronic energy resolution was determined to be 20% at 1 TeV. These measurements confirmed that the PPP-I functioned at its designed parameters.

In the second part of the thesis, the results of the Ω_c^0 analysis from the SELEX (E781) data is presented. A total of 107 ± 22 Ω_c^0 events with a mass $2708 \pm 2.0 \pm 2.6$ MeV/c^2 were observed in three decay modes; 44 ± 14 events with mass 2708.0 ± 4.5 MeV/c^2 in $\Omega_c^0 \to \Omega^-\pi^-\pi^+\pi^+$ decay mode, 35 ± 12 events with mass 2708.0 ± 2.0 MeV/c^2 in $\Omega_c^0 \to \Omega^-\pi^+$ decay mode, and finally 28 ± 12 events with mass 2703.0 ± 8.0 MeV/c^2 in $\Omega_c^0 \to \Xi^- K^-\pi^+\pi^+$ decay mode.

There is a very limited number of theoretical studies on Ω_c^0 and there is yet to be a consensus among the models predicting the Ω_c^0 mass. Our measurement of the Ω_c^0 mass agrees with the theoretical predictions of Martin et al.[48] (2708 MeV/c^2) and

of Roncaglia et al.[49] (2710 MeV/c^2). Furthermore it is 3.7σ higher than the latest experimentally measured mass, 2697.5 MeV/c^2, by the FOCUS collaboration.

For the branching ratios of Ω_c^0, the theoretical study situation is not very different from the mass. Theoretical predictions for the branching ratios are mostly limited to two body decay modes [78] [79]. This is not hard to understand as the hadronic decay mechanisms of heavy quark systems are prohibitively complicated to calculate due to the initial and final state interactions. $\mathcal{B}(\Omega_c^0 \to \Omega^-\pi^-\pi^+\pi^+)/\mathcal{B}(\Omega_c^0 \to \Omega^-\pi^+)$ was measured as $2.00 \pm 0.45(stat) \pm 0.32(sys)$. This result is the first relative branching ratio measurement for these decay modes. This is to say that the four-body decay mode seems to be favored over the two-body decay. When this result is compared with another singly charmed neutral baryon, Ξ_c^0, a similar trend is observed ($\mathcal{B}(\Xi_c^0 \to \Xi^-\pi^-\pi^+\pi^+)/\mathcal{B}(\Xi_c^0 \to \Xi^-\pi^-) = 3.33 \pm 1.33 \pm 0.55$ [44]).

It is hoped that our relative branching ratio measurement will provide additional information and better understanding of the singly charmed baryon, in particular Ω_c^0, decay mechanisms.

REFERENCES

[1] *The Hadron Calorimeter Project, Technical Design Report*, CERN/LHCC 97-31, 1997

[2] P.A. Cerenkov, Nobel Lectures in Particle Physics, New York, Elsevier, 1964

[3] N. Akchurin et al., Nucl. Inst. and Meth. **A 399**, (1997), 202

[4] K. Gill et al., Gamma and Neutron Radiation Damage Studies of Optical Fibers, CERN-ECP/96-13, 1996

[5] K. Nagasawa, Y. Hoshi, Y. Ohki and K. Yahagi, Jpn. J. Appl. Phys. **25**, (1986), 464 and K. Nagasawa, R. Tohmon, and Y. Ohki, Jpn. J. Appl. Phys. **26**, (1987), 148

[6] D. L. Griscom and E. J. Friebele, Phys. Rev. B. **34**, (1986), 7524

[7] H. Hanafusa, Y. Hibino and F. Yamamoto, J. Appl. Phys., **58**, (1985), 1356

[8] D. L. Griscom, *The Centennial Memorial Issue of The Ceramic Society of Japan*, 1991.

[9] D. Griscom, J. Appl. Phys., **80**, No. 4, (1996), 2142

[10] E. Lell, N. J. Kreidl and J. R. Hensler, in *Progress in Ceramic Science*, edited by J. Burke, (Pergamon Press, Oxford, New York), 1966

[11] H. Hayami et al., *Improvement in Radiation Resistivity of Pure Silica Core Image Guides for Industrial Fiberscopes*, Mitsubishi Cable Industries, Ltd. preprint

[12] A. Utsumi et al., SPIE Vol. 506, Fiber Optics in Adverse Environments II 176-181, 1984

[13] E. J. Friebele and M. E. Gingerich, App. Optics, **20**, (1981), 3448

[14] A. N. Gurzhiev et al., *Radiation Hardness of Optical Fibers*, IHEP 95-121, Protvino 1995.

[15] J. K. Partin, SPIE Vol.506, Fiber Optics in Adverse Environments II, (1984)

[16] N.V.Mokhov, "The MARS Code System User's Guide", Fermilab-FN-628, 1995

[17] A. Uzunian, private communication (CMS/HF tdr130 setup).

[18] RISO stands for radiochromatic film dosimeter developed primarily by RISO National Laboratory, Roskilde, Denmark. See CERN report TIS-CFM/89-14/PP for details.

[19] J. P. Potier and L. Rinolfi, CERN/PS 98-016 (LP), 1998

[20] R. Bock et al., Nucl. Meth. Instr. **186**, (1981), 533

[21] C. Caso et al., Particle Data Group: Review of Particle Physics, European Physical Journal C, **3**, (1998)

[22] The *EGS4* Code System, W. R. Nelson, H. Hirayama and D. W. O. Rogers, SLAC-Report-265

[23] G. Barthow et al., Nucl. Phys. **B20**, (1970), 592

[24] W. R. Nelson et al., Phys. Rev. **149**, (1966), 201

[25] C. J. Crannel, Phys. Rev., **161**, (1967), 310

[26] T. Yuda et al., Nuovo Cimento **65**, (1970), 229 and Nucl. Inst. Meth., **73**, (1969), 301

[27] R. A. Alvarez et al., Phys. Rev. **C20**, (1979), 128

[28] L. Katz et al., Phys. Rev. **82**, (1951), 271

[29] J. W. Norbury et al, Aust. J. Phys. **31**, (1978),471

[30] M. Goldhaber and E. Teller, Phys. Rev **74**, (1948),1046

[31] J. S. Levinger and H. Bethe, Phys. Rev **78**, (1950), 115

[32] R. Montalbetti et al., Phys. Rev. **91**, (1953), 659

[33] L. Jones and K. Terwilliger, Phys. Rev. **91**, (1953), 699

[34] J. S. Levinger, *Nuclear Photo-disintegration*, Oxford University Press, 1960

[35] G. Barthow et al., Nucl. Phys., **B2**, (1967), 669

[36] The neutron spectrum for fission of U^{235} can be represented by a semiempirical equation, $n(E) \sim \exp(-E/0.965)\sinh(\sqrt{2.29E})$. See *Proceedings of the International Conference on the Peaceful Uses of Atomic Energy*, Vol.2 (New York: United Nations, 1956), 193

[37] A. Fenyvesi et al., *Package irradiation studies*, CERN/DRDC/RD-16/FERMI Note-14, CERN, Geneva, Switzerland, (January 1993) and M. A. Lone et al., Nucl.Instr.Methd. **143**, (1977), 331

[38] V. Gavrilov et al., CMS/TN 94-324, 1994

[39] R. Wigmans, Calorimetry: Energy Measurement In Particle Physics, Oxford University Press, 2000

[40] N. Akchurin et al., Nucl. Instr. and Meth. **A399**, (1997), 202

[41] T.S. Virdee, Techniques and Concepts of High Energy Physics X, T. Ferbel ed., NATO Science Series C, **Volume 534**, 1999

[42] J. Russ and the SELEX/E781 Collaboration, SELEX Proposal, FNAL

[43] S.F. Biagi et al., Z. Phys C **28**, (1985), 175

[44] K. Hagiwara et al., Phys.Rev D**66**, (2002), 010001

[45] S. Samuel et al., Phys. Lett. **B175**, (1986), 197

[46] D. Izatt et al., Nucl. Phys. **B199**, (1982), 269

[47] M. Gell-Mann, Phys.Lett. **8**, (1964), 214

[48] Andre Martin and J.M. Richard, CERN-TH/95-86, 1995

[49] R. Roncaglia et al., hep-ph/9602251, 1996

[50] M. Rho et al., Phys. Lett. **B251**, (1990), 597

[51] J.M. Richard et al., Phys. Lett. **B128**, (1983), 453

[52] K. Maltman and N. Isgur, Phys. Rev. **D22**, (1980), 1701

[53] L. Chan, Phys. Rev. **D31**, (1985), 204

[54] A.De Rujula, H. Georgi and S.L. Glashow, Phys. Rev. **D12**, (1975), 147

[55] M. Kobayashi et al., Prog. Theor. Phys. **49**, (1972), 282

[56] H. Albrecht et al., Phys.Lett.,**B288**, (1992), 367

[57] P.L. Frabetti et al., Phys.Lett., **B300**, (1993), 190

[58] J.A. Appel, Proceedings of the International Conference on Lepton and Photon Interactions, Ithaca, 1993

[59] D. Cronin-Hennessy et al., Phys.Rev.Lett. **86**, (2001), 3730

[60] M.I. Adamovich Phys.Lett **B358**, (1995), 151

[61] J.M. Link Phys.Lett **B561**, (2203), 41

[62] A.S. Ayan et al., E781 (SELEX) internal note, H-Note 843

[63] S.L.Glashow et al., Phys.Rev.**D2**, (1970), 1285

[64] J.J. Aubert et al., Phys. Rev. Lett. **33**, (1974), 1404

[65] J.E. Augustin et al.,Phys.Rev.Lett. **33**, (1974), 1406

[66] S.W. Herb et al., Phys. Rev. Lett. **39**, (1977), 252

[67] W.R. Innes, Phys. Rev. Lett. **39**, (1977), 1240, Erratum-ibid.**39**,(1977), 1640

[68] W-Y.P.Hwang and D.B.Lichtenberg, Phys.Rev.**D35**, (1986), 3526

[69] J. Engelfried et al., hep-ex/9811001, 1998

[70] J. Engelfried et al., Nucl.Inst.Meth. **A502**, (2003), 285

[71] ROOT- An Object Oriented Data Analysis Framework, R. Brun, F.Rademakers, Nucl. Inst. & Meth. in Phys. Res. **A389**, (1997), 81

[72] V.Matveev et al., E781 (SELEX) internal note, H-Note 829

[73] J. You, E781 (SELEX) internal note, H-Note 815

[74] QQ-The CLEO Event Generator, http://www.lns.cornell.edu/public/CLEO/soft/QQ (unpublished).

[75] P. Cooper, E781 (SELEX) internal note, H-Note 840

[76] J.Wiss and R. Gadner,"Estimating Systematic Errors", E687 internal note

[77] S. Y. Jun et al., Phys. Rev. Lett. **84**, (2000), 1857

[78] J. G. Korner et al., Z. Phys. C **55**, (1992), 659

[79] J. G. Korner et al., Prog. Part. Nucl. Phys. **33**, (1994), 787